Faculty of Engineering Technology

Additive manufactured enhancement for Two-phase CPU cooling

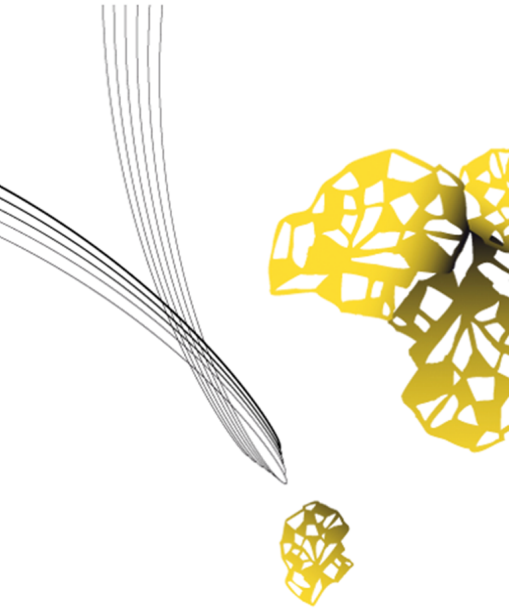

UNIVERSITY OF TWENTE.

NOVOSERVE®

J. Stoop
s2413809

MSc. Thesis
November 16, 2023

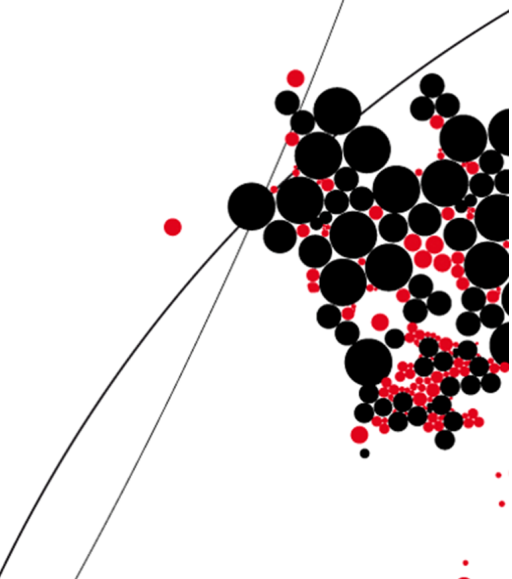

Supervisors
Prof. dr. Tom Vaneker
dr. ir. Davoud Jafari
dr. ir. Mohammad Mehrali

Faculty of Engineering Technology
University of Twente
P.O. Box 217
7500 AE Enschede
The Netherlands

Abstract

Recent studies project that the rapid growth of digital society, the increasing power density of electronic components, the increasing power density of electronic components and the limitations of traditional IT cooling systems lead to major sustainability challenges in data centers. As a result, this study is focused on the development of new advanced two-phase cooling solutions for data center applications and evaluates to what extent a 3D-printed surface microstructure dictates the performance of two-phase loop heat pipes with opposite replenishment and two-phase immersion cooling solutions. In order to investigate the additive manufactured enhancement of loop heat pipes, a new improved steady-state numerical model is developed that predicts the operation behavior in good agreement with experimental data from the literature. The improved model combines the advantages of an existing model that accurately describes heat and mass transfer in the transport lines and condenser section based on a 6th order Runge-Kutta-Method, together with a model that gives a detailed approach to the heat transfer inside the evaporator based on 2D Fourier Series expansion. The numerical simulation suggests that the development of a multi-material 3D-printed evaporator, including a high conductive copper wick/groove structure and a low conductive stainless steel casing material results in an impressive performance enhancement compared to conventional structures. Furthermore, it is predicted that an existing additive-manufactured stainless steel octahedral wick has sufficient capillary performance to satisfy the operation limits of an actual experimental setup. In addition to the numerical model, a 3D-printed stainless steel evaporator is designed and fabricated including an octahedral wick that has the ability to transfer 8.6 W/cm^2 heat. A microscopic analysis observed that the mean pore size of the wick is only 3.5 $\%$ less than the designed CAD model and that the rectangular-designed CAD model grooves are actual parabolic-shaped grooves with high surface roughness. On top of that, an extensive approach is given with limitations and recommendations to test this prototype in practical and experimental applications. Finally, the 3D-printed evaporator including lattice structure and grooves and a prototype that only includes microchannels is tested on heat transfer behavior for two-phase immersion cooling applications by doing a pool boiling test for low heat flux (< 8 W/cm^2). The experimental results observe that the initial heat transfer coefficient of both structures is higher than the tested performance of plain copper and the lattice structure in the literature. It is also observed that this initial high heat transfer coefficient is followed by a reducing heat transfer coefficient which can be related to the vapor blankets that occur due to the geometry or surface morphology of the structure.

Nomenclature

$\bar{M}$	Molar mass [$\frac{kg}{mol}$]
$\bar{R}$	Universal gas constant [$\frac{J}{kg\ mol}$]
$\dot{m}$	Mass flow rate [$\frac{kg}{s}$]
A	Surface area [m^2]
A_f	Contact area between fins and wick [m^2]
B	Coefficients
Bo	Bond number [-]
C_p	Specific heat at constant pressure [$\frac{J}{kgK}$]
G	Mass flux [$\frac{kg}{m^2 s}$]
g	Gravitational acceleration [$\frac{kg}{s^2}$]
H	Height [m]
h	Heat transfer coefficient [$\frac{W}{m^2 K}$]
h	Latent heat [$\frac{J}{kgK}$]
K	Permeability [m^2]
k	Thermal conductivity [$\frac{W}{mK}$]
k_{we}	Effective thermal conductivity of the wick [$\frac{W}{mK}$]
L	Length [m]
M	Mass of working fluid [kg]
Nu	Nusselt number [-]
P	Pressure [Pa]
Pr	Prandtl number [-]

Q Heat transfer rate [W]

q Heat flux [$\frac{W}{m^2}$]

R Thermal resistance [$\frac{K}{W}$]

R_{wf} Contact resistance between wick and fins [$\frac{Km^2}{W}$]

r_{wp} Pore radius [m]

Re Reynolds number [-]

T Temperature [K]

t Thickness [m]

U Global heat transfer coefficient [$\frac{W}{m^2K}$]

W Width [m]

x Vapor quality [$-$]

z Length [m]

Greek

α_{ev} Evaporation coefficient [$-$]

α_v Homogeneous void fraction [$-$]

β Volume fraction of liquid in the compensation chamber [-]

δ Film thickness [m]

ϵ Porosity [-]

λ Thermal conductance [$\frac{W}{K}$]

μ Dynamic viscosity [Pas]

ϕ Friedel two-phase multiplier [$-$]

ρ Density [$\frac{kg}{m^3}$]

σ Surface tension [$\frac{N}{m}$]

θ	Contact angle [°]
ε	Error [$-$]
ϑ	Energy imbalance [W]
ζ	Friction factor [$-$]

Subscript

amb	Ambient
b	Base plate
b	Body
c	Casing
cap	Capillary
cc	Compensation chamber
cnd	Condensation length
$cond$	Condenser
ev	Evaporation
$evap$	Evaporator
f	Fluid
g	Gas
i	Inner
l	Liquid
lim	Limit
ll	Liquid line
$load$	Load
m	Meniscus

nuc	Nucleation
o	Outer
sat	Saturated
sc	Subcooler
$sink$	Sink of condenser
v	Vapor
vg	Vapor grooves
vl	Vapor line
w	Wick

Contents

1 Introduction and Literature Review

The worldwide demand for computing performance of electronic devices is continuing to increase due to the expanding digital society, resulting in increased electricity consumption of data centers. Studies project that the share of global electricity usage of the data center sector will be between 3-13% in 2030 [1–3]. About 40% of the total energy consumption inside these data centers is associated with IT cooling equipment, where a major part belongs to CPU cooling [4–6]. The combination of exponential growth in the amount of stored and processed data and an increasing trend of CPU thermal design power makes that managing the power consumption of data centers has a certain concern [7]. To improve the environmental footprint and to give the data center sector a more sustainable future, it is important to unlock new-generation cooling systems in data centers that have the ability to efficiently dissipate CPU heat and re-use it. This chapter reveals the state-of-the-art of current CPU cooling techniques and aims to identify a research gap in the latest development of advanced cooling systems.

1.1 Data center cooling techniques

Traditionally, data center cooling infrastructure uses aligned racks with hot aisle/cold aisle configuration placed on a raised floor. As shown in figure 1, the cold aisle is formed in a way that the front of the aligned server racks face each other, whereas the rear end of the server racks is placed in the hot aisle. In the setup, servers are directly cooled with cold air generated by a computer room air conditioning (CRAC) unit that enters the cold aisle through a perforated raised floor. This infrastructure requires small fans inside the server to create airflow between both aisles. The exhausted hot air at the back of each rack is usually drawn by the CRAC unit compressor and cooled by a refrigerant.

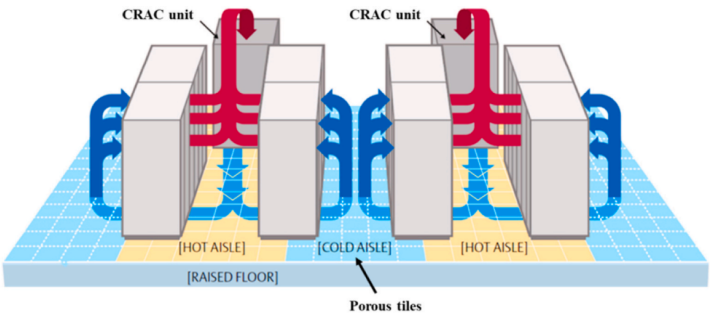

Figure 1: Hot aisle/cold aisle configuration [8]

Since the power density of CPUs is continually increasing and air-cooling has its limitations (e.g. a low heat capacity, the usage of small energy-consuming fans, and non-reusable heat), other more efficient thermal management techniques become essential [9]. A literature review by Zhang et al. distinguished four main categories for promising energy-saving cooling techniques in data center applications, namely free cooling, thermal energy storage (TES) based cooling, single-phase liquid cooling, and two-phase cooling [8]. The first two methods are mainly focused on energy reduction by cooling the exhausted hot air that leaves server racks. A free cooling method uses a natural source (ambient air or water) to directly or indirectly cool hot air. The improvement of this technique is restricted by the data center location and the sensitivity of energy supply fluctuation [10]. TES-based cooling could store the heat by using physical or chemical storage and so avoid the energy supply mismatch and increase the reliability and energy efficiency of data center facilities [11]. However, both methods should be combined with single-phase liquid cooling or two-phase cooling to get away from the energy-consuming small fans inside the servers. In recent years, the development of single-phase liquid cooling has resulted in various techniques such as liquid cold plates, direct-to-chip cooling, and single-phase immersion cooling. This proven technique shows significantly higher heat transfer performance than conventional air cooling systems [9, 12].

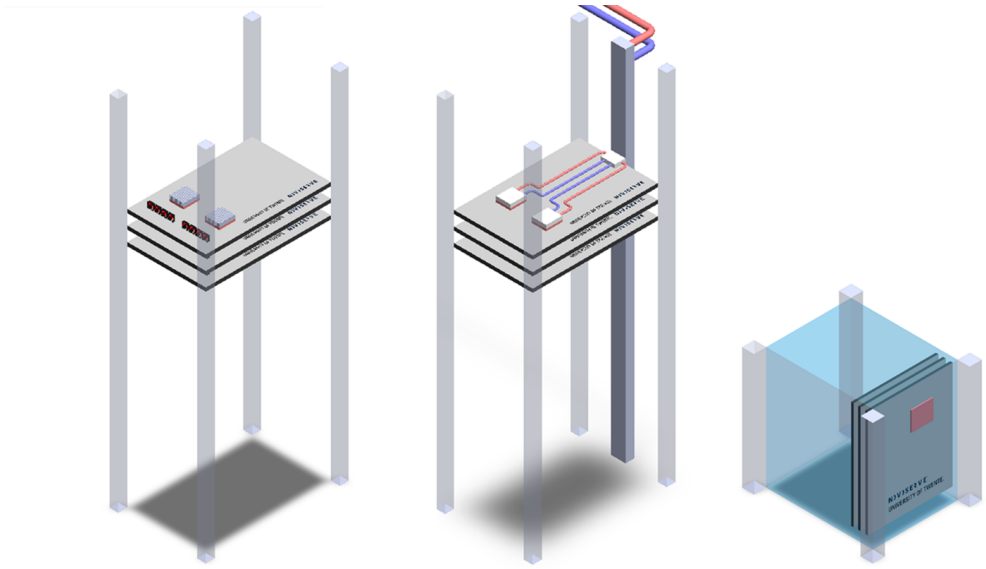

Figure 2: Server rack configuration: air cooling, heat-pipe based cooling and immersion cooling

Nevertheless, a literature review by Zhang et al. concluded that two-phase cooling techniques are more efficient than single-phase systems [8]. This is important to satisfy the continually increasing power density of electronic components like CPUs. The two-phase technique refers to a cooling system where the working fluid is circulated through a closed loop and utilizes the latent heat of a working fluid to dissipate heat. Promising ways for two-phase electronic cooling applications are heat-pipe-based cooling and immersion cooling [13]. As seen in figure 2, heat pipe-based solutions are concentrated to dissipate heat from local hot spots, where in immersion cooling complete servers are submerged into an enclosed dielectric bath. In general, both are passive cooling systems (no active pump or fan), which have several advantages in terms of higher reliability, less maintenance, noise reduction and better energy efficiency.

1.2 Loop heat pipe

Heat pipe-based cooling solutions utilize the evaporation and condensation of a working fluid to transfer heat by making use of capillary force. This capillary force is created by a porous wick structure. Studies show that traditional heat pipe-based methods such as conventional heat pipes, pulsating heat pipes or vapor chambers have limited heat transport capacity and therefore are insufficient to use in data center server applications [14, 15]. Alternately, a reliable passive solution that can transport heat on relatively long distances is a loop heat pipe (LHP). The loop heat pipe, invented in 1972 by Gerasimov and Maydanik, utilizes a porous wick structure in the evaporator as a capillary pump to enable the circulation of vapor and liquid through the loop [16]. All evaporators include an active zone that houses a wick structure, vapor removal channels to collect and transport vapor and a compensation chamber to establish the operation pressure and temperature in the system. As seen in figure 3, a vapor and liquid line connect the evaporator to the condenser section where heat is rejected. In the first years of LHP development, cylindrical evaporators with flat thermal interfaces were used for semiconductor applications. The increasing CPU power density required a more efficient design with larger thermal contact so Maydanik et al. developed the first flat-shaped evaporator in 1995 [17]. Over the years, the technique of flat-shaped loop heat pipes has advanced rapidly. Several parameters such as evaporator design, wick material and working fluid are varied and analyzed in numerous papers [18].

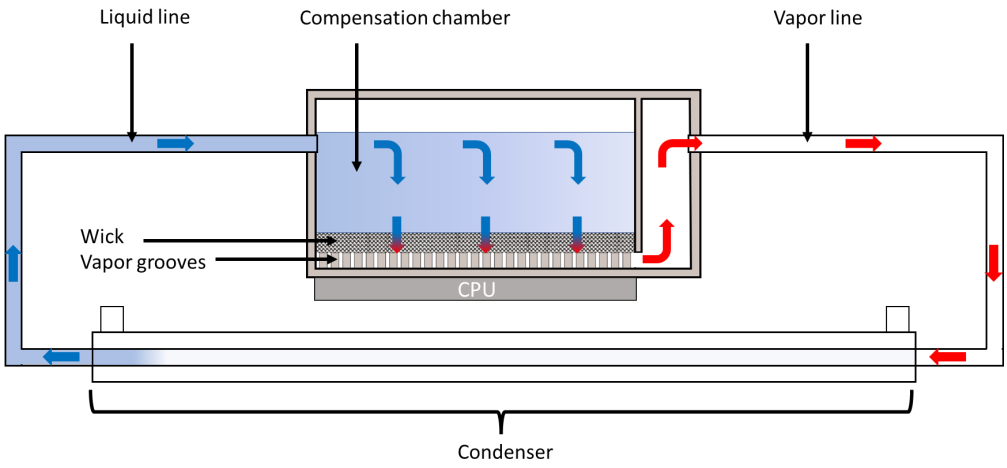

Figure 3: Global working principle of LHP

1.3 Additive manufactturing

Literature observes that the development of flat-shaped evaporators arbitrarily can be divided into evaporators with opposite replenishment (EOR) and longitudinal replenishment (ELR) [19]. In the case of EOR the compensation chamber is placed on top of the wick, in contrast to ELR where the compensation chamber is designed longitudinal to the wick. The latter is frequently used for applications where height is limited. A comparison test by Maydanik et al. concludes that an ELR design has lower operation temperature and lower thermal resistance for high heat flux. However, the report also shows that an evaporator with opposite replenishment is more compact for the same active zone area as an ELR design. This is important for data center applications since the space around the active zone area (CPU) is constrained [20, 21]. Despite the advantages of loop heat pipes, a review by Szymanski et al. shows there still exist some challenging aspects [22]. The frequent reliability problem of flat-shaped evaporators is caused by improper sealing between the wick and casing structure. A recent development to prevent loop heat pipes from sealing failure makes use of additive-manufactured wicks. Typically, wick structures are made of sintered powders. By using selective laser melting (SLM) technique, powders are melted layer-by-layer, whereby a hermetic seal between casing and wick can be provided. An additional benefit compared to conventional sintered wicks is higher design freedom of the wick, higher heat transfer capability, low thermal resistance and the improvement of capillary performance [23–25]. Further, the amount of machine steps is reduced which could have a positive impact on production costs.

There are some studies available on the determination of 3D-printed wick specifications as seen in figure 4. Esarte et al. utilized the SLM technique to fabricate a stainless steel (316l) grid structure [26]. They executed a permeability and conductivity test of the sample which resulted in a permeability value yielding 1.25×10^{-12} m^2 and an effective thermal conductivity of the wick equal to 1.48 W/mK. The mean pore radius of the wick was 80 µm and the porosity was 0.17 The authors concluded that the test sample has poor capillary performance using distilled water as a working fluid due to its high contact angle (90 °). Another study on additive-manufactured wicks was conducted by Hu et al. [27]. Their research was focused on 3 different SLM printed stainless steel grid samples, where the structure with the best heat transfer performance has a pore radius, a porosity, an effective thermal conductivity and a permeability of respectively, 109 µm, 0.509, 5.38 W/mK and 2.13×10^{-10} m^2. The value for the static contact angle between water and the wick surface was not given. The third investigation was performed by Jafari et al. [24]. The authors developed an SLM stainless steel wick by the formation of 3D octahedral unit cells. The mean pore radius, porosity and permeability are 108 µm, 0.46 and 1.305×10^{-10} m^2. The contact angle and effective thermal conductivity were defined in an earlier study on the same test sample and are equal to 56.8° and 6 W/mK [28]. Furthermore, Robinson et al. produced an additive manufactured aluminum wick structure with a pore radius of 88 µm, a porosity equal to 0.59 and the permeability tested on 4×10^{-11} m^2 [25]. The effective thermal conductivity was estimated using Alexander correlation, where the thermal conductivity of aluminum k_w is 125 W/mK.

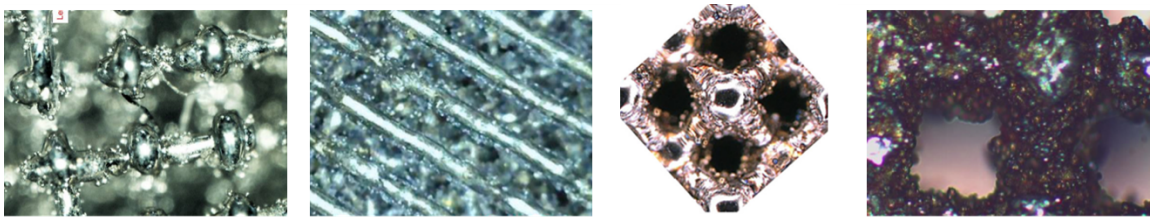

Figure 4: Optical images of additive manufactured wick structures. (a) Stainless steel grid structure by Escarte et al. [26] (b) Stainless steel grid structure by Hu et al. [27]. (c) Stainless steel octahedral structure by Jafari et al. [24]. (d) Aluminum grid structure by Robinson et al. [25].

To the author's knowledge, additive manufactured wick structures only have been applied on cylindrical evaporators with flat thermal interface or flat disk-shaped loop heat pipes [22, 29]. In a cylindrical design, the thermal contact area is a problem for CPUs where in the case of a disk-shaped evaporator, some portion of the evaporator will be useless for the rectangular-shaped CPU's [30]. The development of a new selective laser melting EOR-type evaporator with a rectangular design could be an important breakthrough in thermal management systems.

1.4 Modelling loop heat pipes

Historically, research on loop heat pipes is concentrated on experimental investigations [18, 19]. Nevertheless, to predict the thermal performance and operational limitations numerical modeling of the design is of major importance. Especially for additive manufactured wicks - where there is wide design freedom - a numerical model can be useful to optimize the structure. Due to the complexity of the related two-phase heat transfer phenomena, LHP modeling efforts are mainly focused on simplified steady-state energy balance equations. Siedel et al. observed that only a few steady-state models describe the LHP operation for flat evaporators with opposite replenishment [31]. For cylindrical-shaped evaporators Kaya et al. developed an analytic model based on steady-state energy balance equations at each component of the system [32]. From this model, Adoni et al. evolved a thermal and hydraulic steady-state model that can be used for flat evaporators with opposite replenishment [33]. Their model can estimate the performance of a loop heat pipe with a two-phase or hard-filled (only subcooled fluid) compensation chamber by simultaneously solving ordinary differential equations that describe the heat transfer and pressure drop inside the transport lines and condenser section using a sixth-order Runga-Kutta Method. This approach is useful for getting an accurate estimate of the pressure drop inside the system, especially for additive-manufactured wick structures where the pore radius and capillary limit are often smaller than conventional heat pipes due to current fabrication limitations. The model can predict the operation curve in good agreement with experimental data, however, it has limitations in describing the heat transfer in the evaporator area. Adoni et al. use an empirical obtained thermal conductance value to obtain heat leakage through the evaporator casing and describe heat transfer through the wick by solving a 1D-energy balance [34]. An analytical model by Siedel et al. describes this heat leak based on 2D Fourier series expansion, where it only depends on the geometry and thermal conductivity of the wall or wick structure [31]. Both could be optimized to

minimize the leak, due to the extensive ability of 3D printing. Siedels model also includes a thermal resistance between the wick and grooves which is interesting since additive manufactured loop heat pipes could be made of one entire material and so without contact resistance. Nevertheless, the authors evaluate that the model has limitations in predicting heat transfer in transport lines and condenser section [35]. The combination of two existing models could create one improved steady-state numerical model that accurately describes the heat and mass transfer within the entire LHP system and could be used to predict the performance enhancement and feasibility of additive-manufactured evaporators.

1.5 Two-phase immersion cooling

Fabrication of SLM-printed porous and microchannel structures could also be interesting in two-phase immersion cooling applications. This immersion cooling technique involves and two-phase heat transfer process when the surface temperature of the electronic component exceeds the liquid vaporization temperature. At this point, bubbles are formed and rise up to a condenser section above the bath where heat is rejected. The liquid-vapor phase change of the working fluid can be described by the boiling curve in figure 5, where a relation is given between surface heat flux and the degree of superheating.

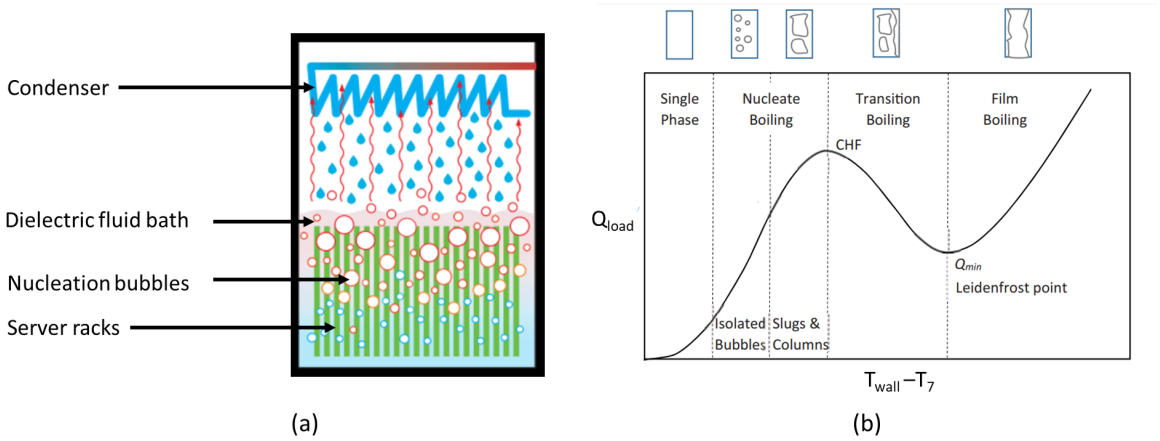

Figure 5: Two-phase immersion cooling (a) Global working principle of two-phase immersion cooling. (b) Typical boiling curve and flow patterns [36, 37].

The formation of bubbles starts at the nucleate boiling stage and ends when the critical heat flux is achieved. Chen et al. outlined that increasing this critical heat flux and decreasing the degree of superheating will enhance the cooling performance [38]. Both could

be achieved by selecting an appropriate working fluid and modifying the surface. A literature review on surface modification by Kang et al. concluded that an expanded surface area increases the number of nucleation sites and so proportionally increases the cooling performance [39]. A way to increase the area of the heating surface is by covering it with microchannels, fins, porous layers, texturing or small fins. Typically, these structures are manufactured using sintering powders or laser texturing [40]. Recent developments by Liu et al. and Zhang et al. show that SLM-printed grooved and porous structures could increase the CHF and heat transfer coefficient [41, 42] compared to solid plain surfaces. This effect is also obtained for additive manufactured microchannels and pin-finned structures [43, 44]. The SLM-printed loop heat pipe evaporator contains microchannels (vapor removal grooves) and a lattice (wick) structure. To the author's knowledge, there is no former research work into the pool boiling heat transfer enhancement of an additive manufactured combination of microchannels and lattice structure. The present work will evaluate the pool boiling behavior of microchannels and a combination of microchannels and lattice structure for low heat flux (<8 $\frac{W}{cm^2}$).

1.6 Research goal

In summary, the design and manufacture of new materials and surface properties is a powerful approach to enhancing the performance of two-phase cooling systems for data centers. However, to date there is limited knowledge about to address the following research gap: "To what extent does the surface microstructure of additive manufactured printed materials and surface properties dictate the performance of particular two-phase cooling?" The project will develop the guiding principles for the design and advanced manufacturing of two-phase cooling systems for data centers and is executed together with Dutch Infrastructure-as-a-Service (IaaS) company NovoServe B.V. and the University of Twente. The IaaS business case provides the hosting of storage, network and servers. The company accommodates the maintenance of these resources for several clients with various requirements. Since user requirements occasionally change, there is relevance to developing a new generation cooling system where maintenance on the individual server level is achievable and without changing the entire infrastructure. For that reason, NovoServe B.V. has a special interest in advanced passive heat pipe-based solutions that can transfer heat from the CPU to the back of the server.

1.7 Structure of report

The project is divided into the 3D printing performance enhancement of 2 different two-phase cooling techniques, respectively, loop heat pipes (Chapters 2-4) and immersion cooling (Chapter 5).

To answer the main question the report is divided into different chapters where several sub-questions are investigated.

Chapter 2.

- What are the operating principles, thermal-hydraulic behavior and limitations of LHPs during operation and how to sustain this thermal-hydraulic behavior?

Chapter 3.

- How to improve the existing steady-state numerical model for flat loop heat pipes with opposite replenishment?
- To what extent does the improved numerical model agree with experimental research from the literature?
- What is the numerically predicted influence and enhancement of additive manufacturing on the LHP compared to conventional manufactured loop heat pipes?

Chapter 4.

- To what extent could a new additive-manufactured LHP prototype be designed within the prescribed design restrictions?
- What is the printing quality of a 3D-printed wick structure within the selective laser melting evaporator?
- How can the prototype be tested in a way that is suited for experimental and practical approaches?

Chapter 5.

- What is the effect of additive-manufactured stainless steel microchannels and a combination of a lattice structure including microchannels on the pool boiling behavior of distilled water under atmospheric pressure?

Designing a proper loop heat pipe requires a detailed explanation of working principles, behavior and limitations of loop heat pipes during operation, given in chapter 2. Knowing this operation behavior is essential in developing a steady-state numerical model. In Chapter 3 an existing numerical model will be improved and validated by experimental research. This model is also used to compare the predicted performance of additive-manufactured heat pipes to conventional loop heat pipes. In the next chapter, a prototype is fabricated based on the predicted values in the numerical model. The chapter also contains a microscopic analysis to check the printing quality and describes the way to test the loop heat pipe prototype for experimental and practical purposes. For two-phase immersion cooling applications (Chapter 5), this prototype is also used for a pool boiling test. Hereby, the heat transfer performance of microchannels and a combination of microchannels and lattice structure is tested for low heat fluxes. The results of the pool boiling test and the numerical model are discussed in Chapter 6. The report concludes with the main findings and recommendations of the project.

2 Loop heat pipe operation

Loop heat pipes are known for their high efficiency, high reliability and maintenance-independent advantages. The passive cooling technique is also known as complex due to its two-phase phenomena. Designing a proper LHP with all advantages requires a deep understanding of this complex two-phase operation and its underlying principles. In the first part of this chapter, a comprehensive description of working principles and limitations is given to get knowledge about the main principles of operation. The chapter's second part focused on the thermal-hydraulic characteristics of a LHP. This knowledge helps to prevent issues such as poor start-up, overheating and inefficient heat dissipation.

2.1 Operation principles

The first section aims to offer a detailed insight into the working principles of a loop heat pipe and their limitations. Understanding these general principles is crucial for developing a new loop heat pipe design.

2.1.1 Working principle

The thermodynamic phase change of the working fluid inside a LHP can be described using the schematic pressure-temperature diagram given in figure 6. Operation starts by evaporation of the working fluid at the interface between superheated liquid in each pore of the wick and vapor in the grooves. The evaporation at this interface (also known as meniscus) will lead to saturated vapor in the grooves (1). From this point, the vapor moves through the grooves driven by the pressure difference between the evaporator and condenser section. The saturated vapor is slightly superheated by absorbing heat from the fin and undergoes a small pressure drop due to friction (1-2). In the next stage, a vapor line is used to transport the working fluid to the condenser (2-3). There is a frictional pressure drop and a temperature drop induced by a lower ambient temperature. Once in the condenser section, vapor condensates into saturated liquid and there will be a two-phase frictional and acceleration pressure drop (3-4). As condensation is completed, the liquid starts to subcool by releasing more heat from the condenser (4-5). In this subcooler section, there will be a single-phase frictional pressure drop. Subcooling is necessary to ensure the absence of vapor in the liquid line. The working fluid in this returns back to the compensation chamber and is subjected to a friction pressure drop (5-6). Depending on the subcooled temperature and the ambient temperature, the working fluid temperature

will drop or rise inside the liquid line. The subcooled fluid that flows into this chamber is heated by the evaporator wall and wick structure till it reaches the wick inlet as fully saturated liquid (6-7). The fluid in this compensation chamber (also known as a reservoir) is in equilibrium with saturated vapor that is filling the remaining space [45].

The more complex part of the thermodynamic loop occurs inside the wick structure (7-8). From the wick inlet in point 7 to the liquid side of the meniscus at point 8 the fluid moves through the wick in metastable condition. During operation the applied heat is conductively transported through the fin and thereafter through the wick structure. Usually, the liquid starts to boil if the vapor pressure inside a bubble exceeds the ambient pressure on the bubble. Instead, the surface tension of the small pore size channels inside the wick creates additional pressure on the bubble, preventing the liquid from boiling. This phenomenon creates a superheated liquid inside the wick structure. The temperature between the wick inlet T_7 and outlet T_1 will be approximately equal, besides there is a hydraulic pressure drop inside the wick P_8 - P_7. Note that the P-T diagram is magnified since the loop heat pipe operates at the steep part of the saturation line [34].

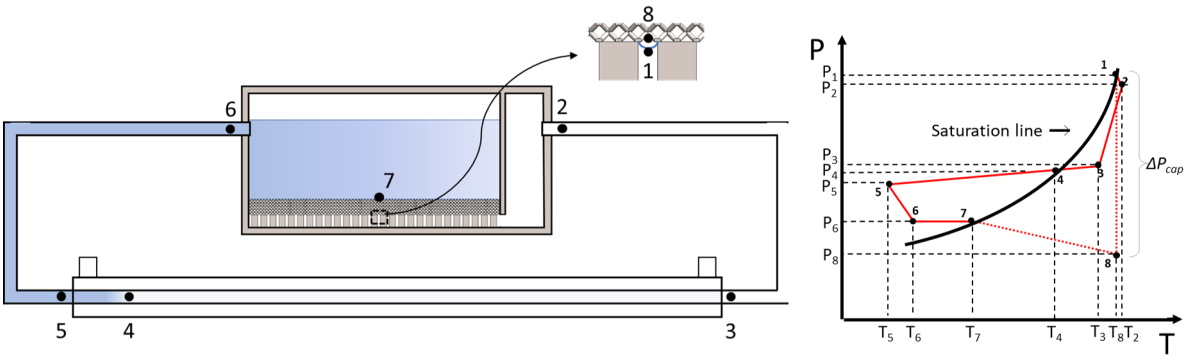

Figure 6: Schematic P-T diagram of the two-phase flow inside the loop heat pipe.

2.1.2 Limitations

At the meniscus along the wick capillary pressure arises due to the interfacial tension between the fluid phases and the surface tension between fluids and the porous medium (8-1). According to the Young-Laplace equation for static interfaces (eqn. 1), the radius of this meniscus r_m is inversely proportional to the capillary pressure of the system. Since the meniscus radius cannot exceed the pore radius of the wick, the maximum capillary limit

depends on the pore size of the wick $r_{w,p}$. The Young-Laplace expression also implies that the capillary capability relies on the surface tension of the working fluid σ_1 and the contact angle between the wick and working fluid θ [46].

$$\Delta P_{cap,lim} \geq \frac{2\sigma_1 cos(\theta)}{r_m} \quad \Rightarrow \Delta P_{cap,lim} = \frac{2\sigma_1 cos(\theta)}{r_{wp}} \tag{1}$$

To ensure flow circulation inside the LHP, the capillary pressure should be larger than the total pressure drop inside the system (see eqn. 2). Note that this equation does not involve the gravitational pressure drop and pressure drop induced by the grooves, since both are supposed to be zero in this case.

$$\Delta P_{cap,lim} > \Delta P_{vl} + \Delta P_{cond} + \Delta P_{sc} + \Delta P_{ll} + \Delta P_w \tag{2}$$

In addition to the capillary limit, it is important to avoid the formation of bubbles inside the wick structure. These bubbles could create a blanket of vapor inside the wick structure which prevents saturated liquid from entering the wick and so it halts the circulation of the system. As described in section 1.5, the formation of bubbles starts at the nucleation boiling stage, at a certain heat load when the surface temperature is sufficiently higher than the saturated fluid temperature. In the case of a loop heat pipe, the transverse heat load through the wick structure should not exceed the load when nucleation starts [45, 47]. For porous wick structures boiling limit can be described with equation 3, where r_{nuc} is the nucleation site radius of working fluid [48].

$$Q_{boil} = \Big(\frac{A_w k_{we} T_1}{h_1 \rho_1 t_w}\Big)\Big(\frac{2\sigma_1}{r_{nuc}} - \Delta P_{cap,lim}\Big) \tag{3}$$

In summary, the underlying thermodynamic working principles for loop heat pipes are rather complex, especially in wick structures. The metastable condition of the working fluid inside the wick enables the capillary pressure that is the key parameter in loop heat pipe operation. It is important to mention that the system only operates when the capillary limitation is higher than the overall pressure drop and the applied heat load does not exceed the boiling limit.

2.2 Operating characteristics

The operation characteristics encompass several key aspects, including the start-up principles, operation mode and reliability. A comprehensive overview of these characteristics helps to understand the thermal-hydraulic behavior of the loop heat pipe.

2.2.1 Start-up

To use a loop heat pipe for practical applications a rapid and smooth start-up is essential. The start-up is defined as the time before the working fluid inside the LHP reaches its steady state value. This transient phenomenon can be complex since it depends on various parameters. Research shows that at the beginning of operation, a temperature overshoot inside the reservoir occurs. Overshoot can be explained as the difference between maximum transient temperature and steady-state temperature. It can be problematic if the temperature reaches a value outside its allowed temperature range (in this case the maximum CPU temperature) [49]. Another issue during start-up could be the absence of nucleate boiling. For cases where vapor grooves are flooded with liquid, a superheat of liquid is needed to initiate nucleate boiling and so dispose of all undesired liquid in grooves. Defining the exact amount of required superheat is rather complex as nucleation boiling is influenced by several parameters [50, 51]. However, Ku concluded that the initiation of nucleate boiling can be advanced by adding a higher initial heat load. Further, a succeeded operating LHP is sufficiently filled with liquid through the entire loop [49]. Bai et al. mathematically show that for cases where vapor grooves are not flooded, the influence of the thermal capacity of the evaporator during the start-up process is negligible even as the effect of sink temperature. In addition, it is observed that a higher ambient temperature increases the start-up time [50].

2.2.2 Variable and Fixed Conductance Mode

Numerous experimental tests on loop heat pipes observe a relationship between the operation temperature and the applied heat load [52, 53]. Typically as seen in figure 7 (a,b), LHP operation is divided into two modes: the variable conductance mode (VCM) and the fixed conductance mode (FCM) [53]. In the first mode, the operating temperature decreases or remains constant when increasing the heat load. The heat input results in a partially utilized vapor in the condenser section (see fig. 7) correspondingly, the working fluid is subcooled close to the sink temperature. If the sink temperature is lower than the ambient temperature the fluid will gain ambient heat in the liquid line. Increasing the heat

load - which proportional increases the mass flow and decreases the residence time - will reduce the amount of attained ambient heat in the liquid line. This reduced quantity of gained heat in the liquid line creates a decreasing operating temperature in the reservoir to ensure heat balance in the reservoir. The slope of this operating curve in VCM mode (flat or decreasing) strongly depends on the heat exchange between the reservoir/liquid line and ambient. Launay et al. describe that for low-thermal-conductivity wicks with low-pressure working fluids a flat shape is observed [54]. Ku shows that an increasing temperature difference between the sink and the ambient increased the slope in the variable conductance mode [55]. At a certain heat load, the full condenser length is only used for utilizing vapor. From this point, the LHP operates in the fixed conductance mode and the operation temperature increases quasi-linear with heat load.

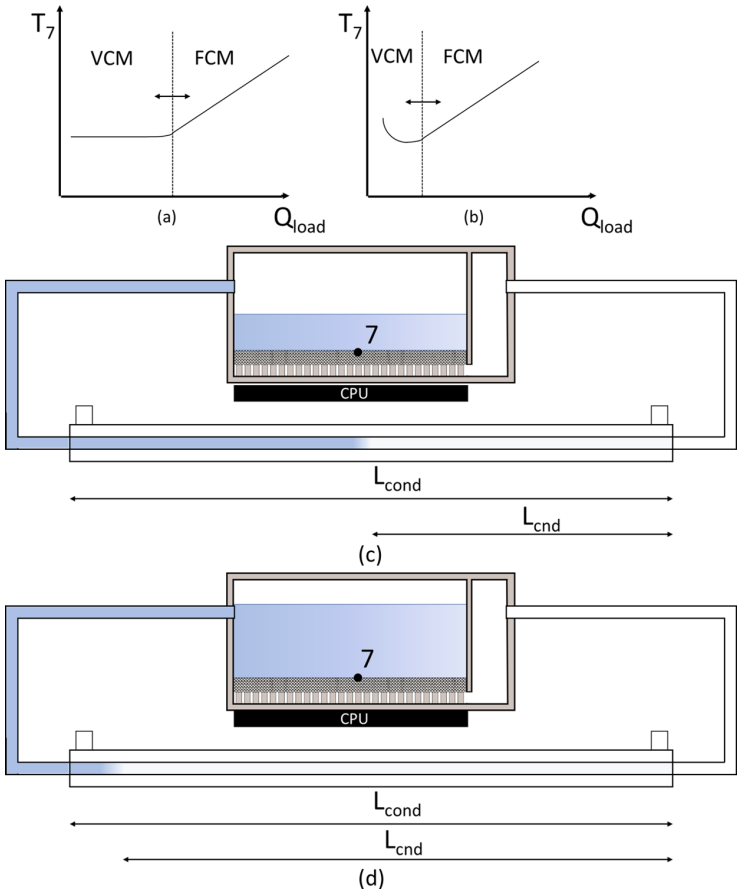

Figure 7: (a) Flat-shaped operation curve. (b) U-shaped operation curve. (c) Variable conductance mode. (d) Fixed conductance mode.

2.2.3 Condensable gasses

The lifespan and reliability of loop heat pipes can be degraded by the existence of non-condensable gases (NCG) inside the LHP [56, 57]. These gases are generated by chemical reactions inside the LHP. Experiments show that NCG results in a higher steady-state operation temperature due to the accumulation of gas inside the reservoir and an increase in system pressure. The existence of relatively high partial pressure of NCG also leads to an increase in start-up time [56, 58]. These gases are mainly generated by a chemical reaction between the working fluid and imperfections of the loop heat pipe material. Poor machining and cleaning of the evaporator could lead to glitches in the wick structure and oxidation at the wick surface [45]. In Appendix A.1 it is shown which combinations of working fluid and LHP materials are incompatible. The presence of different wick and evaporator materials in conventional loop heat pipes could also lead to a chemical reaction. Printing the entire structure with one material - as the case in this project - will avoid this issue. Li et al. evaluate that NCG can be removed by evacuating the system and working fluid before filling [59].

In brief, designing an efficient and reliable heat pipe depends on various parameters. It was observed that the start-up behavior of loop heat pipe is a complex phenomenon that relies on the geometry (are the grooves filled with liquid or not) and the amount of nucleation boiling. A proper start-up is essential to prevent the system from temperature overshooting. Further, it was observed that the thermal-hydraulic behavior of loop heat pipes can be distinguished in 2 operation modes depending on the ambient temperature, sink temperature and condenser length. Finally, this section showed that the presence of non-condensable gasses and the choice of incompatible materials have a negative effect on the lifespan and reliability of loop heat pipes.

3 Numerical model loop heat pipe

As described in chapter 2 the LHP operation curve and limitations depend on various parameters. Having an accurate steady-state numerical model is an often used way to design, simulate and evaluate this thermal behavior and performance. In this chapter, an improved steady-state numerical model will be revealed that combines an accurate heat transfer and pressure drop approach in the transport lines and condenser section based on the Runge Kutta method as described by Adoni et al. [33], together with precise 2D analytical solutions to model heat leak inside the evaporator as explained by Siedel et al. [35]. The newly developed model is validated using experimental results in the literature and a parametric analysis is conducted to identify the influence of several specifications on the operation curve. Finally, the model is used to estimate the performance enhancement and ability of additive manufactured loop heat pipes compared to an existing structure.

3.1 Modelling

The heat transfer process occurring in a flat evaporator with opposite replenishment can be described in figure 8. The applied heat load of the CPU (Q_{load}) is mainly utilized for heating the fluid inside the evaporator (Q_{evap}). A relatively small amount of applied heat load does not participate in the evaporation of fluid and refers to heat leak through the evaporator casing (Q_b). This heat travels by conduction through the wall and so exchanges heat to the fluid inside the compensation chamber (Q_{cc}) and to the surrounding environment (Q_{amb}).

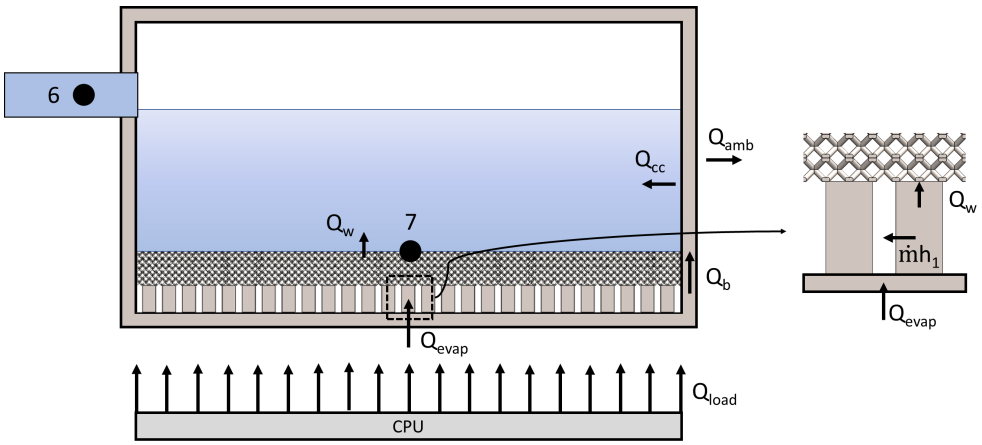

Figure 8: Schematic energy balance in the evaporator

$$Q_{load} = Q_{evap} + Q_b \tag{4}$$

$$Q_b = Q_{cc} + Q_{amb} \tag{5}$$

3.1.1 Evaporator casing

Adoni et al. use a prescribed thermal conductance value λ_b to obtain this heat leak through the wall [33]. They concluded that this thermal coupling between the evaporator and the compensation chamber has a significant influence on the shape of the operating curve. A more detailed approach that describes the heat leak path in the casing is presented by Siedel et al. [35]. This approach involved a 2D heat equation with 4 boundary conditions to obtain a temperature field and so the heat leaks through the evaporator body (Appendix B.1). The method is based on 2D Fourier series expansion, where the rectangular evaporator casing is divided into two fields.

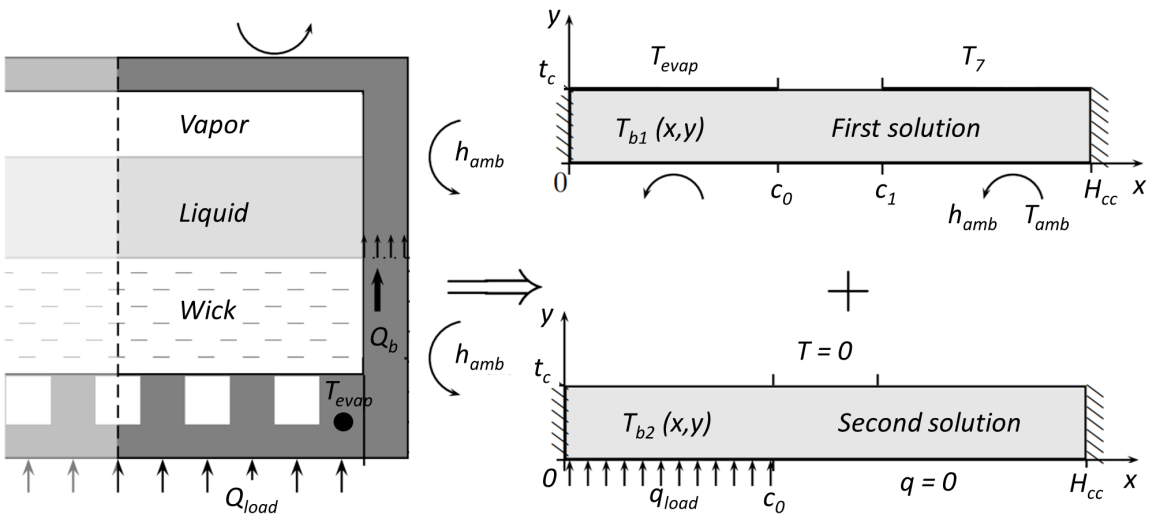

Figure 9: Modeling evaporator casing [35]

As illustrated in figure 36, the first profile corresponds to the temperatures at the inner side of the casing. Both ends are supposed to be adiabatic due to symmetry and there will be convective heat transfer with ambient (h_{amb}) at the entire external evaporator surface. The points c_0 and c_1 represent respectively the height of the base plate and grooves (c_0 = H_b + H_{vg}) and this height together with the wick thickness (c_1 = c_0 + t_w). The inner side of the casing has two fixed temperatures, namely the evaporator temperature ($0 \leq x \leq c_0$) and the liquid/vapor bulk temperature of the compensation chamber ($c_1 \leq x \leq H_{cc}$).

To simplify the model, the compensation chamber bulk temperature will be equal to the saturated liquid temperature (T_7) inside this reservoir, however, it must be noted that in actual situations the working fluid temperature distribution varies along the inner side of the casing. Between $c_0 \leq x \leq c_1$ the temperature is supposed to be linear. The second temperature profile adds the applied heat flux ($q_{load} = \frac{Q_{load}}{A_w}$) to the inner casing/fin interface ($0 \leq x \leq c_0$). Considering symmetry means that both ends are adiabatic. The next boundary condition involves the absence of heat input at the entire surface excluding the mentioned interface. An expression based on the 2D Fourier series is used to sum up both profiles and create a general expression of the non-dimensional temperature field. As noted in Appendix B.1, integrating this equation (Fouriers law) at $y = H_{cc}$ leads to a formula for heat leak (eqn. 6), where B_1, B_2, B_3 are coefficients independent of T_{evap} and T_7. Also, the heat that leaks to the ambient is expressed with coefficients (eqn. 7). The exchanged heat between the wall and compensation chamber Q_{cc} is obtained by subtracting equation 6 and 7 to the fluid inside the compensation chamber.

$$Q_b = B_1 T_7 + B_2 T_{evap} + B_3 \tag{6}$$

$$Q_{amb} = B_4 T_7 + B_5 T_{evap} + B_6 \tag{7}$$

$$Q_{cc} = Q_b - Q_{amb} \tag{8}$$

3.1.2 Wick modeling

The heat transmitted to the fluid in the evaporator (Q_{evap}) is primarily used to evaporate the liquid at the fin/wick interface (Q_{ev}). It is assumed that the vapor inside the grooves is not superheated and evaporation only depends on the latent heat ($\dot{m}h_7$). A smaller part of this heat leaks into the wick structure (Q_w), whereas it results in convective and conductive heat exchange inside the wick and heat leak to the compensation chamber. Considering the heat of evaporation ($\dot{m}h_7$) is much larger than heat leak through the wick structure, the mass flow rate is estimated using equation 10 [33, 34].

$$Q_{evap} = Q_{ev} + Q_w = \dot{m}h_1 + Q_w \tag{9}$$

$$\dot{m} = \frac{Q_{evap}}{h_1} = \frac{Q_{load} - Q_b}{h_1} = \frac{Q_{load} - (B_1 T_7 + B_2 T_{evap} + B_3)}{h_1} \tag{10}$$

Adoni et al. solved a 1-D energy balance for porous media to obtain the heat leak through the wick structure with the assumption that heat and mass flow are in transverse direction

[33]. An important boundary condition in this procedure is that the temperature below the wick equals the saturated vapor temperature T_1. Nonetheless, in practical situations, a significant portion below the wick consists of a groove/wick interface that influences the temperature distribution inside the wick. A more precise 2D method is used by Siedel et al. [35]. As seen in figure 10, a segment of the porous wick structure is selected to predict the heat transfer across the wick. At the interface between grooves and wick ($y = 0$), this area involves one-half side of the fin ($a_0 = \frac{W_f}{2}$) between $0 \leq x \leq a_0$ that contains the evaporator temperature corrected for thermal contact resistance between fins and wick ($T_{evap,w}$). The other interval ($a = \frac{W_f + W_{vg}}{2}$) represents one-half side of the groove and consists of the saturated vapor temperature T_1. The model also includes a micro-region between the groove and fin where intensive evaporation occurs ($a_0 \leq x \leq a_1$).

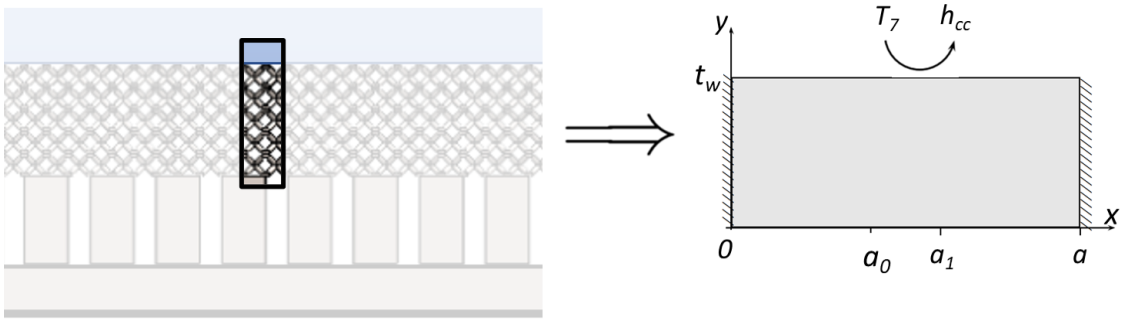

Figure 10: Modeling wick structure [35]

Siedel et al. suppose a linear temperature profile in this micro-region area and so consider that the slope of this temperature gradient is related to the heat transfer coefficient at the liquid-vapor interface and the length of this region ($a_0 \leq x \leq a_1$) [60]. The size of this region is estimated using equation 77, where k_{we} and h_{ev} are respectively, the effective thermal conductivity of the wick structure and the heat transfer coefficient of evaporation [35].

$$a_1 - a_0 = \frac{k_{we}}{h_{ev}} \tag{11}$$

The effective thermal conductivity accounts for conduction through solid and liquid and could be obtained using different correlations depending on fabrication, porosity, working fluid and microstructure geometry of the wick structure [28, 61]. The heat transfer coefficient is obtained using the kinetic gas theory, where a_{ev} is equal to the evaporation coefficient. This evaporation coefficient is an essential parameter to predict the performance of a loop heat pipe, however, several studies also indicate that the determination of

this coefficient depends on various parameters. A study by Marek and Straub concluded that surface-active substances and impurities of the working fluid and small contamination of the surface could reduce the evaporation significantly [62]. An empirical literature review by Eames et al. concludes that this coefficient will be in a range between 0.01 and 1 for water as a working fluid [63]. For dynamically renewing water surfaces - which is theoretically the case at the wick interface - Marek and Straub explain that the coefficient will exceed 0.1 [62].

$$h_{ev} = \frac{2a_{ev}}{2-a_{ev}} \frac{\rho_1 {h_1}^2}{T_1} \left(\frac{2\pi \bar{R} T_1}{\bar{M}} \right)^{-0.5} \left(1 - \frac{P_1}{2\rho_1 h_1} \right) \tag{12}$$

At the top side of the wick ($y = t_w$), the structure is bordered by the liquid bulk temperature, where both side walls are treated as adiabatic due to symmetry. It is supposed that this bulk temperature is equal to the saturated temperature T_7. The heat transfer between wick and saturated bulk is obtained using a heat transfer coefficient h_{cc}. According to Siedel et al. this parameter is empirically determined by experimental results [35]. The mathematical procedure is slightly different than the 2D approach that defines heat leaks through the evaporator body. As described in Appendix B.2, a standard non-dimensional temperature profile for solid structures is modified by changing the conductivity into an effective thermal conductivity for porous structures. However, this modified temperature field based on 2D Fourier expansion only depends on conduction through the wick and so excludes the liquid flow inside the porous structure. Assuming a 1D liquid flow in the wick structure and so considering a homogeneous volumetric source in the opposite direction of the heat transfer, create an extra non-dimensional temperature profile that describes the convection in the wick structure. By using the superposition principle, the convective and conductive temperature profiles can be added together into one non-dimensional temperature field. Integrating this profile over length $0 \leq x \leq \frac{a_0+a_1}{2}$ describes the total heat transfer through the wick (Q_{evap}) , where the integration over the interval $\frac{a_0+a_1}{2} \leq x \leq a$ results in the heat transfer related to evaporation (Q_{ev}). As described in Appendix B.2, both values can be expressed by coefficients independent of $T_{evap,w}$, T_1 and T_7. The amount of heat leak that enters the compensation chamber (Q_w) is obtained by subtracting both formulas.

$$Q_{evap} = B_7 T_7 + B_8 T_1 + B_9 T_{evap,w} \tag{13}$$

$$Q_{ev} = B_{10} T_7 + B_{11} T_1 + B_{12} T_{evap,w} \tag{14}$$

$$Q_w = Q_{evap} - Q_{ev} = (B_7 - B_{10}) T_7 + (B_8 - B_{11}) T_1 + (B_9 - B_{12}) T_{evap,w} \tag{15}$$

As mentioned the evaporator temperature at the wick interface is corrected for the contact resistance between the fins and the wick. Typically, the wick and fin/groove structures are fabricated separately and generate a thermal gap between both structures. An estimation of the contact resistance (R_{wf}) in heat pipe applications is given by Choi et al. and ranges between 3×10^{-4} to 7×10^{-5} Km^2/W [64]. Siedel et al. defined that the temperature at the wick side of the interface can be expressed using equation 16 [35], where A_f is the contact area between fins and wick structure.

$$T_{evap,w} = T_{evap} - \frac{R_{wf} Q_{evap}}{A_f} \tag{16}$$

At this point there are 4 unknowns (T_1, T_7, $T_{evap,w}$, T_{evap}) with 4 correlations (eqn. 4, 6, 13, 16). The solving procedure to obtain the evaporator temperature starts by combining equation 4 and equation 6 as expressed in equation 17. The heat transmitted to the evaporator, represented in equation 13, depends on the evaporator temperature at the wick interface ($T_{evap,w}$). By combining equation 13 and equation 16 the heat transfer through the evaporator can be defined with equation 18. Bringing both solutions together (eqn. 17 and 18) results in a general expression dependent on (T_1, T_7, Q_{evap}) as given in equation 19. The iteration of the numerical scheme starts by considering guess values for the saturated temperatures of the working fluid. As a result, the evaporator temperature can be iteratively obtained by solving equation 18 using the Newton-Raphson-Method [34, 65].

$$Q_{evap} = Q_{load} - B_1 T_7 - B_2 T_{evap} - B_3 \tag{17}$$

$$Q_{evap} = B_7 T_7 + B_8 T_1 + B_9 \left(\frac{R_{wf} Q_{evap}}{A_f} \right) \tag{18}$$

$$(B_1 + B_7) T_7 + B_2 T_{evap} + B_3 + B_8 T_1 + B_9 \left(T_{evap} - \frac{R_{wf}(Q_{load} - B_1 T_7 - B_2 T_{evap} - B_3))}{A_f} \right) - Q_{load} = 0 \tag{19}$$

Since the coefficients B_7, B_8 and B_9 to obtain the evaporator temperature depend on the mass flow rate and the mass flow rate - as showed in equation 10 - is obtained by the evaporator temperature a guess value is required to start the iteration without doing complicated simultaneous iterations. The mass flow guess value is estimated using equation 20.

$$\dot{m}_{guess} = \frac{Q_{load}}{h_1} \tag{20}$$

The temperature drop across the wick is related to the Clausius-Clapeyron relation (eqn. 21) [55]. Typically, a loop heat pipe operates at the steep part of the P-T curve so the

temperature difference across the wick is sufficiently small. Therefore, it is assumed that $T_7 \approx T_1$. The one-directional flow of the working fluid through the porous wick structure leads to a pressure drop that is obtained using Darcy's relation (eqn. 22) [34, 66].

$$T_1 - T_7 = \frac{\Delta P_{tot} - \Delta P_w}{\frac{\Delta P}{\Delta T} \mid_{sat}} \tag{21}$$

$$\Delta P_w = P_8 - P_7 = \frac{\mu_7 \dot{m} t_w}{K \rho_7 A_w} \tag{22}$$

As mentioned in section 2.1.1 there will be a small pressure drop inside the grooves. Adoni et al. suggest that this pressure drop is sufficiently small and therefore can be neglected [34]. As a result, the temperature and pressure at points 1 and 2 are supposed to be identical.

$$T_2 = T_1 \quad \Leftrightarrow \quad P_2 = P_1 \tag{23}$$

3.1.3 Transport lines and condenser

The steady-state numerical model by Siedel et al. assumes that the pressure drop inside the vapor line is sufficiently small that the evaporator outlet temperature is equal to the condenser temperature [35]. A more accurate approach is described by Adoni et al. based on the sixth-order Runga Kutta method [34, 65]. The fluid flow inside the vapor line, liquid line and subcooler is single phase. Heat exchange, pressure drop and mass of working fluid in these lines are calculated using equation 24, 25 and 26. Subscript t represents respectively the vapor line (vl), liquid line (ll) and subcooler (sc). Adoni et al. use an accurate approach to solve these differential equations based on the sixth-order Runga Kutta method [34, 65]. Thermophysical properties are calculated at the beginning of each length step and will be obtained at the saturation pressure if phase change occurs inside the tube. This procedure has high precision, especially for high thermal conductive tubes with a significant length, where thermal physical properties change within the tube [34].

$$\frac{dP_t}{dz} = -\zeta \frac{G^2}{2\rho_t D_{i,t}} \tag{24}$$

$$\frac{dT_t}{dz} = -\frac{U_t \pi D_{i,t} (T_t - T_{amb})}{\dot{m} C_{p,t}} \tag{25}$$

$$\frac{dM_t}{dz} = A_t \rho_t \tag{26}$$

The friction factor of single-phase flow in straight circular tubes depends on the amount of turbulence of the working fluid expressed in Reynolds number (eqn. 27). For laminar flow ($Re < 4000$) inside smooth tubes the friction factor is approximated using the Darcy-Weisbach relation given in equation 28, and for turbulent flow inside smooth tubes the Blasius correlation is used (eqn. 29) [67].

$$Re = \frac{4\dot{m}}{\pi D_i \mu} \tag{27}$$

$$Re < 4000 \quad \Rightarrow \quad \zeta = \frac{64}{Re} \tag{28}$$

$$Re \geq 4000 \quad \Rightarrow \quad \zeta = 0.3164 Re^{-0.25} \tag{29}$$

The global heat transfer coefficient U_t inside a circular tube is derived using equation 30. It depends on the heat resistance offered by the tube wall and individual convective heat transfer coefficients. The individual heat transfer coefficient for the outer area of the sub-cooler $h_{o,sc}$ and condenser $h_{o,cnd}$ is equal to the heat transfer coefficient of the sink h_{sink}. For the liquid and vapor line the outer heat transfer coefficient $h_{o,vl}$ and $h_{o,ll}$ is identical to the heat transfer coefficient of the ambient h_{amb} (≈ 5 W/m^2K). To determine the heat transfer coefficient of the single-phase flow inside the tube (vl, ll, sc), the Dittus-Boelter relation is utilized to estimate the dimensionless Nusselt number Nu.

$$U_t = \left[\frac{D_{o,t}}{2k_t} \ln(\frac{D_{o,t}}{D_{i,t}}) + \frac{D_{o,t}}{D_{i,t} h_{i,t}} + \frac{1}{h_{o,t}} \right]^{-1} \tag{30}$$

$$h_{i,t} = \frac{kNu}{D_{i,t}} \quad \Rightarrow \quad Nu = 0.023 Re^{0.8} Pr^{0.4} \tag{31}$$

The length of the two-phase region is determined by solving the differential equation for vapor quality using the sixth order RungeKutta method (eqn. 32) as described by Adoni et al. [34], where it is assumed that the working fluid temperature during phase-change is constant T_3 = T_4 = T_{cnd}. The total length of condensation is achieved if the vapor quality equals zero ($z = L_{cnd}$ when $x_{cnd} = 0$). The resulting condenser length (L_{sc}) is used to sub-cool the single-phase fluid in the condenser and therefore equations 24, 25 and 26 are used. The global heat transfer coefficient U_{cnd} is estimated with equation 30, where the convective heat transfer coefficient of two-phase flow is obtained by equation 35 as described by Hajal et al. [68]. This approach includes a liquid film thickness δ for annular flow during condensation and a homogeneous void fraction α_v. Subscript l and v represent the

saturated liquid and vapor properties.

$$\frac{dx_{cnd}}{dz} = -\frac{U_{cnd}(T_{cnd} - T_{sink})\pi D_{cnd,i}}{\dot{m}h_4} \tag{32}$$

$$L_{sc} = L_{cond} - L_{cnd} \tag{33}$$

$$h_{cnd} = 0.4{Re_l}^{0.5}Pr^{0.5}\frac{k_l}{\delta} \quad \Rightarrow \quad Re_l = \frac{GD_{i,cnd}(1 - x_{cnd})}{\mu_l} \tag{34}$$

$$\delta = \frac{D_i(1 - \alpha_v)}{4} \quad \Rightarrow \quad \alpha_v = \Big[1 + \left(\frac{1 - x_{cnd}}{x_{cnd}}\right)\left(\frac{\rho_v}{\rho_l}\right)\Big]^{-1} \tag{35}$$

Typically, frictional pressure drop in two-phase flow is predicted using a separated flow model. Single-phase flow in liquid and vapor phases are treated separately and related to each other in a two-phase multiplier ${\phi_l}^2$. Literature observes that numerous frictional multiplier correlations have been developed over the years [69]. Adoni et al. use the standard two-phase multiplier correlation by Friedel, however, Chen et al. observe that for small tubes (<7 mm) in combination with water as the working fluid the Friedel correlation could not predict empirical data with acceptable accuracy [70, 71]. They modified the existing correlation by implementing a dimensionless Bond number Bo.

$$\frac{dP_{cnd}}{dz} = -\phi^2\zeta_l\frac{G^2}{2\rho_l D_{i,cnd}} \tag{36}$$

$$\phi^2 = \frac{0.0333Re_l^{0.45}}{{Re_v}^{0.09}(1 + 0.4e^{-Bo})} \quad \Rightarrow \quad Re_v = \frac{GD_{i,cnd}x_{cnd}}{\mu_v} \tag{37}$$

$$Bo = \frac{g(\rho_v\rho_l)\frac{D_{i,cnd}}{2}^2}{\sigma} \tag{38}$$

Equation 39 gives the mass of the working fluid inside the condenser. Vapor quality, pressure drop and mass of working fluid are simultaneously solved using the Runga-Kutta method, where the thermophysical properties are calculated at the beginning of each length step.

$$\frac{dM_{cnd}}{dz} = A_{cnd}[\alpha_v\rho_v + (1 - \alpha_v)\rho_l] \tag{39}$$

The mass of the working fluid within the evaporator is determined using equation 40, where β is the applied volume fraction of the fluid inside the compensation chamber and ϵ the porosity of the wick structure. The values for $\rho_{7,l}$ and $\rho_{7,g}$ are related to the density of the saturated liquid and vapor inside the compensation chamber. The total mass inside the loop is estimated using equation 41

$$M_{evap} = M_{cc} + M_w + M_v = \rho_{7,l} A_w H_{cc} \beta + \rho_{7,g} A_w H_{cc} (1 - \beta) + A_w \epsilon \rho_{7,l} + A_v \rho_1 \tag{40}$$

$$M_{tot} = M_{evap} + M_{vl} + M_{cnd} + M_{sc} + M_{ll} \tag{41}$$

The analytical model of Adoni et al. considered that the working fluid inside the compensation chamber is saturated [34]. Since the pressure at the end of the liquid line P_6 is equal to the pressure inside the compensation chamber P_7, it is supposed that the temperature inside the compensation chamber is identical to the saturation temperature at P_6 (eqn. 43).

$$P_7 = P_6 \tag{42}$$

$$T_7 = T_{sat}(P_7) \quad \rightarrow T_7 = T_{sat}(P_6) \tag{43}$$

Overall, the improved numerical model includes mathematical equations that describe the heat transfer process inside the evaporator, the transport lines and the condenser section with high precision. By separately describing the heat transfer process in the evaporator and the transport lines, the model enables the possibility of implementing extra equations in later research that describe the pressure drop induced by bends or vapor grooves. This is an additional benefit compared to the numerical model of Siedel, since the authors neglect the pressure drop inside the transport lines.

3.2 Numerical scheme

This section aims to provide an algorithm where the steady-state balance of a loop heat pipe is achieved using the equations given in the previous chapter. The main goal of this steady-state balance is to predict stable pressure and stable temperature at different locations inside the loop for a certain geometry.

A frequently used method to create a steady-state condition of the loop heat pipe is to minimize the energy imbalance inside the compensation chamber given in equation 45. This equation is evaluated for different saturated vapor temperatures (T_1) till the temperature converges and the energy imbalance is below a fixed error ε.

$$\vartheta_{cc} = Q_{cc} + Q_w - \dot{m} x_6 h_6 - \dot{m} C_{p,7}(T_7 - T_6) \tag{44}$$

$$\vartheta_{cc} \leq \varepsilon \tag{45}$$

The iteration starts by predicting a guess value for saturated vapor temperature T_1 and saturated liquid T_7. The selection of both values has an influence on the amount of iterations to achieve convergence. To reduce the number of guess values and to simplify the scheme, the temperature difference between the saturated vapor and liquid ΔT is fixed for each iteration to a certain number. As mentioned in the Clausius-Claypeyron relation (eqn. 21), the temperature difference across the wick (ΔT) is sufficiently small and so a value of 0.5 K is chosen. Figure 11 showed that a ΔT between 0.5 K and 2 K has barely any influence on the steady-state output temperatures. For a guess value difference above 2 K a deviation was observed in the low heat flux range. In general, the operation temperature of the working fluid is lower for smaller heat loads which results in a larger effect of the prescribed temperature difference of the wick.

$$T_{7,guess} = T_{1,guess} - \Delta T = T_{1,guess} - 0.5 \tag{46}$$

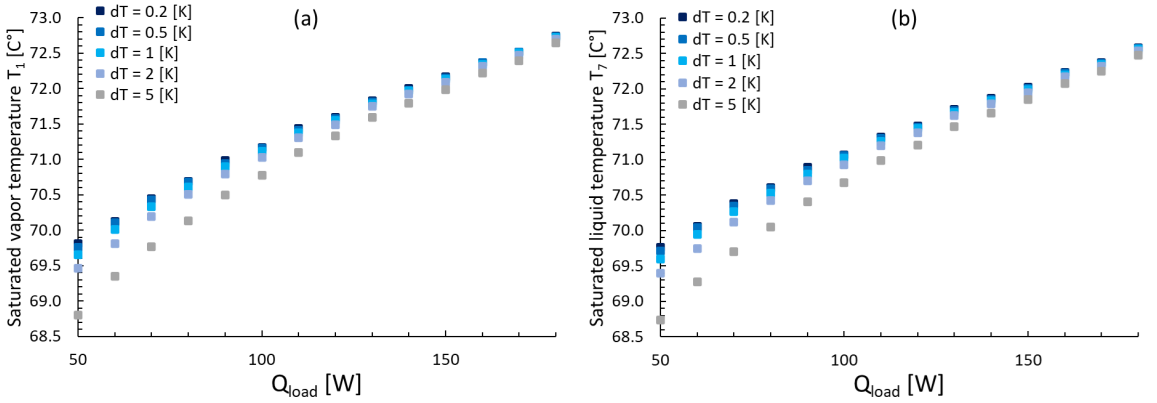

Figure 11: Numerical results. (a) Influence of the guess temperature difference on the saturated vapor temperature. (b) Influence of the guess temperature difference on the saturated liquid temperature.

Following the numerical procedure as shown in figure 13, gives all temperatures and pressures at specified locations in the loop heat pipe. The complexity of the Fourier-based formulas makes it not suitable to use the Newton-Rapshon Method to solve the energy imbalance as described by Adoni et al. [34]. When the energy imbalance is larger than the prescribed error (eqn. 45) a new value for saturated vapor is obtained using the Secant Method (eqn. 47) [65]. This root finding approach requires 2 values T_1^{i-1} and T_1^i to determine the energy imbalance as a function of these values ϑ_{cc}^{i-1} and ϑ_{cc}^i. The slope of the constructed (secant) line between those 2 points is used to approximate a new value for T_1^{i+1} where the function for energy imbalance is equal to zero. To start the secant method two initial values (T_1^0 and T_1^1) are required, with the rule that both values are not identical. As illustrated in the algorithm scheme, T_1^0 is equal to the guess temperature and T_1^1 is arbitrarily chosen to be slightly (0.1K) higher than T_1^0.

$$T_1^{i+1} = T_1^i + \frac{(T_1^i - T_1^{i-1})\vartheta_{cc}^i}{\vartheta_{cc}^i - \vartheta_{cc}^{i-1}} \tag{47}$$

As mentioned in Appendix B, the coefficients are obtained by infinite series. This serial convergence is achieved for a summation difference below $1{\times}10^{-7}$. For the coefficients B_1, B_2 and B_3 it was observed that a limited number series ($\infty \rightarrow 100$) results in reasonable solutions. The Runga Kutta method, which is applied to approximate heat transfer and pressure drop in the transport line and condenser section, is divided into increments of 5 mm in the vapor line, liquid line and subcooler and 1 mm in the condenser. Further, the Newton-Raphson method to obtain the evaporator temperature is selected to converge

if the initial value and output value during the iteration are lower than 0.01K. The thermophysical properties of the working fluids are obtained using REFPROP:10.0. As illustrated in figure 12 (a), the numerical error has an influence on the predicted saturated vapor temperature for a fixed error above 0.001%. It was also observed that the saturated liquid temperature is independent of the prescribed numerical accuracy (fig. 12 (b)). This tendency is related to the assumption that the temperature in the compensation chamber is equal to the saturation pressure at the end of the liquid line (43). Since a higher saturated vapor temperature T_1 (which is the case for an error above 0.001%), will not have a significant effect on the pressure difference inside the loop, the saturated liquid temperature will be approximately identical for each numerical error.

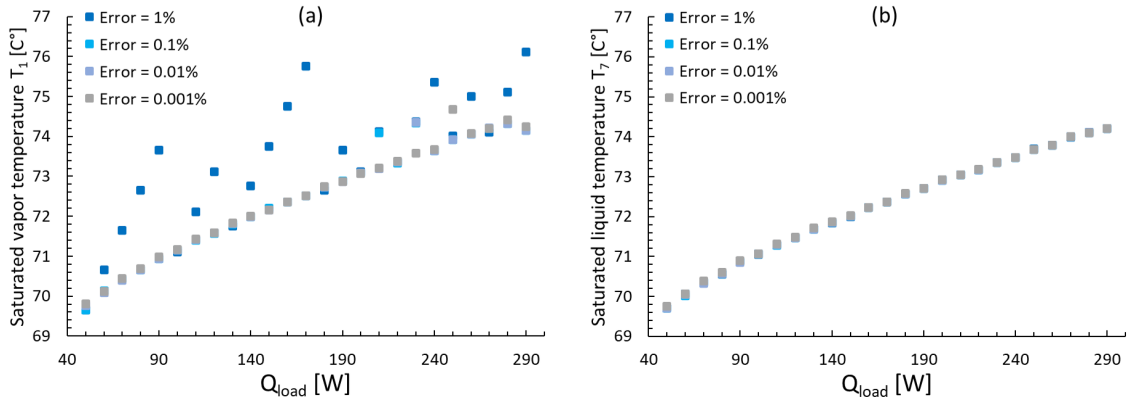

Figure 12: Numerical results. (a) Influence of the numerical error on the saturated vapor temperature. (b) Influence of the numerical error on the saturated liquid temperature

The section reveals an algorithm that has the ability to predict steady-state values of temperatures inside the system using the precise mathematical formulas given in section 3.1. Further, it is observed that the numerical output reached a steady-state condition for a numerical error less or equal to 0.001 %.

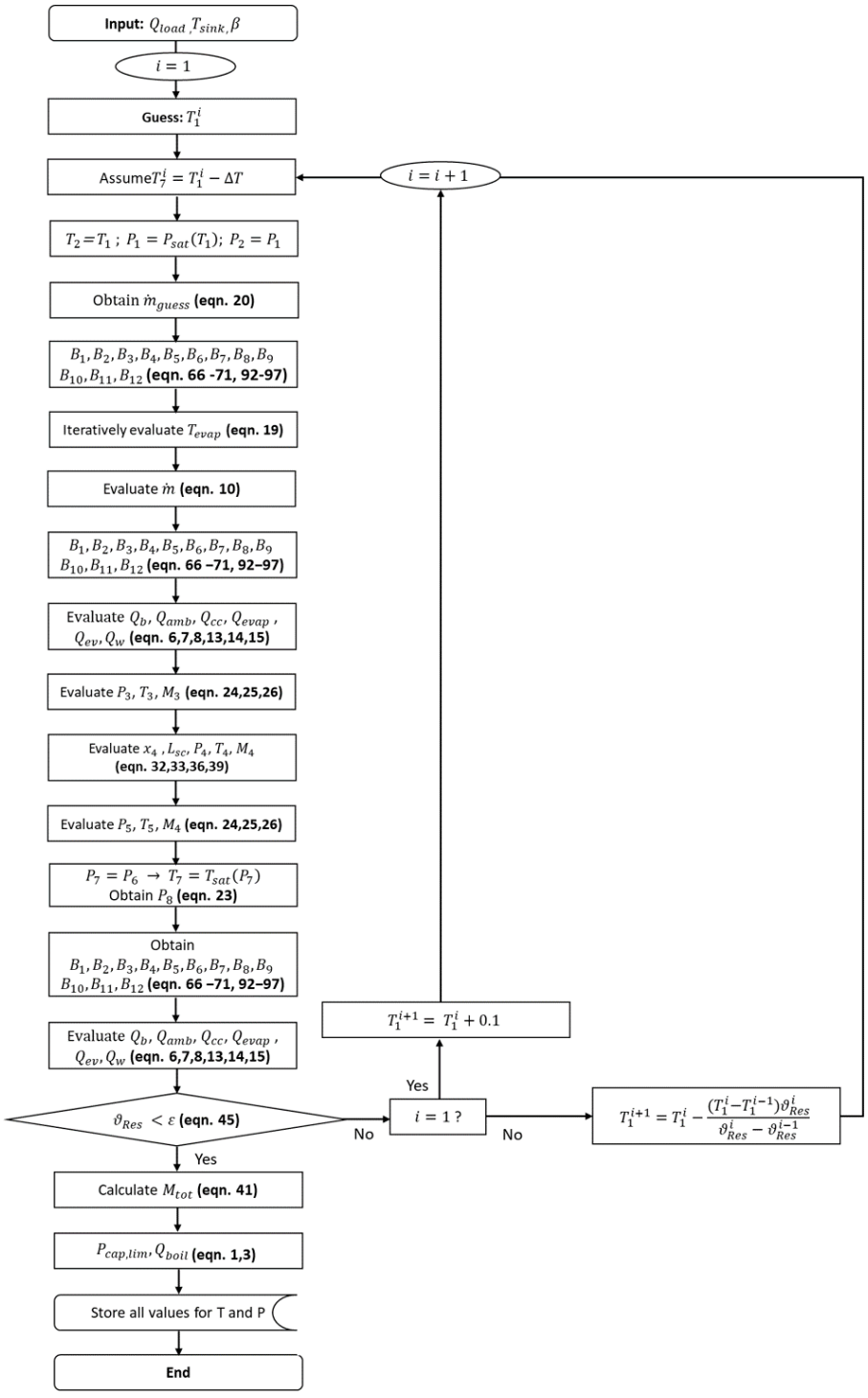

Figure 13: Algorithm scheme of the improved numerical model

3.3 Experimental validation

The improved numerical model is based on mathematical equations and assumptions that govern the heat transfer phenomena occurring within the LHP. Nevertheless, it is essential to experimentally validate this model to ensure it can accurately predict the performance and behavior of actual loop heat pipes. In this research 2 experimental investigations were used to verify if the developed model simulates reliable results.

The comparison between numerical and experimental data is conducted by analyzing key performance metrics such as temperature distribution and thermal resistance. The latter is distinguished in the thermal resistance of the evaporator (eqn. 48) and the thermal resistance of the entire loop heat pipe (eqn. 49). The first equation includes the temperature difference between the evaporator temperature at the fins T_{evap} and the saturated vapor temperature T_1 inside the grooves and the applied heat load. The thermal resistance of the entire LHP is obtained by the temperature difference between evaporator temperature T_{evap} and the average temperature of the working fluid inside the condenser $\frac{T_5-T_3}{2}$.

$$R_{evap} = \frac{T_{evap} - T_1}{Q_{load}} \tag{48}$$

$$R_{LHP} = \frac{T_{evap} - \frac{(T_5-T_3)}{2}}{Q_{load}} \tag{49}$$

The first validation is conducted using experimental data obtained by Singh et al. [72]. They developed a miniature loop heat pipe with a flat disk-shaped evaporator using a Nickel wick structure and water as a working fluid. The experiments were executed in a heat load range from 5 W to 70 W with an active heat transfer area of 7.069 cm^2, the authors observe unstable temperature distributions at a low heat load range (< 20 W) and therefore the numerical validation is only executed above this value. As shown in Table 1, a fin-and-tube type heat exchanger was utilized to condense the working fluid by a fan with a sink temperature identical to the ambient temperature (22 °C). The effective thermal conductivity for the homogeneous wick structure is estimated by the Alexander correlation (eqn. 50) as described by Sing et al. in later research, where k_w is the conductivity of solid Nickel ($\approx$ 90 W/mK), ϵ the porosity of the wick (0.75) and k_l the thermal conductivity of the working fluid depending operation temperature [73].

$$k_{we} = k_l \left(\frac{k_l}{k_w} \right)^{-(1-\epsilon)^{0.59}} \tag{50}$$

Inside the evaporator, an O-ring was placed to prevent heat leak through the wall ($k_c \approx 1$ W/mK). The authors did not describe key parameters as the heat transfer coefficient of the sink, the evaporation coefficient, the contact resistance of the wick and the heat transfer coefficient of fluid inside the compensation chamber. Nevertheless, the same experimental setup was validated by the numerical model of Siedel et al. and so some of these unknown parameters were identified in their research [35]. Siedel et al. conclude that the evaporation coefficient is identical to 0.4 and the contact resistance is fixed to 1×10^{-5} Km^2/W. The heat transfer coefficient of the fluid inside the reservoir h_{cc} was not given in the research paper, however, after correspondence with the authors it was set to 1000 W/m^{2}K. The heat transfer coefficient of the sink is selected to be 4.5 kW/m^{2}K, which is slightly higher than the prescribed value of Siedel et al. (3.2 kW/m^{2}K) since their model does not include the thermal resistance of the condenser wall.

The second validation is based on experimental research by Zhoa et al. [74]. The authors investigate the performance of flat disk evaporator with a capillary biporous T255 Nickel wick together with deionized water as the working fluid (Table 1). The LHP was tested in a heat load range from 50 W to 290 W with an active area of 10.18 cm^2. A sink temperature of 10 °C was used to cool the working fluid within a tube-in-tube heat exchanger. The authors did not describe the material of the evaporator casing, however, their earlier research on loop heat pipes utilized a stainless steel body and so $k_c \approx 18$ W/mK [75]. The same research was used to identify the effective thermal conductivity of the biporous Nickel wick $k_{we} \approx 3.265$ W/mK. Note that the porosity in this earlier research (0.742) is slightly higher than the porosity in the investigated study (0.71). A biporous wick is characterized by large pores that reduce the flow resistance and small pores to maintain the capillary forces. The capillary performance was estimated by the given static contact angle (88.75 °) and the mean radius of the small pores (5 µm). An evaporation coefficient of 0.1 was chosen, identical to the value Siedel et al. use in their 'standard case' simulation [35] for a standard case. The heat transfer coefficient of the fluid inside the compensation chamber and the thermal resistance between wick and fins were specified to the same value used in the first validation, respectively, 1000 W/m^2K and 1×10^{-5} Km^2/K. Furthermore, the heat sink heat transfer coefficient is set to 6 kW/m^{2}K, which is in the range between values from Siedel et al. (2 kW/m^2) and from Gabsi et al. (12 kW/m^2) [35, 76].

	Experimental setup		**Experimental setup**
Casing		Liquid line	
Material	SLM Stainless steel (316)	$D_{i,ll}$ / $D_{o,ll}$	4 / 6 [mm]
H_b	2 [mm]	L_{ll}	875.5 [mm]
H_{top}	0 [mm]	k_{ll}	398 [W/mK]
H_c	23 [mm]	Vapor line	
t_c	2 [mm]	$D_{i,vl}$ / $D_{o,vl}$	4 / 6 [mm]
k_c	18 [W/mK]	L_{vl}	330 [mm]
Grooves		k_{vl}	398 [W/mK]
α_{ev}	0.1 [-]	Condenser	
H_{vg} / W_{vg}	2 / 0.5 [mm]	Type of heat exchanger	Tube-in-Tube
W_f / L_f	1 / 37 [mm]	$D_{i,cond}$ / $D_{o,cond}$	4 / 6 [mm]
N_f	28 [-]	L_{cond}	500 [mm]
A_f	9.990 [cm^2]	k_{cond}	398 [W/mK]
Wick		h_{sink}	2000 [W/m^2K]
Material	SLM Octahedredal steel (316)	T_{sink}	20 [°C]
t_w	2.5 [mm]	General specifications	
A_w	15.17 [cm^2]	Working fluid	Distilled water
R_{wf}	0 [Km^2/W]	r_{nuc}	0.254 [µm]
k_{we}	6 [W/mK]	$\boldsymbol{\theta}$	56.8 [°]
ε	0.46 [-]	$\bar{\mathbf{M}}$	0.01805 [kg/mol]
K	$1.305x10^{-10}$ [m^2]	h_{amb}	5 [W/m^2K]
r_{wp}	108 [µm]	T_{amb}	22 [°C]
Compensation chamber			
h_{cc}	1000 [W/m^2K]		

Table 1: Experimental setup specifications by Singh et al. and Zhao et al. [73, 74]

As illustrated in figure 14, the numerically predicted values are in good agreement with the experimentally obtained data from both studies [72, 74]. It is observed that the numerical obtained values for average condenser temperature are 1.2% to 12.4% higher compared to the experimental data by Singh et al. (fig. 14 (a)) [72]. This could be related to the type of heat exchanger that is used - a fin-in-tube instead of a tube-in-tube - which differs from the numerical model. The deviation in condenser temperature also initiates a difference in thermal resistance of the loop heat pipe (fig. 14 (b)) as concluded from equation 49. Despite this, the predicted temperature distribution has the same tendency as experimental data and the evaporator casing and outlet temperature do not show a significant difference. Figure 14 (a) also shows a comparison between the numerically obtained data from Siedel et al. and the new improved model using the data from Singh et al. [35, 72]. It is noticed that both models do not predict a distinctive difference. However, it is relevant to mark that the main improvement of the new model is the estimation of heat transfer in the transport lines and the condenser which is not substantial in the developed miniature loop heat pipe of Singh et al. [72].

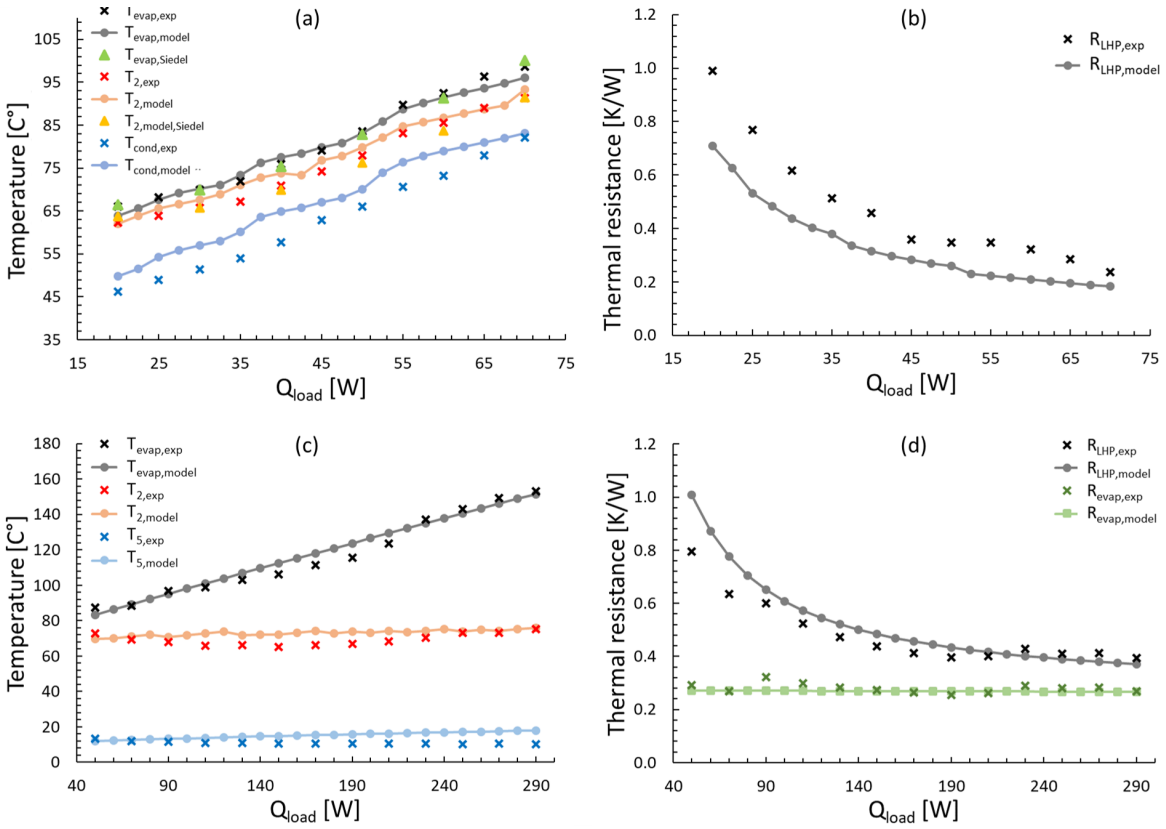

Figure 14: (a) Predicted temperatures by the new improved model and the numerical model of Siedel et al. vs experimental data by Singh et al. [35, 72]. (b) Predicted loop heat pipe thermal resistance vs experimental data by Singh et al. [72]. (c) Predicted temperatures vs experimental data by Zhoa et al. [74]. (d) Predicted evaporator and loop heat pipe and thermal resistance vs experimental data by Zhoa et al. [74].

Moreover, figure 14 (b,c) presents that the numerical model predicts equivalent results as the experimental data from Zhoa et al. [74]. However, it is remarkable that at 50 W the experimental obtained loop heat pipe thermal resistance is 21.1 % lower than estimated and the actual condenser outlet temperature is 11.4% higher than predicted. Zhoa et al. observe a temperature fluctuation for heat loads below 90 W and relate this effect to unstable pressure development in low heat range [74]. For higher heat loads the experimentally obtained outlet temperature becomes identical to the sink temperature (10 °C). In contrast, the predicted condenser exit temperature increases to 17.9 °C at 290 W. This deviation can be associated with the geometry of the condenser. According to a schematic diagram of the developed LHP, the condenser section contains 2 bends, which could create a more

turbulent flow and a higher heat transfer coefficient of the working fluid compared to the working fluid within the straight-modeled heat exchanger. At 290 W the improved numerical model predicts a heat transfer coefficient of 220 W/m^{2}K for the working fluid inside the subcooler h_{sc}. By completing equation 30 with the condenser diameters, the thermal conductivity of the copper wall (k_{sc} = 400 W/mK) and the heat transfer coefficient of the sink (h_{sink} = 6000 W/m^{2}K), it can be observed that the internal heat transfer coefficient is the dominant parameter.

Overall, the improved numerical model shows a reasonable predicting power compared to 2 discussed experiments investigations in the literature. It was noticed that the deviation of the condenser temperature in both cases is related to the condenser type and shape. For practical applications, for example in data center servers, it is suggested to implement a new equation to the numerical model that describes the heat transfer occurring in a fin-tube heat exchanger.

3.4 Parametric study

In addition to the experimental validation, the improved numerical model is subjected to a parametric study. The influence of several fundamental LHP specifications is tested to see if the output agrees with hypothetical predictions. The study was executed with the same geometry and specifications as the experimental validation for the LHP developed by Zhao et al. given in Table 1 [74].

The numerical model is first investigated on 4 'unknown' parameters. As expected from equation 78, a higher evaporation coefficient induces an increasing heat transfer coefficient of evaporation (fig. 15). This will lead to less heat leak (eqn. 15) and a lower evaporator temperature (fig. 15 (a)). It is observed that the evaporation coefficient of 0.01 results in significantly higher temperature distribution, however as mentioned before, for a dynamically renewed water surface the coefficient will be larger than 0.1. Further, figure 15 (b) shows that a high contact resistance results in an increase in evaporator temperature which is plausible, since a thermal gap between wick and fins leads to a lower heat transfer rate at the meniscus of the wick. The third figure outlined that the heat transfer coefficient of the sink influences the LHP performance at higher evaporator temperatures. As there is less heat transfer in the condenser the amount of subcooling decreases and so the operation temperature increases. The last graph illustrated that the heat transfer of the working

fluid inside the compensation chamber plays a significant role in the performance - especially at low heat loads. However, it must be noted that the actual value of this parameter partly depends on the mass flow rate which is lower for a smaller heat load (eqn. 10).

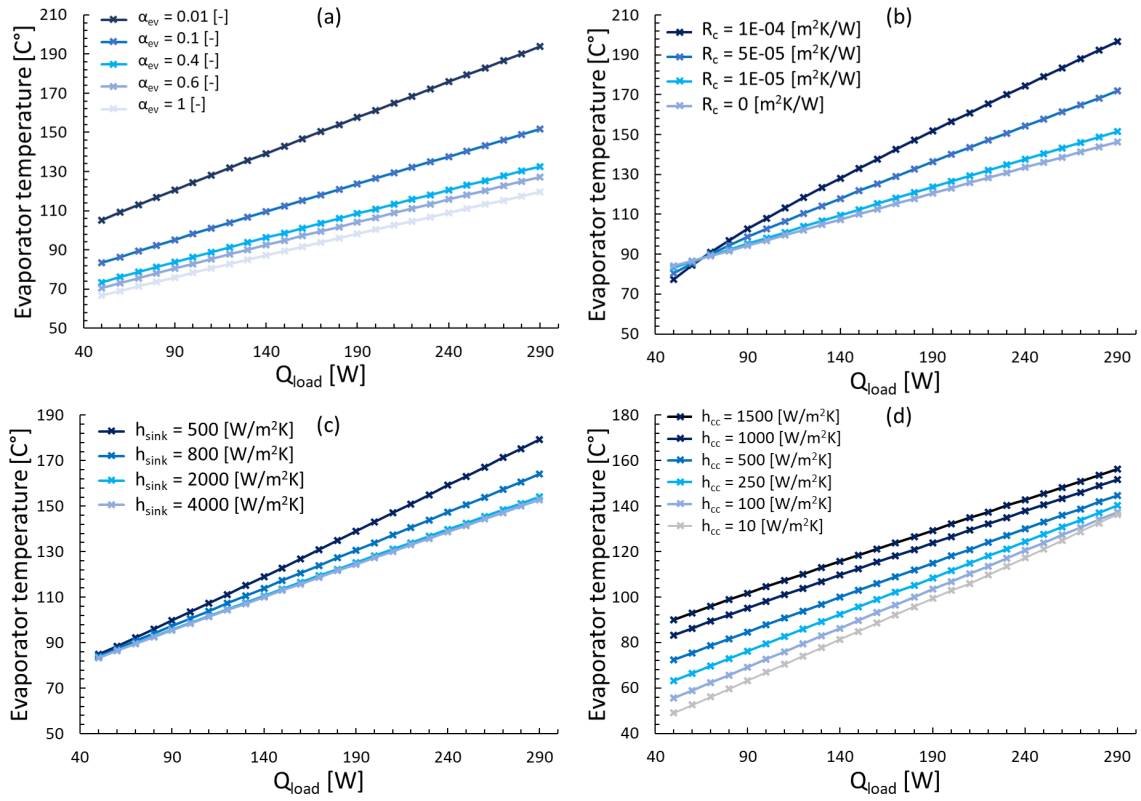

Figure 15: Parametric study. (a) Influence evaporation coefficient on T_{evap}. (b) Influence contact resistance on T_{evap}. (c) Influence heat transfer coefficient of the sink on T_{evap}. (d) Influence heat transfer coefficient of fluid inside compensation chamber on T_{evap}.

Next to the prescribed specification, the effect of 4 geometry-dependent parameters is verified. These values are important for the design optimizations that can be approached by additive manufacturing. The first graph of figure 16 observes that the effective thermal conductivity of the wick strongly influences the LHP performance. A higher effective thermal conductivity accounts for better heat transfer and evaporation of the saturated vapor at the meniscus of the wick. In addition, a larger wick thickness leads to a performance enhancement, since the heat leak through the wick is reduced. As expected, the thermal conductivity of the casing should be minimized to avoid heat leakage through the wall

and decrease the evaporator temperature (fig. 16 (c)). Finally, the thickness of the casing is increased which results in a higher leakage from the casing to the compensation chamber. To compensate for this heat leak, the evaporator temperature should expand as illustrated in figure 16 (d).

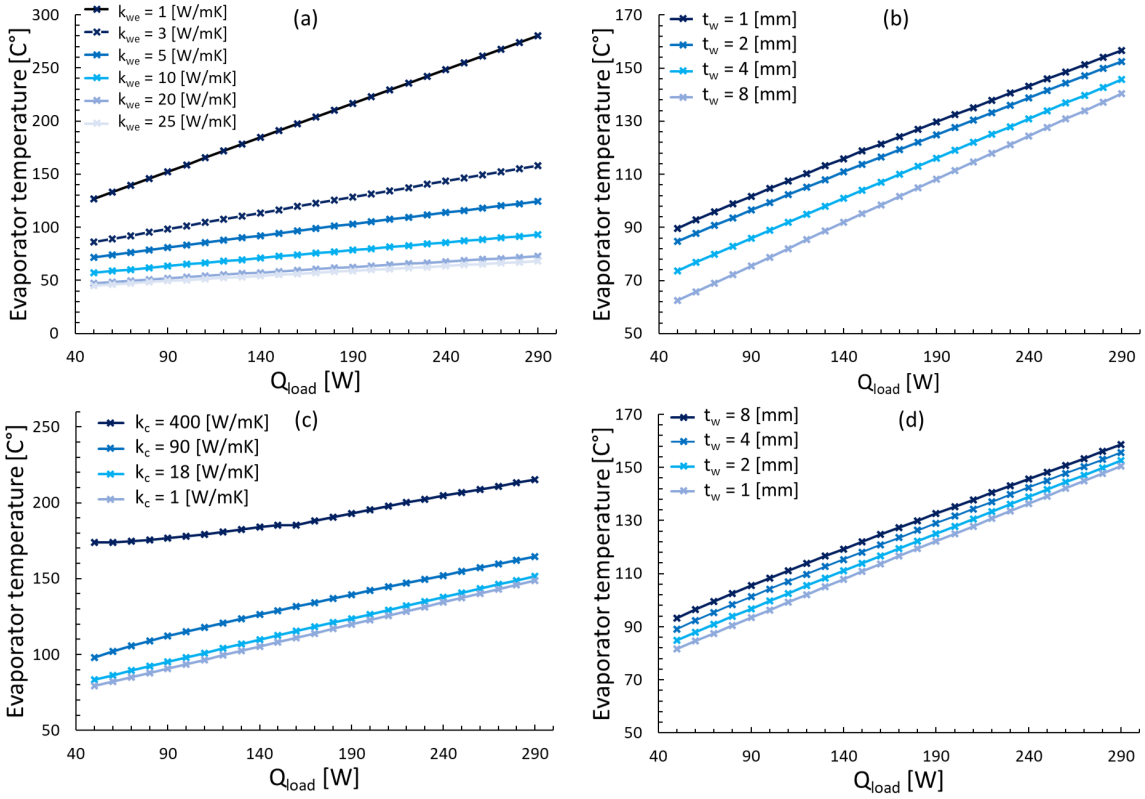

Figure 16: Parametric study. (a) Influence effective thermal conductivity of wick on T_{evap}. (b) Influence wick thickness on T_{evap}. (c) Influence thermal conductivity of evaporator body on T_{evap}. (d) Influence evaporator body thickness on T_{evap}.

The parametric study in this section predicts the influence of several input parameters on the operation temperature in good agreement with the hypothetical expectations. Furthermore, the relevance was observed to obtain more information in later research about the heat transfer coefficient of the sink, the heat transfer coefficient of the working fluid inside the compensation chamber and the evaporation coefficient.

3.5 Numerical evaluation and discussion of 3D printed loop heat pipes

In summary of the last 2 sections, the experimental validation and the parametric study both observe that the improved numerical model has the ability to generate predictable and reliable solutions. From figure 16 it is also shown that parameters such as the effective thermal conductivity of the wick, thermal conductivity of the body, casing thickness and wick thickness have a notable influence on the performance. The most distinctive advantage of additive manufacturing is that all of these parameters can be changed and so optimized to get a more high-performance loop heat pipe. This section aims to provide an enhanced loop heat pipe efficiency by varying the evaporator geometry using the improved numerical model. Further, the discussed additive-manufactured structures in section 1.3 are investigated on capillary performance and heat transfer characteristics to find whether there is an ability to utilize additive-manufactured wicks in actual designs.

All numerical simulations were executed using the experimental setup specifications by Zhoa et al. given in Table 1 [74]. The authors fabricated a 2.2 mm thick biporous sintered Nickel wick structure within a 1.5 mm stainless steel casing. By varying the effective thermal conductivity of the wick and the thermal conductivity of the casing it was observed that the first value has the biggest influence on the overall performance (fig. 17). Figure 17 also shows that the best enhancement is reached using a high-conductive wick material and a low-conductive casing material.

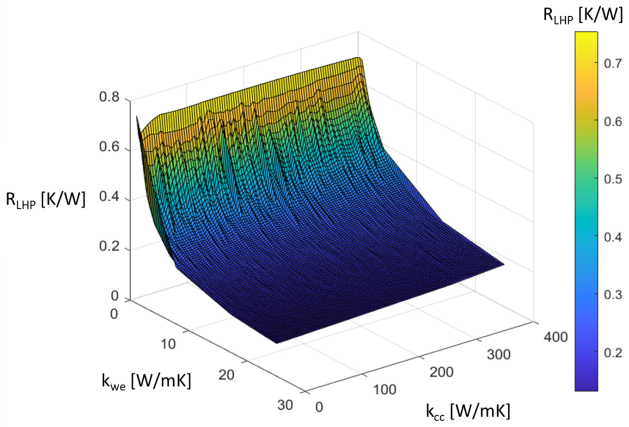

Figure 17: Numerically obtained thermal resistance of the loop heat pipe vs the thermal conductivity of the casing and the effective thermal of the wick by using the experimental setup by Zhao et al. [74].

The latest development concerning the metal printing technique aims to fabricate multi-materials. This provides the ability to print wick structures with a high thermal conductivity such as copper together with low conductive casing materials as steel. To the authors knowledge, there is no former research into the fabrication of high-conductive 3D printed wick materials such as copper. However, a recent literature review by Jiang et al. revealed that the development of copper additive manufactured structures is increasing rapidly [77]. An experimental study by Jafari et al. on effective thermal conductivity correlations showed that the effective thermal conductivity of an SLM porous media corresponds the best using the Upper Maxwell Correlation (eqn.51) [28]. The development of an additive manufactured copper wick structure (k_w = 398 W/mK) with the same porosity (ϵ = 0.59) as the developed octahedral structure by Jafari et al. results in an approximate effective thermal conductivity of 176.6 W/mK. As mentioned in section 3.4, printing the grooves and wick as one structure disables the contact resistance and leads to a more efficient system. By printing the identical evaporator developed by Zhoa et al. as one entire structure (R_{wf} = 0 Km^2/K), using a copper wick (k_{we} = 176.6 W/mK) and stainless steel as casing material (k_c = 18 W/mK), the heat pipe performance significantly improved (fig. 18). At 290 W, the overall and evaporator thermal resistance of Sample I in Table 4 is approximately 0.064 K/W and 0.046 K/W which is 82.7 $\%$ higher than the developed structure of Zhoa et al. (0.371 K/W and 0.264 K/W) [74].

$$k_{we} = \frac{k_7 \left[2\left(\frac{k_w}{k_7}\right)^2 (1-\epsilon) + (1+2\epsilon)\left(\frac{k_w}{k_7}\right) \right]}{(2+\epsilon) + \frac{k_w}{k_7} + 1 - \epsilon} \tag{51}$$

Furthermore, the described additive-manufactured copper/steel evaporator can be improved by changing the casing and wick size. As obtained in the parametric study, the performance enhancement is achieved using a smaller casing thickness and an increased wick thickness. The first one is limited by the gas tightness of additive manufactured structure, which is important to avoid pressure leakage. Abelea et al. conducted gas tightness research on thin-walled selective laser melting stainless steel structures, where pressure leakage was detected for structures smaller than 200 µm [78]. Note that the outcome of this experiment depends on the printing settings and powder materials, and therefore a minimum wall thickness of 500 µm is chosen. The selection of the wick thickness depends on the required capillary performance of the additive-manufactured copper wick, which is unknown since several parameters as permeability and contact angle are not given. To

give an indication about the performance enhancement of additive manufactured copper wick structures, the wick thickness is varied with 4 mm, 6 mm, 8 mm which is in the same range as actual heat pipes. As shown in Table 4 and figure 17, the influence of the wick thickness and casing thickness is marginal compared to the performance of Sample I. Sample IV has the smallest overall thermal resistance (0.063 K/W) which is 82.9 % lower than the constructed evaporator by Zhoa et al. [74].

	Zhoa et al. [74]	**Sample I**	**Sample II**	**Sample III**	**Sample IV**
Casing					
Material	Steel (304)	SLM Steel (304)	SLM Steel (304)	SLM Steel (304)	SLM Steel (304)
t_c	1.5 [mm]	1.5 [mm]	0.5 [mm]	0.5 [mm]	0.5 [mm]
$\mathbf{k_c}$	18 [W/mK]	18 [W/mK]	18 [W/mK]	18 [W/mK]	18 [W/mK]
Wick					
Material	Biporous Nickel	SLM copper	SLM copper	SLM copper	SLM copper
t_w	2.2 [mm]	2.2 [mm]	4 [mm]	6 [mm]	8 [mm]
k_{we}	3.265 [W/mK]	176.6 [W/mK]	176.6 [W/mK]	176.6 [W/mK]	176.6 [W/mK]
$\mathbf{R_{wf}}$	$1x10^{-5}$ [Km^2/W]	0 [Km^2/W]	0 [Km^2/W]	0 [Km^2/W]	0 [Km^2/W]
Numerical output (290 W)					
$\mathbf{R_{LHP}}$	0.371 [K/W]	0.064 [K/W]	0.0635 [K/W]	0.06347 [K/W]	0.06341 [K/W]

Table 2: Specifications for the Nickel biporous wick by Zhoa et al. compared to the suggested multi-material additive manufactured samples. [74]

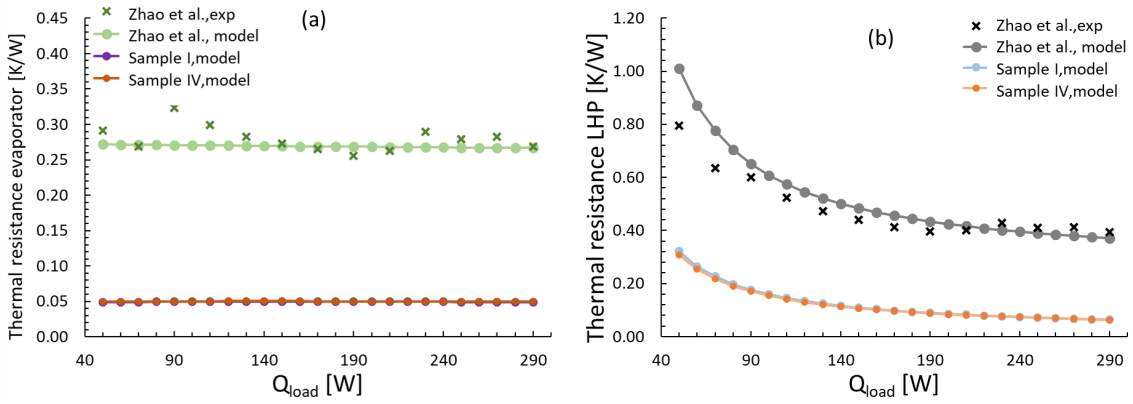

Figure 18: (a) Evaporator thermal resistance. (b) Loop heat pipe thermal resistance.

The numerical model shows the relevance of developing a wick structure with a high capillary performance (to increase the wick thickness) and low porosity (to increase the effective thermal conductivity). The wide design freedom of additive manufacturing combined with the latest development of 3D-printing techniques (multi-materials, new high

conductive materials, more advanced and precise structures) and the rapid development of artificial intelligence-driven design optimization tools could help to develop an excellent wick structure in future research [77, 79, 80]. The specifications of this improved wick structure can be used as input values in the new improved model to predict the loop heat pipe performance.

Despite the performance enhancement of the suggested copper/steel evaporator, the development of additive-manufactured multi-material structures is in its early stages. As a result, it is relevant to investigate the heat transfer characteristics and capillary performance of existing 3D-printed wick structures discussed in section 1.3. The specifications of these wick structures are outlined in Table 3. Hu et al. did not describe the static contact angle between the working fluid and water and therefore the value is set to 90 ° which is identical to the obtained contact angle by Esarte et al. [26, 27]. The incompatibility of water and aluminum means that the study of Robinson et al. did not investigate the static contact angle for water as a working fluid [25]. To give an indication of the capillary performance the static contact angle was supposed to be 83 ° [81].

	Esarte et al. [26]	**Hu et al. [27]**	**Jafari et al. [24]**	**Robinson et al. [25]**	**Zhoa et al. [74]**
Wick					
Material	SLM printed 316l	SLM printed 316l	SLM printed 316l	DMLS printed aluminium	Biporous T255 Nickel
k_{we}	1.48 [W/mK]	5.87 [W/mK]	6 [W/mK]	8.30 [W/mK]	3.265 [W/mK]
ε	0.17 [-]	0.509 [-]	0.46 [-]	0.59 [-]	0.71 [-]
K	1.25×10^{-12} [m^2]	2.13×10^{-10} [m^2]	1.305×10^{-10} [m^2]	4×10^{-11} [m^2]	1.14×10^{-12} [m^2]
r_{wp}	80 [µm]	109 [µm]	108 [µm]	88 [µm]	5 [µm]
$\boldsymbol{\theta}$	90 [°]	90 [°]	56.8 [°]	83 [°]	88.75 [°]

Table 3: Specifications of the additive manufactured wick structure [24–27, 74]

All numerical simulations were executed with the same experimental setup specifications (using the same wick thickness, wick geometry, casing thickness e.g.) given by Zhoa et al. (Table 1) [74]. The numerical results given in figure 19 (a), present that several existing 3D-printed structures generate lower operation temperatures. This performance enhancement is related to the larger effective thermal conductivity of the wick caused by the relatively low porosity of the additive-manufactured wick structures. Nevertheless, as shown in figure 19, most 3D-printed wick structures fail to maintain the capillary limit due to their large pore size and high contact angle. The 3D-printed wick that satisfies the capillary condition is the octahedral structure developed by Jafari et al. [24]. Despite the relatively low permeability and high pore size of the wick - which causes less pressure drop inside

the wick - the overall pressure drop of the system is higher than using a wick of Zhoa et al. [74]. This effect is associated with the high-pressure drop of laminar flow within a vapor line. The lower temperatures inside the system create a laminar flow with a higher friction factor (eqn. 28). Finally, it was predicted that the octahedral structure has a lower overall thermal resistance (29 %) and a lower evaporator thermal resistance (32 %) compared to the developed wick biporous Nickel wick. When the fins and wick are printed as one entire structure, the contact resistance disappears and the loop heat pipe thermal resistance declines 34 % (0.372 K/W $\rightarrow$ 0.245 K/W) and the evaporator thermal resistance decreases 39 % (0.267 K/W $\rightarrow$ 0.163 K/W).

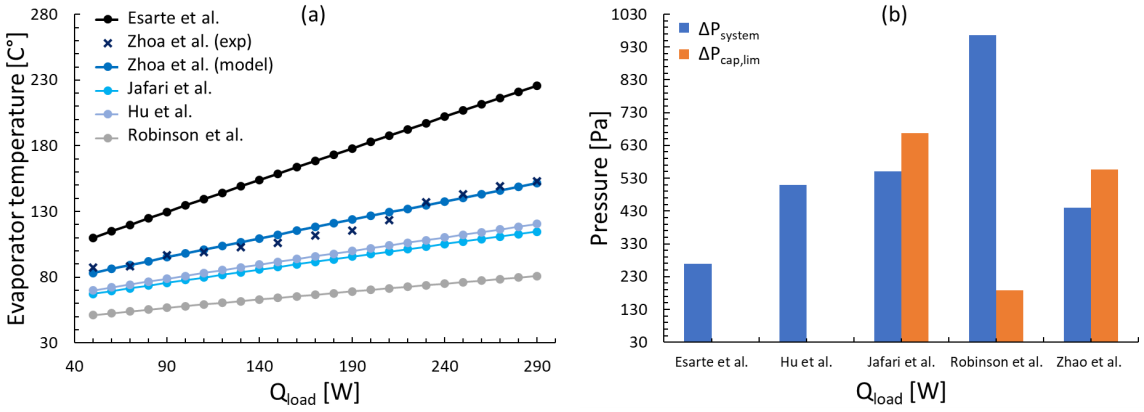

Figure 19: (a) Temperature distribution inside the system for several additive manufactured wick structures (b) Capillary limitations and total pressure drop of existing additive manufactured wick structures.

In brief, the numerical results predict an imposing enhancement for additive-manufactured evaporators including a 0.5 mm thick stainless steel casing, a copper wick/groove structure, and an 8 mm thick wick. The development of these multi-material copper/steel structures is in an early stage and requires more information about key parameters such as capillary performance and porosity of the wick structure. However, it could be an important breakthrough in loop heat pipe development. Even, the applications of existing low conductive stainless steel additive manufactured structures could increase the overall performance compared to a Nickel biporous wick structure. From all discussed 3D-printed structures, it was observed that the octahedral structure developed by Jafari et al. has sufficient capillary performance to satisfy the operation limitation of an actual experimental setup [24].

4 Experimental loop heat pipe study

Validation of the improved numerical model demonstrated that the predicted performance is in good agreement with experimental results. It was also noted that the existing additive-manufactured octahedral structure developed by Jafari et al. could lead to a significant performance enhancement compared to an actual biporous Nickel structure and also satisfy the capillary limitations of an existing experimental setup [24]. To investigate if this 3D-printed structure actually improves the heat transfer characteristics of a loop heat pipe, a selective laser melting evaporator is fabricated and analyzed on printing quality. On top of that, this chapter aims to describe an extended approach to testing this prototype for experimental and practical applications.

4.1 Prototype design

The evaporator prototype is designed to dissipate heat from an Intel® E5-2695v4 CPU to the back of an HPE® DL360 Gen9 server chassis. The required CPU cooling area is 36.37×40.5 mm^2 and thermal design power is 120 W. To make sure that the entire CPU is covered, the prototype cooling area is 37×41 mm^2. The maximum allowed temperature of the processor - and so the limited evaporator casing temperature - may not exceed 84 °C.

4.1.1 Evaporator

The newly developed evaporator is entirely made by the selective laser melting technique using stainless steel powders (S316l). As concluded in section 1.3, a higher wall thickness could stimulate heat leak through the casing. A study by Abelea et al. reveals that an SLM-printed thin-walled stainless steel structure above 200 µm is gas-tight [78]. Note that this experiment only gives an indication about minimum wall thickness, since the evaporator in this project is printed with different settings. To make sure that pressure leakage through the wall is avoided and to create a significant contact area between the evaporator and the top plate a wall thickness of 2 mm is chosen arbitrarily. The compensation chamber and wick structure are placed on top of the CPU and have the same area as the CPU cooling area (37×41 mm^2). The size of the grooves is arbitrarily selected in a way that all fins have the same integer dimension. In total 27 fins are constructed of 1×2×39 mm^3 (width×height×length) and so 28 grooves of 0.5×2×39 mm^3 (width×height×length). Vapor is collected in a vapor outlet chamber that is separated from the compensation chamber by a 2 mm wall. The vapor outlet chamber has a length of 5 mm and has the same width as

the compensation chamber (41 mm). Most flat evaporators are constructed in a way that the vapor outlet line is below the liquid inlet and that both channels are designed on a perpendicular plane. This induces extra pressure drop inside the system (due to gravitational pressure and bent tubes) and decreases the overall performance of the heat pipe. As illustrated in figure 20, the additive manufacturing enhancement makes it possible to design a horizontal in- and outlet at the same height and at the same plane. The vapor outlet chamber shrinks over the height at an angle of 70 degrees to create a wall between the vapor chamber and the incoming liquid line. In appendix C a detailed 2D draw is given of the evaporator. Note that this draw includes an advanced base plate. Printing the evaporator including the advanced base plate as one entire structure reduces the number of machine steps and could be interesting for mass production of the design. For this project, the base plate is only printed below the evaporator design.

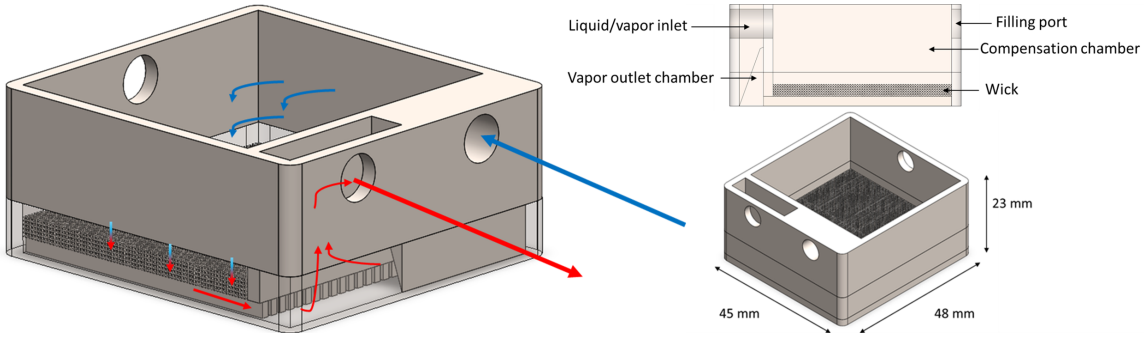

Figure 20: Global working principle of the evaporator

4.1.2 Transport lines and condenser

The transport lines were made of copper tubes since high flexibility (complex server design) and compatibility with several working fluids (Appendix A.1) are desired. Both lines have an inner and outer diameter (ID and OD) of 4 and 6 mm. In total, the length of the liquid line is 875.5 mm, including 4 bends to satisfy the server geometry. The length and number of bends of the vapor line, respectively, 330 mm and 2 bends, are smaller than the liquid line to reduce the relatively high-pressure drop induced by vapor. The condenser, and so subcooler, are also made of copper tubes due to their high thermal conductivity. Formulas in the numerical model that predict the two-phase fluid behavior inside the condenser are based on a straight tube-in-tube heat exchanger. To create a reliable comparison between experiments and the numerical model a straight condenser was constructed with

an arbitrary length of 500 mm. The geometry of the inner tube is respectively, 4 mm and 6 mm. For the outer tube, the ID and OD are 10mm and 12 mm.

4.1.3 Wick structure

The use of additive manufacturing gives wide freedom in designing and optimizing a wick structure. A study by Jafari et al. experimentally investigated that 3D printed wick structures have 1-6 times higher capillary performance compared to conventional sintered structures [24]. The authors designed an octahedral structure with a unit cell size of 500 µm and fabricated a test sample of this structure ($1\times10\times10$ mm^3) by utilizing stainless steel powders (S316l) in the SLM printing technique (fig. 21). Earlier research by Jafari et al. on this structure shows that the effective thermal conductivity of this octahedral wick structure in vacuum conditions will be around 6 W/mK for distilled water as a saturated fluid. The contact angle between distilled water and the printed structure is estimated 56.8 $\pm$0.5 [°]. The mean pore radius of the structure was investigated by scanning electron microscopy (SEM) analysis and showed that the produced wick (108 µm) has 6% deviation compared to the CAD model (115 µm). Using Archimedes method the authors measured that the average porosity of the test sample was 0.46 $\pm$ 2%. A forced liquid flow setup was used to execute permeability measurements and conclude that the test sample has a permeability of 13.05×10^{-11} m^2 according to Darcy's law. For this project the same unit cell structure and wick properties are used as described by Jafari et al [24].

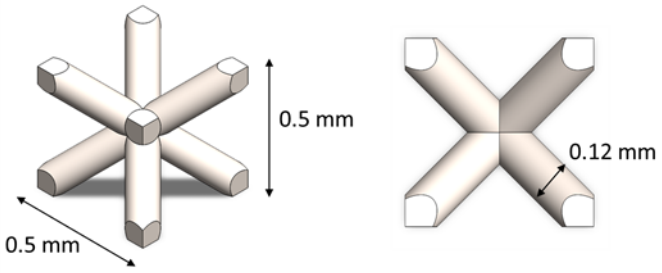

Figure 21: Octahedral unit cell

The height of the selected unit cell means that the thickness can be increased by steps of 0.5 mm. As predicted in figure 16 (b), an increasing wick thickness leads to less heat leak and better operation performance. To make sure that the fabricated structure was in good condition and to avoid contamination inside the wick, the height of the wick was chosen at 2.5 mm.

4.2 Predicted performance

The improved numerical model was utilized to estimate the operation curve and limitations of the new design by solving the energy imbalance. An evaporation coefficient of 0.1 and a sink heat transfer coefficient of 2000 W/m^{2}K were chosen, which are identical to the data Siedel et al use for their design [35]. The heat transfer coefficient of the fluid in the compensation chamber is arbitrarily selected at 1000 W/m^{2}K. Calculations were executed at a sink temperature of 20 °C and an ambient temperature of 22 °C. Figure 22 (a) shows that the evaporator casing temperature does not exceed the prescribed processor limitations of 84 °C over the entire heat range [30 - 150 W]. The evaporator thermal resistance is estimated at around 0.0959 K/W and will be approximately equal for all heat loads due to the constant evaporation coefficient (fig. 22 (b)). The overall thermal resistance shifts from 0.969 K/W at 30 W to 0.230 K/W at 150 W.

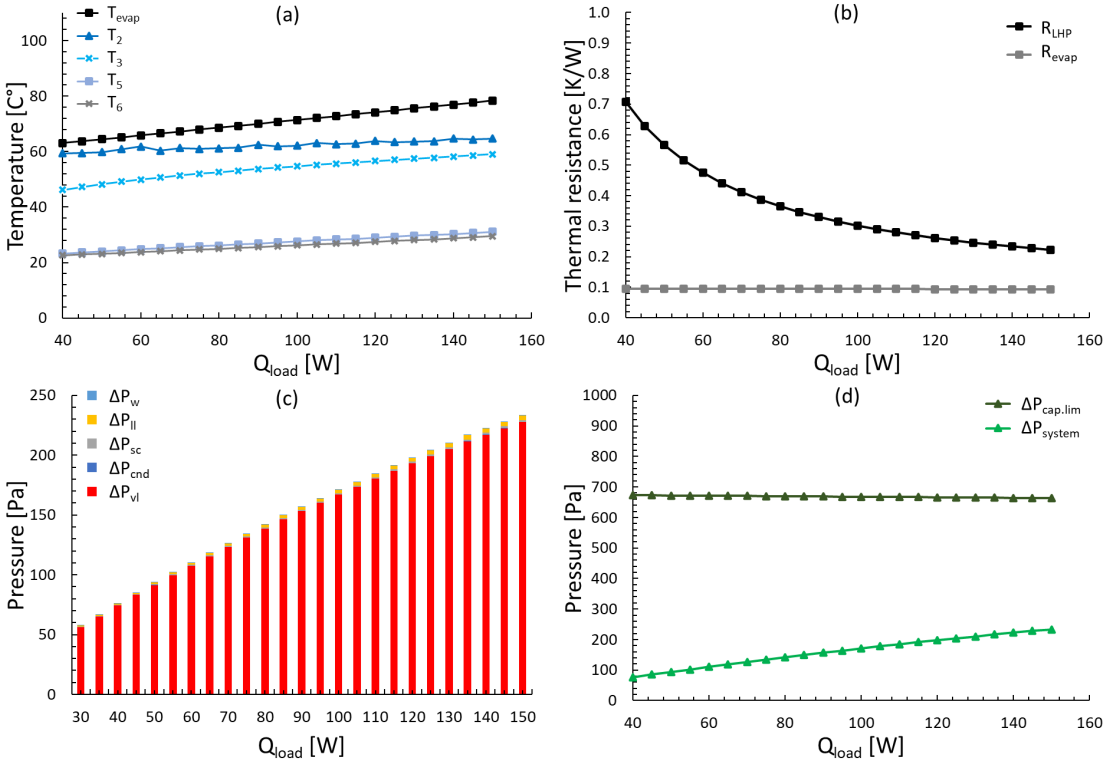

Figure 22: Steady-state prediction of new LHP design. (a) Temperatures inside the system. (b) Thermal resistance of LHP and evaporator. (c) Pressure drops inside the system. (d) Capillary limitation vs total pressure drop.

The numerical model predicts that the main pressure drop occurs inside the vapor line, nevertheless, it will not exceed the capillary limit. An often-used approach in practical applications of loop heat pipes is to use a larger vapor line tube in contrast to the liquid line diameter. The numerical model obtained that the pressure drop induced by friction of saturated vapor rapidly decreases for a larger tube diameter. This knowledge can be helpful in later research to sustain the capillary limit. The model also predicts that the high thermal conductivity of the transport lines has barely any effect on the overall performance of the system. This can be associated with the high insulation properties of the ambient h_{amb} = 5 W/m^{2}K. Finally, the boiling limitation was measured around 2 kW at the entire heat load range which is significantly higher than the actual applied heat load.

	Experimental setup		**Experimental setup**
Casing		Liquid line	
Material	SLM Stainless steel (316)	$D_{i,ll}$ / $D_{o,ll}$	4 / 6 [mm]
H_b	2 [mm]	L_{ll}	875.5 [mm]
H_{top}	0 [mm]	k_{ll}	398 [W/mK]
H_c	23 [mm]	Vapor line	
t_c	2 [mm]	$D_{i,vl}$ / $D_{o,vl}$	4 / 6 [mm]
k_c	18 [W/mK]	L_{vl}	330 [mm]
Grooves		k_{vl}	398 [W/mK]
α_{ev}	0.1 [-]	Condenser	
H_{vg} / W_{vg}	2 / 0.5 [mm]	Type of heat exchanger	Tube-in-Tube
W_f / L_f	1 / 37 [mm]	$D_{i,cond}$ / $D_{o,cond}$	4 / 6 [mm]
N_f	28 [-]	L_{cond}	500 [mm]
A_f	9.990 [cm^2]	k_{cond}	398 [W/mK]
Wick		h_{sink}	2000 [W/m^{2}K]
Material	SLM Octahedredal steel (316)	T_{sink}	20 [°C]
t_w	2.5 [mm]	General specifications	
A_w	15.17 [cm^2]	Working fluid	Distilled water
R_{wf}	0 [Km^2/W]	r_{nuc}	0.254 [µm]
k_{we}	6 [W/mK]	$\boldsymbol{\theta}$	56.8 [°]
ε	0.46 [-]	$\bar{\mathbf{M}}$	0.01805 [kg/mol]
K	1.305x10^{-10} [m^2]	h_{amb}	5 [W/m^{2}K]
r_{wp}	108 [µm]	T_{amb}	22 [°C]
Compensation chamber			
h_{cc}	1000 [W/m^{2}K]		

Table 4: Specifications of the experimental setup

4.3 Fabrication

The evaporator prototype, respectively 48×45×23 mm^3 (length×width×height), was constructed from Stainless steel (S316l) powder by SLM using a MetalFAB1 3D Metal Printing machine. The specifications of the used metal powders and the printing process are given in table 5. To avoid surface contamination the printed sample was cleaned with ethanol. A microscopic analysis of the wick structure has been conducted to verify the printing quality. Figure 23 showed an SEM image of the wick structure as well as an optical picture. The sample generated by Jafari et al. was constructed of a two-layer octahedral unit cell (thickness 1 mm), whereas this project includes 5 layers (thickness 2.5 mm). These extra layers make it more complicated to obtain the produced mean pore size, nevertheless, the pore radius is estimated at 111.5 µm. This size is slightly smaller than the CAD-model (115 µm) and is larger than the structure developed by Jafari et al. [24]. In summary, the printing quality is very close to the modeled design (± 3.5%) and allows the AM production of a wick and evaporator casing as one entire structure with controlled geometry.

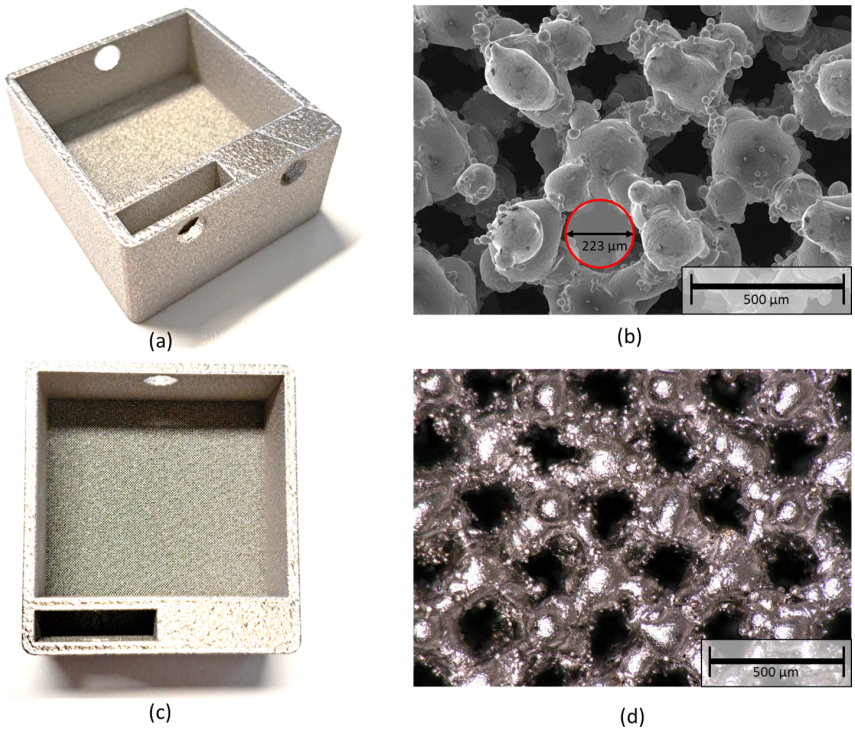

Figure 23: Printing results. (a) Additive manufactured evaporator. (b) SEM image of wick structure. (c) The top side additive manufactured evaporator. (d) Optical image of wick structure.

Commerical name	CT-316-AAKK
Material	RVS 316L powder
Particle size (minimum/maximum)	15/45 [µm]
Powder shape	Irregular
SLM machine	MetalFAB1
Laser system	SPI (Trumpf) laser 500 W
Layer thicknes	60 [µm]

Table 5: Printing specifications

In addition to the evaporator, the same design was printed with identical printing specifications only without a wick structure. As illustrated in figure 24, an optical microscope was used to measure the surface roughness inside the grooves. It is clearly observed that the small powders initiate a more or less parabolic geometry of the channels and create a high surface roughness. The small powder was also noticed in the optical images at the top side of the grooves (fig. 25)

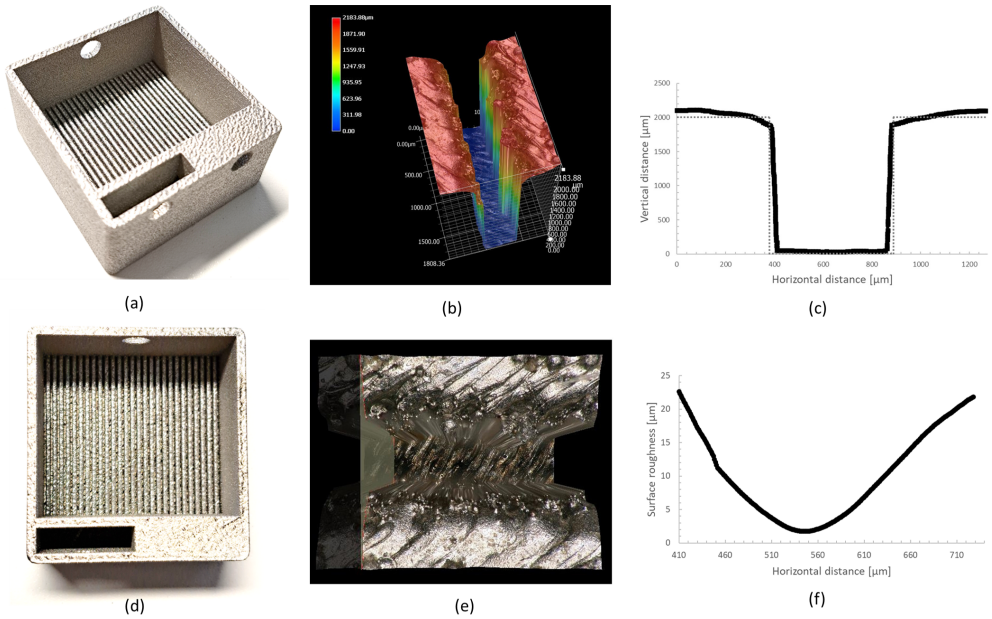

Figure 24: Printing results. (a) Additive manufactured evaporator. (b) 3D optical surface roughness measurement. (c) Surface roughness of the shape of the groove. (d) The top side of the additive-manufactured evaporator. (e) Optical image of the grooves. (f) Surface roughness within the groove.

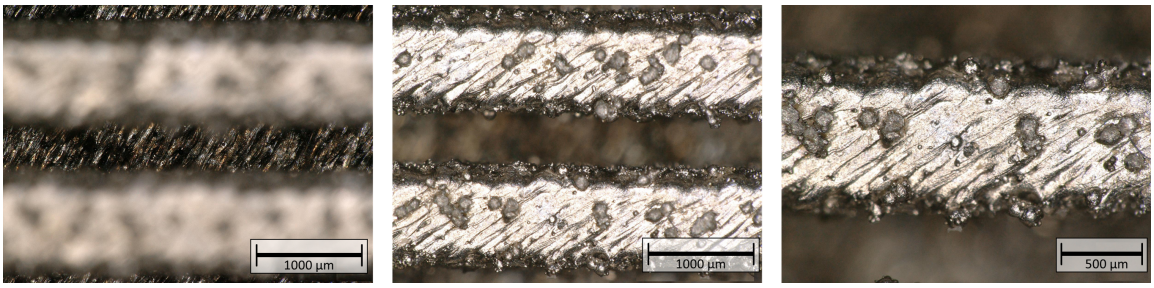

Figure 25: Optical images of the grooves.

4.4 Test-Setup for loop heat pipes

Usually, research on LHP is only focused on the experimental approach (using a heating element as a heat source and using straight heat transport lines) and not on practical applications. However, as mentioned in section 4.1, the prototype evaporator is designed in a way it can dissipate heat from an Intel® E5-2695v4 CPU within a HPE® DL360 Gen9 server. The setup is constructed in a way that can be implemented and tested into this prescribed server chassis as well as using a reliable heat element as a heat source (figure 26). Since, the Intel® E5-2695v4 CPU has a thermal design power of 120 W, the setup heat load range is chosen to be 20-150 W.

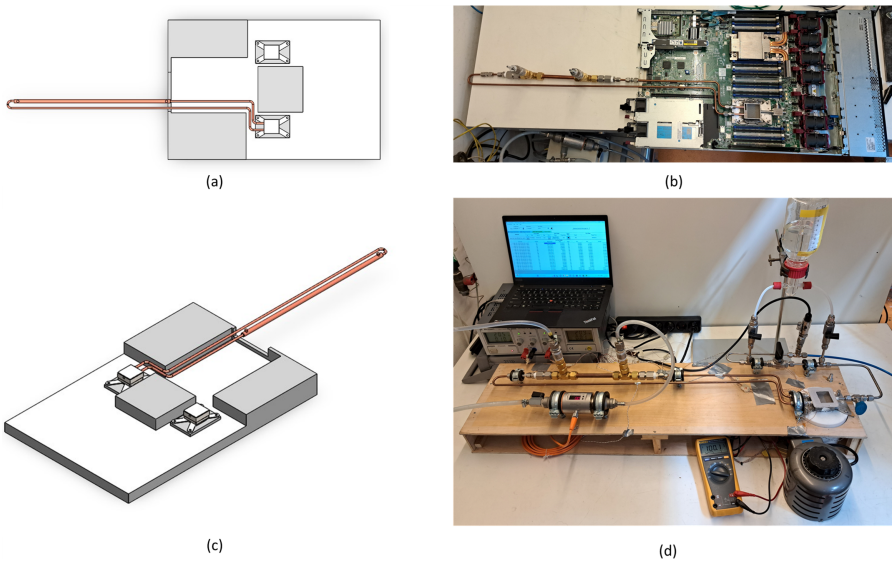

Figure 26: test-setup. (a) Schematic diagram of the test-setup. (b) LHP setup within a server chassis. (c) Schematic diagram of the test-setup. (d) LHP setup tested with a heat element.

4.4.1 Heat element

A 200W AC cartridge heater (OD 8 mm, L = 40 mm) was inserted into a copper housing (12.5×14×75 mm^3), where the end of the copper block - the interface between copper and evaporator - was sized to the mentioned CPU dimensions (37.5×41×5 mm^3). A high-conductive thermal paste was used for the cartridge heater and the evaporator surface to increase the thermal conduct with the copper. To reduce heat loss and to create a stable construction, the copper heater was insulated into a low-conductive PTFE housing. 3 T-type thermocouples (TC01,TC02 and TC03) were used to measure the applied heat flux through the solid heat element by equation 53, where k is the thermal conductivity of copper (398 W/mK) and x_1 and x_2 are the distance between the thermocouples, respectively, 11 mm and 10 mm. The applied heat load was controlled by an AC voltage regulator.

$$Q_{load} = \frac{q_{load}}{A_{CPU}} \tag{52}$$

$$q_{load} = k\left(\frac{TC01 + TC02 + TC03}{x_1 + x_2}\right) \tag{53}$$

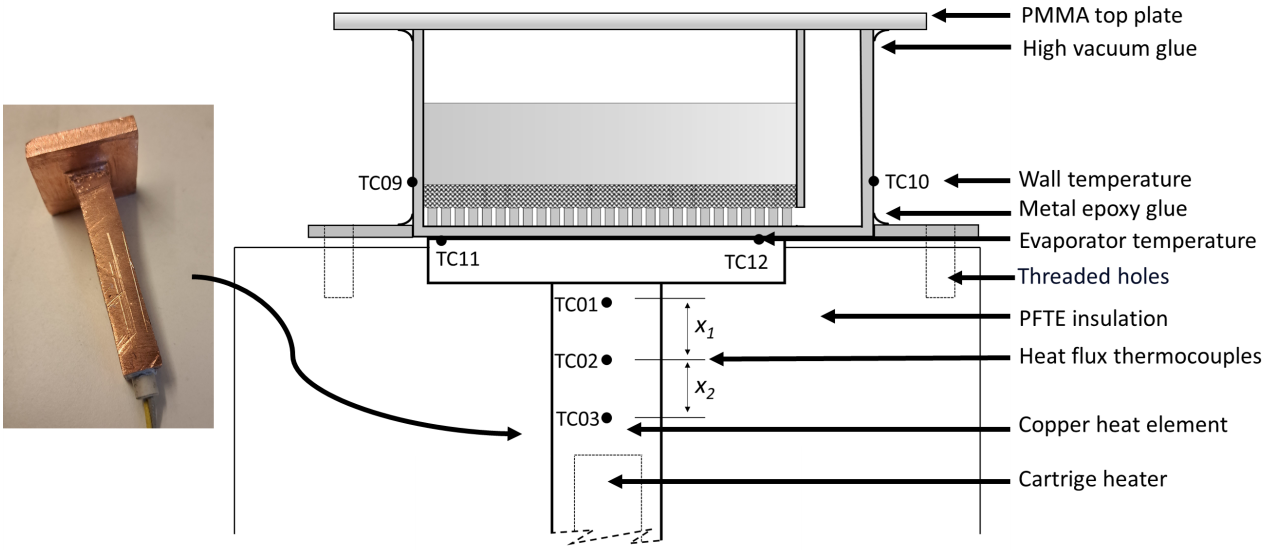

Figure 27: Schematic diagram of the experimental setup of the evaporator section and the developed copper heat source

4.4.2 Filling system

A vacuum pump (1×10^{-4} mbar) was used to remove the non-condensable gas and to create a pressure difference between the setup and the fluid tank filled with distilled water. The filling process can be described as follows: (1) Valves 3 and 4 (see figure 28) are closed and the system is evacuated by the vacuum pump. (2) Open the fourth valve and close valves 1 and 3 to remove the noncondensable gasses inside the fluid tank using a vacuum pump. (3) Now close the second and fourth valves to avoid the existence of fluid inside the pump. The system can be filled to the desired filling ratio by opening the first and third valves. (4) All valves can be closed and the cooling system can be decoupled from the filling system. An Omgega PXM409-050BUSBH absolute pressure transducer (range 0-50 bar, accuracy $\pm$ 0.08 $\%$) is placed within the filling system to estimate the amount of non-condensable gasses and check pressure leakage inside the system. The current output signal (4-20mA) is converted into a Keysight 34972A data acquisition system and connected to a DC power supply.

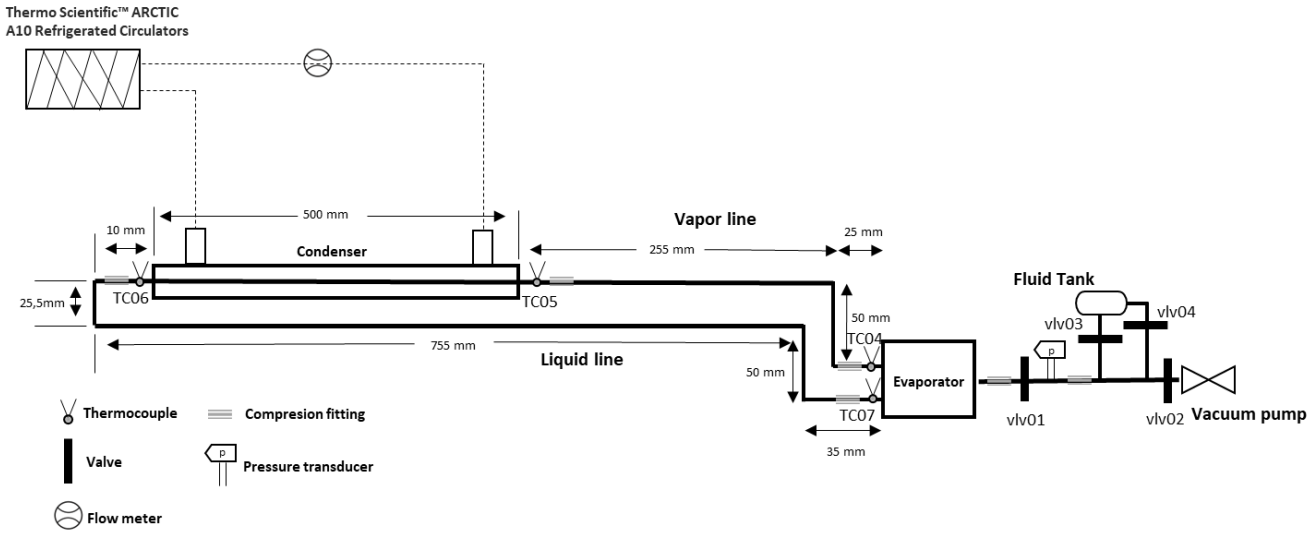

Figure 28: Schematic representation of the experiment test setup of the loop heat pipe

4.4.3 Condenser

The condenser is constructed as the tube-in-tube heat exchanger, to which a constant temperature coolant was continuously supplied by a cooling bath (ThermoScientific Artic A10). This refrigerant circulator can provide water as coolant in a range from -10 C° to 100 C° with a flow rate maximum of 17 L/min. An IFM SM7000 magnetic inductive flow meter (range 0.2 L/min - 50 L/min, accuracy 2 %) is inserted into the test setup to measure the flow rate and to obtain the heat transfer coefficient of the sink. The output data (4-20mA) is logged in a Keysight 34972A acquisition system and the flow meter is wired to a DC power supply.

4.4.4 Temperature sensors

In total, 4 T-type thermocouples are used to estimate the wall temperature at the transport line inlet and exit (TC05,TC06,TC07,TC08) and 2 for measuring the wall temperature of the evaporator body (TC09,TC10). Besides, 2 flat surface thermocouples are placed between the copper heater and prototype to measure the evaporator temperature (TC11,TC12). All used thermocouples are connected to the Keysight 34972A data acquisition system and have been calibrated in a water bath ranging from 10 C° to 50 C° (accuracy $\pm$0.5K).

4.4.5 Sealing

As shown in figure 29 (a,b), 2 aluminum base plates were glued (using 2-part epoxy for metal applications) to both ends of the evaporator prototype. This connection type and material were chosen above welding 2 stainless steel base plates to the evaporator casing, Using these base plates makes it feasible to assemble the evaporator to the server chassis and to PTFE housing. The transport lines are connected by stainless steel compression fittings to sustain the low pressure inside the system. Besides, stainless steel ball valves are used to meet the vacuum condition. Connection tubes and a transparent PMMA plate (thickness 4mm) are sealed on the prototype using high vacuum glue (Loctite Hysol 1C). This approach facilitates the ability to test the evaporator structure on the build test setup and the server design.

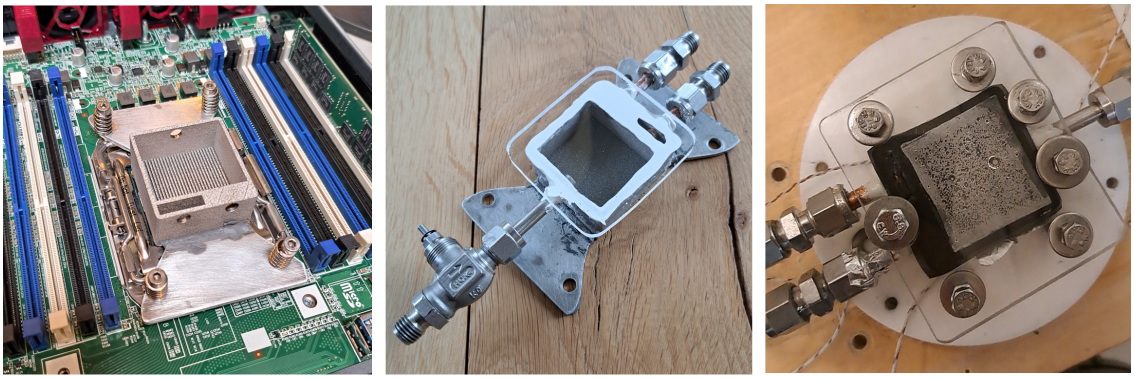

(a) (b) (c)

Figure 29: Fabricated evaporator design. (a) Within server application (b) Evaporator constructed with glue sealing. (c) Evaporator constructed with gasket.

4.5 Experimental evaluation and discussion of 3D printed loop heat pipes

Regardless, the experiments failed to accomplish, related to a pressure leakage inside the system. To make sure that the transport lines and condenser were well connected, the loop was disconnected from the evaporator prototype and 2 valves were placed at both ends. The pressure transducer was installed within the loop and after evacuating the system the pressure stays at a constant level, which excludes the influence of the loop. However, it is important to mention that often (re)connecting the compression fittings could create scratches on the tube wall, which results in small air gaps. It was attempted to avoid the pressure leakage by using a gasket between the PMMA top plate and the evaporator design as seen in figure 29 (c). The gasket was sealed by the applied mounting force on the top plate. However, both setups (glue or gasket), lead to undesired pressure increasing during the filling process. Due to limitations of time scope extra research should be executed in another project to find out where leakage occurs and how to solve it. A suggestion is to execute a helium leak test that is able to trace the gas leakage.

In brief, this section includes a new design and fabrication of a flat loop heat pipe with opposite replenishment for CPU cooling applications using SLM as a fabrication technique. The executed microscopic analysis observes the ability to print an evaporator with high printing quality, including a 2.5 mm octahedral wick structure, grooves and casing as one entire structure. Finally, it was shown that the approach to building a setup for experimental and practical applications (using PMMA top plate and vacuum glue) has complications and requires further research related to pressure leakage inside the system.

5 Pool boiling

The microscopic analysis of the 3D-printed samples in the previous chapter showed that the SLM-printed designs contain advanced surface modification, including grooves with high roughness and rough grooves combined with a wick structure. As mentioned in the section 1.5, altered surface areas could enhance the heat transfer behavior of two-phase immersion cooling applications. For that reason, the heat transfer behavior of this advanced prototype will be investigated by a pool boiling test. This chapter presents an experimental investigation and evaluation of the pool boiling heat transfer performance of these advanced prototypes

5.1 Pool boiling test-samples

Experimental research on pool boiling behavior of microchannels or lattice structures aims to investigate the heat transfer characteristics of boiling in these structures. As explained in section 1.5, the advanced surface properties of SLM-printed structures could be a potential enhancement for the heat transfer performance due to its increased surface area. The latter was clearly observed in the microscopic analysis in section 4.3. The SEM image of the wick (lattice) structure and the optical pictures of the vapor grooves (microchannels) show that small powder particles were attached to the surface. An optical roughness measurement on the microchannels monitors an irregular surface area with significant roughness. In this experimental research, the pool boiling characteristic of the two SLM-fabricated stainless steel samples in section 4.3 is explored. The first sample involves a 2.5 mm thick octahedral porous structure ($37\times41\times39$ mm^2) on top of 27 fins of $1\times2\times39$ mm^3 and 28 grooves $0.5\times2\times39$ mm^3 (width$\times$height$\times$length) together with a 2 mm thick base plate (see figure 30). The second prototype has identical specifications as the first design, however without a porous wick structure.

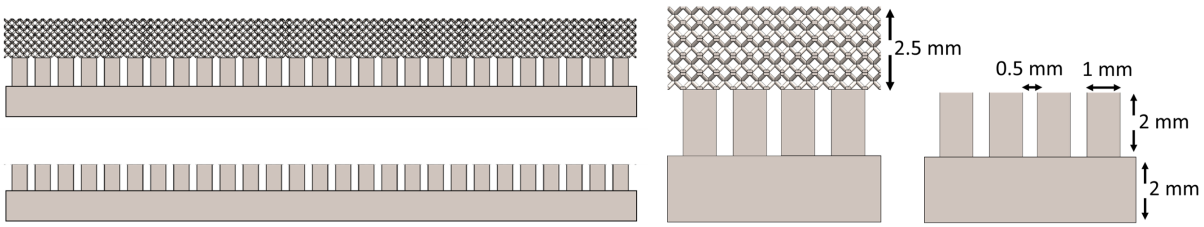

Figure 30: Test samples Microchannels and Microchannels and lattice structure

5.2 Experimental pool boiling procedure

Typically, the experimental pool boiling setup comprised a boiling facility with a working fluid circulation system and an electric heater to simulate heat flux. The test sample is placed on top of the heater and is in contact with fluid inside the boiling chamber. The design of the prototype already includes a reservoir and therefore the reservoir operates as boiling chamber (fig. 31). It is supposed that the heat leakage through the side walls is sufficiently small due to the low conductivity of the stainless steel (18 W/mK) and the relatively small level of fluid. To get rid of impurities, both designs were cleaned with acetone. All experiments were executed with 15 ml of distilled water as working fluid.

The heat transfer coefficient was calculated using equation 54, where T_{wall} is the wall temperature and T_{sat} is the saturation temperature at atmospheric pressure.

$$h = \frac{q_{load}}{T_{wall} - T_{sat}} \tag{54}$$

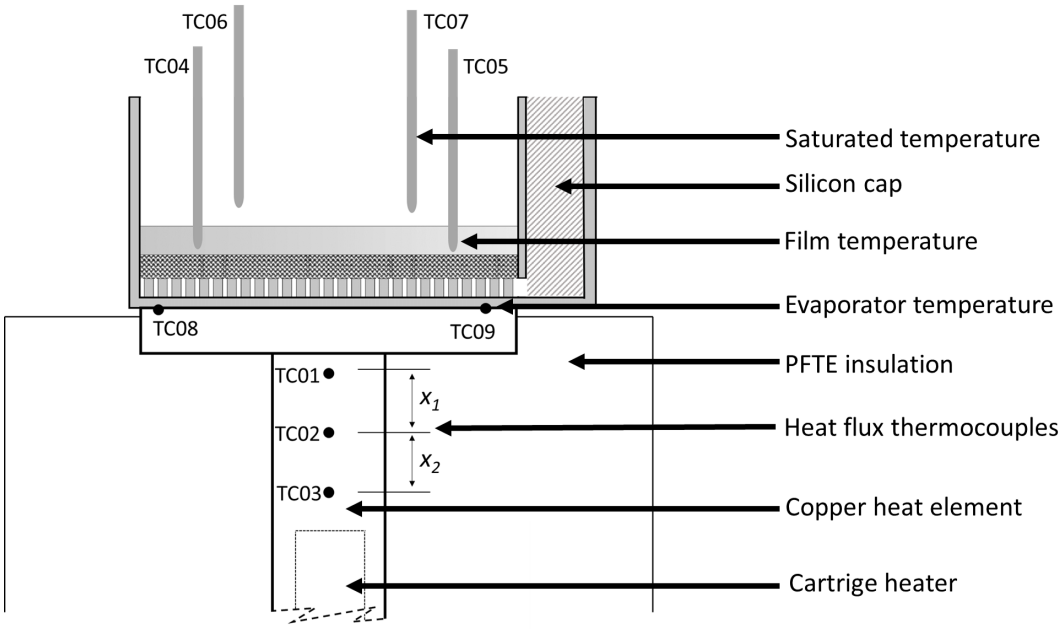

Figure 31: Schematic diagram of pool boiling test-setup

The applied heat flux in this equation was determined with the same approach as described in section 4.4.1. The 200 W AC cartridge heater (OD 8 mm, L = 40 mm) was inserted into a copper housing ($12.5\times14\times75$ mm^3) and insulated using PTFE. The heat flux was measured with the same approach as derived with equation 53, using 3 T-type thermocouples (TC01, TC02,TC03) over a distance, respectively, 11 mm and 10 mm. An AC Voltage regulator was used to control the applied heat. The end side of the heat source has a thickness of 5 mm and a surface area (37.5×41 mm^2). This means that the present work will only evaluate pool boiling behavior for relatively low heat fluxes (<8 W/cm^2). Conventional pool boiling test facilities contain a refilling system to condense the generated vapor bubbles inside the system. Usually, pool boiling tests are executed on a wide heat load range from 5 W/cm^2 to the critical heat flux and have a large set of data points. As mentioned, this research is only focused on low heat fluxes and therefore the number of tests is significantly reduced compared to conventional experiments. For that reason, the test facility does not involve a condensation section and the reservoir will be refilled each experiment after dry-out is reached. During experiments, it was observed that the working fluid has the tendency to boil first within the small vapor outlet chamber (fig. 3). To prevent this behavior a silicon cap was placed inside this chamber as displayed in figure 31).

As shown in figure 32, the prototype was fixed on the heat source by mounting a 4 mm PMMA top plate to the PFTFE housing. The vapor can leave the boiling reservoir to the atmosphere by a 12 mm OD opening created in the top plate. 4 small gaps (OD 1 mm) were inserted into the PMMA plane to guide 4 T-type thermocouples into a stable position. 2 of these sensors were used to measure the film temperature (TC04,TC05) and 2 were utilized to obtain the saturated fluid temperature (TCO6, TCO7). The evaporator temperature was determined using 2 flat T-type thermocouples (TC08,TC09) between the prototype/heat source interface. All thermocouples have been calibrated in a water bath ranging from 10 °C to 50 °C (accuracy $\pm$0.5°C) and are connected to a Keysight 34972A acquisition system.

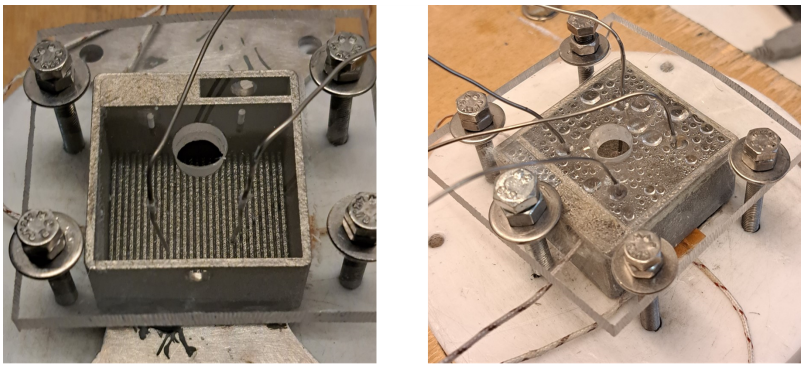

Figure 32: Experimental test-setup. (a) Before operation. (b) During operation.

5.3 Experimental pool boiling results and discussion

The experimental outcome of this research is shown in figure 33, where it is observed that the additive-manufactured microchannels in this research show significantly higher heat transfer performance compared to the test sample including the lattice structure. To explain this phenomenon a deeper understanding of the bubble dynamics and the vapor-liquid interaction inside the microchannels and lattice structure is required, and therefore it is recommended to execute later research using a high-speed camera. To the author's knowledge, there is no former research work into the pool boiling behavior of an additive manufactured combination of lattice structure and microchannels. However, in the low heat flux range it is observed that the SLM fabricated stainless steel lattice structure (1.1 mm) developed by Zhang et al. has a smaller heat transfer coefficient compared to 3D printed υ-shaped bronze microchannels by Pi et al. (fig. 34) [42, 43].

Further, figure 33 illustrates that the advanced surface modification of the additive manufactured microchannels leads to a significant performance enhancement compared to a plain copper surface tested by Wong and Leong [82]. For heat fluxes below 6 W/cm^2, the test sample including microchannels only also shows a distinctive heat transfer improvement compared to a stainless steel Octet-3.0C-2.5 structure fabricated by Wong and Leoung [82]. The comparison of pool boiling behavior for heat fluxes larger than 8 W/cm^2 could not be made, due to the limitations of the experimental setup. Nevertheless, it is interesting to mention that 3D printed microchannel has a higher initial heat transfer coefficient, since electronic components often operate in this low heat flux range. Understanding this behavior could be an important approach to optimizing the heat transfer performance at low heat fluxes. For both samples, it is observed that the slope of the heat transfer performance

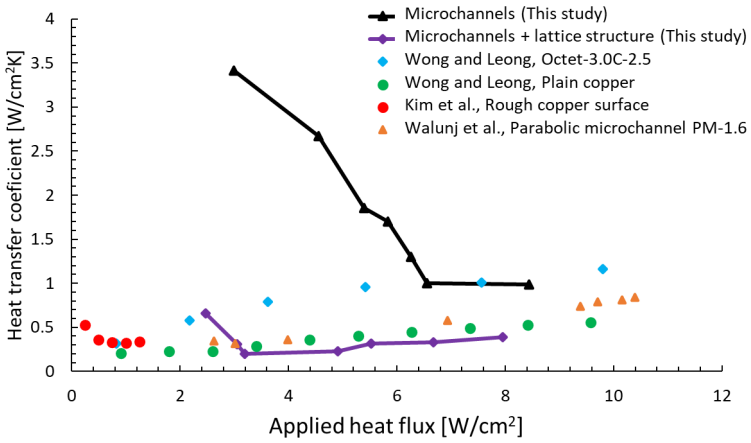

Figure 33: Experimental obtained heat transfer coefficient for the additive manufactured test samples compared to actual pool boiling investigations

reduces in the lower heat flux range till a certain transition point. The transition point for microchannels only occurs around 7 W/cm^2 and for microchannels in combination with a lattice structure the transition point shifts to the lower heat flux area and is approximately around 4 W/cm^2. The decline heat transfer slope in the low heat flux area and the presence of a transition point is remarkable since experimental data from literature frequently observe an increasing linear or quasi-linear tendency [40]. However, in figure 34 it is shown that an experimental investigation by Pi et al. on 3D printed υ-shaped bronze microchannels with water as working fluid noticed the same behavior [43]. The authors associate this trend with the obstruction of bubble clusters during bubble departure. The formation of bubbles is initiated by the active nucleation sides on the heated surface. As the heat transfer at this nucleation side increases, the bubbles tend to grow and accelerate to departure. Depending on the size and shape of the microchannels, the bubbles merge together into columns. As concluded by Pi et al. this coalescence could partly hinder the bubble departure and heat dissipation from the sample surface and so decrease the heat transfer performance. Using a high-speed camera, the authors also observe that for higher heat fluxes - after the transition point - the bubble motion increases and the vapor blanket periodically disappears [43]. For water as working fluid, a curved tendency was also observed in an investigation on copper-sintered υ-shaped reentrant porous microchannels by Deng et al. [83] and an advanced copper interconnected microchannel network by Tang et al. [84] (fig. 34). As shown in figure 33, the observation of an initial high heat transfer coefficient and a decreasing slope was also found by Kim et al. [85]. Their pool boiling investigation with water as working fluid was executed on several copper structures with different surface

roughness varied from 0.042 to 1.54 µm with corresponding contact angles ranging from 116 ° to 153 °. It was observed that vapor blanketing is initiated more by a higher average surface roughness and contact angle. For the investigated hydrophobic samples ($\theta > 90$ °) with a higher surface roughness the heat transfer coefficient slope decreased more rapidly as the heat flux increased. The high surface roughness of the test samples in this project - as outlined in section 4.3 - could explain the occuring trend as shown in figure 33. In addition to the surface morphology, a study by Walunj and Sathyabhama revealed that the microchannel geometry could create vapor blanketing [86]. The pool boiling characteristics of rectangular, parabolic and stepped copper microchannels were tested and compared for different geometries. For the parabolic channel with a top/base ratio of 1.6, a decline in heat transfer coefficient slope was measured as shown in figure 33. This is interesting since the executed microscopic analysis in section 4.3, shows that the SLM printed grooves have a parabolic shape. As mentioned, the remarkable initial heat transfer characteristics could be related to the geometry and surface morphology of the microchannels, nevertheless, it is hard to define to which specific structures this behavior occurs. Additive manufacturing enables rapid prototyping with controlled geometry and surface roughness (powder size), which could help to predict the behavior in future development.

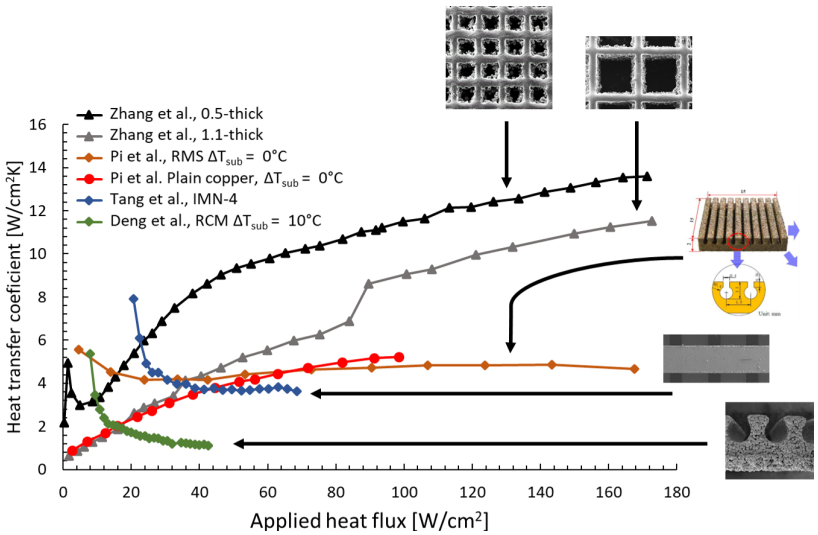

Figure 34: Heat transfer characteristics of various investigations in literature

6 Conclusion and recommendation

In conclusion, the performance enhancement of additive manufactured structures in two-phase applications has demonstrated significant advantages in terms of heat transfer capability and design flexibility. A new improved steady-state numerical model for flat loop heat pipes with opposite replenishment has been developed that describes heat transfer inside the evaporator and the loop accurately in good agreement with two existing experimental setups. The flexibility of the steady-state model enabled the implementation of heat transfer and pressure drop equations for vapor grooves, for bends inside the transport lines and for a new more advanced condenser design for later research. The latter is suggested since experimental validation observed that the steady-state model is sensitive to the type of heat exchanger that is used. A parametric study revealed that the evaporation coefficient and the heat transfer coefficient of fluid inside the compensation chamber have a significant influence on the operation behavior of loop heat pipes. It is advised to execute new research on the effect of an additive-manufactured surface on this evaporation coefficient. Further, the heat transfer coefficient of the fluid inside the compensation chamber requires a more precise evaluation. In addition, the numerical model does not describe the heat transfer through the base plate and fins which is recommended for design optimization aims in later research.

The numerical model suggested that the development of an additive manufactured multi-material evaporator, including 0.5 mm thick stainless steel casing and copper wick/groove results in a significant performance enhancement compared to an actual loop heat pipe. The model showed the relevance of new studies on high-conductive additive manufactured materials such as copper, the ability of multi-material printing and the implementation of artificial intelligence-driven tools for design optimization of an additive manufactured wick. It was also observed that an existing low-conductive 3D-printed stainless steel octahedral structure satisfies the operation limitation of an actual experimental setup and has a performance enhancement compared to an existing biporous Nickel wick structure due to its higher effective thermal conductivity.

The identical octhahedral stainless steel wick structure from the literature was reproduced by fabricating 5 octahedral unit cell layers together with rectangular grooves and the evaporator casing. A microscopic analysis of the fabricated selective laser melting evaporator showed the ability to print the entire structure with high printing quality. The mean pore

size of the fabricated wick structure was very close to the CAD-model ($\pm$ 3.5 %) and enabled the production of wick structures with controlled geometry. Furthermore, an identical design was printed without a wick structure and optically observed a high surface roughness of the grooves related to the small powders. It was also shown that additive manufacturing of rectangular grooves leads to more or less parabolic structure. The evaporator prototype was designed to facilitate experiments in practical (server design) and experimental applications, however, it was observed that the experiments failed to accomplish related to a pressure leakage inside the system. It is suggested to execute a helium leak test to detect the location of the leakage inside the system.

In addition to the numerically obtained enhancement of additive manufactured loop heat pipe structures, it is experimentally observed that 3D printing leads to a significant performance enhancement of two-phase immersion cooling. A pool boiling test on additive manufactured microchannels and microchannels including a lattice wick structure was executed for low heat fluxes (< 8 W/cm^2). It was observed that microchannels only had better heat transfer characteristics than the more advanced lattice structure. It is suggested to execute further research with higher heat loads and use a high-speed camera to observe the complex bubble dynamics within the lattice structure. Besides, the experimental investigation showed that additive-manufactured microchannels had a higher initial heat transfer coefficient compared to a plain copper surface and a stainless steel Octet-3.0C-2.5 lattice structure in the literature. This high initial heat transfer coefficient is followed by a rapid decline caused by vapor blankets that hinder heat dissipation from the surface. The same trend was observed in literature for 3D-printed υ-shaped microchannels, additive manufactured lattice structures, rough surfaces and parabolic structures. A new extended study with several microchannel geometries and surface roughness is recommended to get a better understanding of this complex pool boiling behavior at low heat fluxes.

Overall, additive-manufactured two-phase cooling systems appear to be a significant performance enhancement compared to actual two-phase cooling systems and could play a key role in achieving worldwide sustainability goals.

References

[1] Carolina Koronen, Max Åhman, and Lars J Nilsson. "Data centres in future European energy systems energy efficiency, integration and policy". In: *Energy Efficiency* 13.1 (Jan. 2020), pp. 129–144. ISSN: 1570-646X. DOI: 10.1007/s12053-019-09833-8.

[2] Martijn Koot and Fons Wijnhoven. "Usage impact on data center electricity needs: A system dynamic forecasting model". In: *Applied Energy* 291 (June 2021), p. 116798. ISSN: 03062619. DOI: 10.1016/j.apenergy.2021.116798.

[3] Anders Andrae and Tomas Edler. "On Global Electricity Usage of Communication Technology: Trends to 2030". In: *Challenges* 6.1 (Apr. 2015), pp. 117–157. ISSN: 2078-1547. DOI: 10.3390/challe6010117.

[4] Z. Song, X. Zhang, and C. Eriksson. "Data Center Energy and Cost Saving Evaluation". In: *Energy Procedia* 75 (Aug. 2015), pp. 1255–1260. ISSN: 18766102. DOI: 10.1016/j.egypro.2015.07.178.

[5] Chaoqiang Jin et al. "A review of power consumption models of servers in data centers". In: *Applied Energy* 265 (May 2020), p. 114806. ISSN: 03062619. DOI: 10.1016/j.apenergy.2020.114806.

[6] Miyuru Dayarathna, Yonggang Wen, and Rui Fan. "Data Center Energy Consumption Modeling: A Survey". In: *IEEE Communications Surveys & Tutorials* 18 (2016). DOI: 10.1109/COMST.2015.2481183.

[7] Yifan Sun et al. "Summarizing CPU and GPU Design Trends with Product Data". In: *Northeastern University* (2019). DOI: 10.48550/arXiv.1911.11313.

[8] Yelong Zhang et al. "Cooling technologies for data centres and telecommunication base stations : A comprehensive review". In: *Journal of Cleaner Production* 334 (Feb. 2022), p. 130280. ISSN: 09596526. DOI: 10.1016/j.jclepro.2021.130280.

[9] Mahmoud Amin et al. "Improving the Data Center Servers Cooling Efficiency via Liquid Cooling-based Heat Pipes". In: *2020 IEEE Industry Applications Society Annual Meeting*. IEEE, Oct. 2020, pp. 1–5. ISBN: 978-1-7281-7192-0. DOI: 10.1109/IAS44978.2020.9334731.

[10] Yin Zhang, Zhiyuan Wei, and Mingshan Zhang. "Free cooling technologies for data centers: energy saving mechanism and applications". In: *Energy Procedia* 143 (Dec. 2017), pp. 410–415. ISSN: 18766102. DOI: 10.1016/j.egypro.2017.12.703.

[11] Lijun Liu et al. "State-of-the-art on thermal energy storage technologies in data center". In: *Energy and Buildings* 226 (Nov. 2020), p. 110345. ISSN: 03787788. DOI: 10.1016/j.enbuild.2020.110345.

[12] Jessica Gullbrand et al. "Liquid Cooling of Compute System". In: *Journal of Electronic Packaging* 141.1 (Mar. 2019). ISSN: 1043-7398. DOI: 10.1115/1.4042802.

[13] Nugroho Agung Pambudi et al. "The immersion cooling technology: Current and future development in energy saving". In: *Alexandria Engineering Journal* 61.12 (Dec. 2022), pp. 9509–9527. ISSN: 11100168. DOI: 10.1016/j.aej.2022.02.059.

[14] Munonyedi Egbo. "A review of the thermal performance of vapor chambers and heat sinks: Critical heat flux, thermal resistances, and surface temperatures". In: *International Journal of Heat and Mass Transfer* 183 (Feb. 2022), p. 122108. ISSN: 00179310. DOI: 10.1016/j.ijheatmasstransfer.2021.122108.

[15] Xiaohong Han et al. "Review of the development of pulsating heat pipe for heat dissipation". In: *Renewable and Sustainable Energy Reviews* 59 (June 2016), pp. 692–709. ISSN: 13640321. DOI: 10.1016/j.rser.2015.12.350.

[16] Yu. F. Gerasimov et al. "Low-temperature heat pipes with separate channels for vapor and liquid". In: *Journal of Engineering Physics* 28.6 (June 1975), pp. 683–685. ISSN: 0022-0841. DOI: 10.1007/BF00867371.

[17] Y.F. Maidanik et al. "Some Results of Loop Heat Pipes Development, Tests and Application in Engineeri". In: *Proc. of the 5th International peat pipe symposium Melbourne Australia* (1996), pp. 406–412.

[18] Jobin Jose and Rajesh Baby. "Recent advances in loop heat pipes : A review". In: *IOP Conference Series: Materials Science and Engineering* 396 (Aug. 2018), p. 012060. ISSN: 1757-899X. DOI: 10.1088/1757-899X/396/1/012060.

[19] Yu.F. Maydanik, M.A. Chernysheva, and V.G. Pastukhov. "Review: Loop heat pipes with flat evaporators". In: *Applied Thermal Engineering* 67.1-2 (June 2014), pp. 294–307. ISSN: 13594311. DOI: 10.1016/j.applthermaleng.2014.03.041.

[20] Yury Maydanik, Mariya Chernysheva, and Sergey Vershinin. "High-Capacity Loop Heat Pipe with Flat Evaporator for Efficient Cooling Systems". In: *Journal of Thermophysics and Heat Transfer* 34.3 (July 2020), pp. 465–475. ISSN: 1533-6808. DOI: 10.2514/1.T5845.

[21] Yu.F. Maydanik, S.V. Vershinin, and M.A. Chernysheva. "Comparison tests of loop heat pipes with flat evaporators of different types". In: *International Journal of Heat and Mass Transfer* 186 (May 2022), p. 122491. ISSN: 00179310. DOI: 10.1016/j.ijheatmasstransfer.2021.122491.

[22] Pawel Szymanski et al. "Recent Advances in Loop Heat Pipes with Flat Evaporator". In: *Entropy* 23.11 (Oct. 2021), p. 1374. ISSN: 1099-4300. DOI: 10.3390/e23111374.

[23] Pawel Szymanski, Dariusz Mikielewicz, and Sasan Fooladpanjeh. "Current Trends in Wick Structure Construction in Loop Heat Pipes Applications: A Review". In: *Materials* 15.16 (Aug. 2022), p. 5765. ISSN: 1996-1944. DOI: 10.3390/ma15165765.

[24] Davoud Jafari, Wessel W. Wits, and Bernard J. Geurts. "Metal 3D-printed wick structures for heat pipe application: Capillary performance analysis". In: *Applied Thermal Engineering* 143 (Oct. 2018), pp. 403–414. ISSN: 13594311. DOI: 10.1016/j.applthermaleng.2018.07.111.

[25] A.J. Robinson et al. "A wicked heat pipe fabricated using metal additive manufacturing". In: *International Journal of Thermofluids* 12 (Nov. 2021), p. 100117. ISSN: 26662027. DOI: 10.1016/j.ijft.2021.100117.

[26] J. Esarte et al. "Optimizing the design of a two-phase cooling system loop heat pipe: Wick manufacturing with the 3D selective laser melting printing technique and prototype testing". In: *Applied Thermal Engineering* 111 (Jan. 2017), pp. 407–419. ISSN: 13594311. DOI: 10.1016/j.applthermaleng.2016.09.123.

[27] Zhuohuan Hu et al. "Development of a loop heat pipe with the 3D printed stainless steel wick in the application of thermal management". In: *International Journal of Heat and Mass Transfer* 161 (Nov. 2020), p. 120258. ISSN: 00179310. DOI: 10.1016/j.ijheatmasstransfer.2020.120258.

[28] Davoud Jafari, Wessel W. Wits, and Bernard J. Geurts. "An investigation of porous structure characteristics of heat pipes made by additive manufacturing". In: *2017 23rd International Workshop on Thermal Investigations of ICs and Systems (THERMINIC)*. IEEE, Sept. 2017, pp. 1–7. ISBN: 978-1-5386-1928-5. DOI: 10.1109/THERMINIC.2017.8233841.

[29] B. Richard, W.G. Anderson, and J. Crawmer. "Development of a 3D Printed Loop Heat Pipe". In: *35th Semiconductor Thermal Measurement, Modeling and Management Symposium (SEMI-THERM), San Jose, CA, USA* (2019), pp. 58–60.

[30] Ji Li, Daming Wang, and G. P. Bud Peterson. "A Compact Loop Heat Pipe With Flat Square Evaporator for High Power Chip Cooling". In: *IEEE Transactions on Components, Packaging and Manufacturing Technology* 1.4 (Apr. 2011), pp. 519–527. ISSN: 2156-3950. DOI: 10.1109/TCPMT.2010.2099531.

[31] Benjamin Siedel, Valérie Sartre, and Frédéric Lefèvre. "Literature review: Steady-state modelling of loop heat pipes". In: *Applied Thermal Engineering* 75 (Jan. 2015), pp. 709–723. ISSN: 13594311. DOI: 10.1016/j.applthermaleng.2014.10.030.

[32] Tarik Kaya et al. "Mathematical modeling of loop heat pipes". In: *37th Aerospace Sciences Meeting and Exhibit*. Reston, Virigina: American Institute of Aeronautics and Astronautics, Jan. 1999. DOI: 10.2514/6.1999-477.

[33] Abhijit Avinash Adoni et al. "Theoretical and Experimental Studies on an Ammonia-Based Loop Heat Pipe With a Flat Evaporator". In: *IEEE Transactions on Components and Packaging Technologies* 33.2 (June 2010), pp. 478–487. ISSN: 1521-3331. DOI: 10.1109/TCAPT.2010.2042056.

[34] Abhijit A. Adoni et al. "Thermohydraulic Modeling of Capillary Pumped Loop and Loop Heat Pipe". In: *Journal of Thermophysics and Heat Transfer* 21.2 (Apr. 2007), pp. 410–421. ISSN: 0887-8722. DOI: 10.2514/1.26222.

[35] Benjamin Siedel, Valérie Sartre, and Frédéric Lefèvre. "Complete analytical model of a loop heat pipe with a flat evaporator". In: *International Journal of Thermal Sciences* 89 (Mar. 2015), pp. 372–386. ISSN: 12900729. DOI: 10.1016/j.ijthermalsci.2014.11.014.

[36] Dhruv Varma. *Two-phase versus Single-phase immersion cooling*. Nov. 2019.

[37] Guan Heng Yeoh and Xiaobin Zhang. "Computational fluid dynamics and population balance modelling of nucleate boiling of cryogenic liquids: Theoretical developments". In: *The Journal of Computational Multiphase Flows* 8.4 (Dec. 2016), pp. 178–200. ISSN: 1757-482X. DOI: 10.1177/1757482X16674217.

[38] Pin Chen, Souad Harmand, and Safouene Ouenzerfi. "Immersion cooling effect of dielectric liquid and self-rewetting fluid on smooth and porous surface". In: *Applied Thermal Engineering* 180 (Nov. 2020), p. 115862. ISSN: 13594311. DOI: 10.1016/j.applthermaleng.2020.115862.

[39] Daehoon Kang et al. "Recent Advances in Two-Phase Immersion Cooling with Surface Modifications for Thermal Management". In: *Energies* 15.3 (Feb. 2022), p. 1214. ISSN: 1996-1073. DOI: 10.3390/en15031214.

[40] Robert Kaniowski and Robert Pastuszko. "Pool Boiling of Water on Surfaces with Open Microchannels". In: *Energies* 14.11 (May 2021), p. 3062. ISSN: 1996-1073. DOI: 10.3390/en14113062.

[41] Houli Liu et al. "Enhancement of pool boiling heat transfer using 3D-printed groove structure". In: *International Journal of Heat and Mass Transfer* 183 (Feb. 2022), p. 122155. ISSN: 00179310. DOI: 10.1016/j.ijheatmasstransfer.2021.122155.

[42] Chi Zhang et al. "Performance of pool boiling with 3D grid structure manufactured by selective laser melting technique". In: *International Journal of Heat and Mass Transfer* 128 (Jan. 2019), pp. 570–580. ISSN: 00179310. DOI: 10.1016/j.ijheatmasstransfer.2018.09.021.

[43] Guang Pi et al. "Pool boiling performance of 3D-printed reentrant microchannels structures". In: *International Journal of Heat and Mass Transfer* 156 (Aug. 2020), p. 119920. ISSN: 00179310. DOI: 10.1016/j.ijheatmasstransfer.2020.119920.

[44] Haozhi Bian et al. "Enhanced nucleate boiling on 3D-printed micro-porous structured surface". In: *Applied Thermal Engineering* 141 (Aug. 2018), pp. 422–434. ISSN: 13594311. DOI: 10.1016/j.applthermaleng.2018.05.107.

[45] McGlen R.J, Kew P.A., and Reay D.A. *Heat Pipes Theory, Design and Applications*. 6th ed. Oxford OX5 1AJ, UK: Elsevier, 2014. ISBN: 9780080982663. DOI: 10.1016/C2011-0-08979-2.

[46] Van P. Carey. *Liquid-Vapor Phase-Change Phenomena*. CRC Press, Feb. 2020. ISBN: 9780429082221. DOI: 10.1201/9780429082221.

[47] Tarik Kaya and John Goldak. "Numerical analysis of heat and mass transfer in the capillary structure of a loop heat pipe". In: *International Journal of Heat and Mass Transfer* 49.17-18 (Aug. 2006), pp. 3211–3220. ISSN: 00179310. DOI: 10.1016/j.ijheatmasstransfer.2006.01.028.

[48] Patrik Nemec, Alexander Čaja, and Milan Malcho. "Mathematical model for heat transfer limitations of heat pipe". In: *Mathematical and Computer Modelling* 57.1-2 (Jan. 2013), pp. 126–136. ISSN: 08957177. DOI: 10.1016/j.mcm.2011.06.047.

[49] Jentung Ku. "Loop heat pipe startup behaviors". In: *International Conference on Environmental Systems (No. ICES-2016-24)* (July 2016).

[50] Lizhan Bai, Guiping Lin, and Dongsheng Wen. "Modeling and analysis of startup of a loop heat pipe". In: *Applied Thermal Engineering* 30.17-18 (Dec. 2010), pp. 2778–2787. ISSN: 13594311. DOI: 10.1016/j.applthermaleng.2010.08.004.

[51] M. Nishikawara et al. “Liquid vapor phase behavior and operating characteristics of the capillary evaporator of a loop heat pipe at start-up”. In: *International Journal of Thermal Sciences* 129 (July 2018), pp. 426–433. ISSN: 12900729. DOI: 10.1016/j.ijthermalsci.2018.03.023.

[52] Yu.F. Maydanik. “Loop heat pipes”. In: *Applied Thermal Engineering* 25.5-6 (Apr. 2005), pp. 635–657. ISSN: 13594311. DOI: 10.1016/j.applthermaleng.2004.07.010.

[53] Nguyen Phan et al. “Flat-evaporator-type loop heat pipe with hydrophilic polytetrafluoroethylene porous membranes”. In: *Physics of Fluids* 32.4 (Apr. 2020), p. 047108. ISSN: 1070-6631. DOI: 10.1063/1.5143561.

[54] Stéphane Launay, Valérie Sartre, and Jocelyn Bonjour. “Analytical Model for Characterization of Loop Heat Pipes”. In: *Journal of Thermophysics and Heat Transfer* 22.4 (Oct. 2008), pp. 623–631. ISSN: 0887-8722. DOI: 10.2514/1.37439.

[55] J. Ku. “Operating Characteristics of Loop Heat Pipes”. In: *Journal of Aerospace* 108 (1999), pp. 503–519.

[56] Randeep Singh, Aliakbar Akbarzadeh, and Masataka Mochizuki. “Operational characteristics of the miniature loop heat pipe with non-condensable gases”. In: *International Journal of Heat and Mass Transfer* 53.17-18 (Aug. 2010), pp. 3471–3482. ISSN: 00179310. DOI: 10.1016/j.ijheatmasstransfer.2010.04.008.

[57] Jiang He et al. “Effect of non-condensable gas on the operation of a loop heat pipe”. In: *International Journal of Heat and Mass Transfer* 70 (Mar. 2014), pp. 449–462. ISSN: 00179310. DOI: 10.1016/j.ijheatmasstransfer.2013.11.043.

[58] S.C. Zhao et al. “Experimental study on global visualization of loop heat pipe with a flat disk-shaped evaporator”. In: *Energy Reports* 8 (Nov. 2022), pp. 10895–10912. ISSN: 23524847. DOI: 10.1016/j.egyr.2022.08.240.

[59] Yong Li et al. “Effects of vacuuming process parameters on the thermal performance of composite heat pipes”. In: *Applied Thermal Engineering* 99 (Apr. 2016), pp. 32–41. ISSN: 13594311. DOI: 10.1016/j.applthermaleng.2016.01.035.

[60] Benjamin Siedel, Valérie Sartre, and Frédéric Lefèvre. “Numerical investigation of the thermohydraulic behaviour of a complete loop heat pipe”. In: *Applied Thermal Engineering* 61.2 (Nov. 2013), pp. 541–553. ISSN: 13594311. DOI: 10.1016/j.applthermaleng.2013.08.017.

[61] Melanie Bonnefoy et al. "Effective Thermal Conductivity of Saturated Sintered Nickel Loop Heat Pipe Wicks". In: *37th AIAA Thermophysics Conference*. Reston, Virigina: American Institute of Aeronautics and Astronautics, June 2004. ISBN: 978-1-62410-035-2. DOI: 10.2514/6.2004-2571.

[62] R. Marek and J. Straub. "Analysis of the evaporation coefficient and the condensation coefficient of water". In: *International Journal of Heat and Mass Transfer* 44.1 (Jan. 2001), pp. 39–53. ISSN: 00179310. DOI: 10.1016/S0017-9310(00)00086-7.

[63] I.W. Eames, N.J. Marr, and H. Sabir. "The evaporation coefficient of water: a review". In: *International Journal of Heat and Mass Transfer* 40.12 (Aug. 1997), pp. 2963–2973. ISSN: 00179310. DOI: 10.1016/S0017-9310(96)00339-0.

[64] Jeehoon Choi et al. "Interface engineering to enhance thermal contact conductance of evaporators in miniature loop heat pipe systems". In: *Applied Thermal Engineering* 60.1-2 (Oct. 2013), pp. 371–378. ISSN: 13594311. DOI: 10.1016/j.applthermaleng.2013.06.060.

[65] Myron B. Allen and Eli L. Isaacson. *Numerical Analysis for Applied Science*. 1st ed. Vol. 492. John Wiley & Sons, Nov. 1997.

[66] Y. Maydanik, V. Pastukhov, and M. Chernysheva. "Development and investigation of a loop heat pipe with a high heat-transfer capacity". In: *Applied Thermal Engineering* 130 (Feb. 2018), pp. 1052–1061. ISSN: 13594311. DOI: 10.1016/j.applthermaleng.2017.11.084.

[67] I.E. Idelcchik. *Handbook of Hydraulic Resistance: Coefficients of Local Resistance and of Friction*. Ed. by D. Grunaer and IPST Staff. 1st ed. Vol. 509. The U.S. Atomic Energy Commission and the national science foundation, 1966, pp. 190–196.

[68] J El Hajal, J.R Thome, and A Cavallini. "Condensation in horizontal tubes, part 1: two-phase flow pattern map". In: *International Journal of Heat and Mass Transfer* 46.18 (Aug. 2003), pp. 3349–3363. ISSN: 00179310. DOI: 10.1016/S0017-9310(03)00139-X.

[69] Sung-Min Kim and Issam Mudawar. "Universal approach to predicting two-phase frictional pressure drop for adiabatic and condensing mini/micro-channel flows". In: *International Journal of Heat and Mass Transfer* 55.11-12 (May 2012), pp. 3246–3261. ISSN: 00179310. DOI: 10.1016/j.ijheatmasstransfer.2012.02.047.

[70] Ing Youn Chen, Kai-Shing Yang, and Chi-Chung Wang. "Two-Phase Pressure Drop of Air-Water in Small Horizontal Tubes". In: *Journal of Thermophysics and Heat Transfer* 15.4 (Oct. 2001), pp. 409–415. ISSN: 0887-8722. DOI: 10.2514/2.6643.

[71] Warren M. Rohsenow, James R Hartnett, and Young I. Cho. *Handbook of Heat Transfer*. Third Edition. Vol. 18. McGraw-Hill, 1998, pp. 38–14.

[72] Randeep Singh, Aliakbar Akbarzadeh, and Masataka Mochizuki. "Operational characteristics of a miniature loop heat pipe with flat evaporator". In: *International Journal of Thermal Sciences* 47.11 (Nov. 2008), pp. 1504–1515. ISSN: 12900729. DOI: 10.1016/j.ijthermalsci.2007.12.013.

[73] Randeep Singh, Aliakbar Akbarzadeh, and Masataka Mochizuki. "Effect of Wick Characteristics on the Thermal Performance of the Miniature Loop Heat Pipe". In: *Journal of Heat Transfer* 131.8 (Aug. 2009). ISSN: 0022-1481. DOI: 10.1115/1.3109994.

[74] Tianyuan Zhao et al. "Experimental investigation of a loop heat pipe with a flat evaporator and cupric oxide nanofluids as working fluid". In: *Energy Reports* 7 (Nov. 2021), pp. 7693–7703. ISSN: 23524847. DOI: 10.1016/j.egyr.2021.10.114.

[75] Zikang Zhang et al. "Application of biporous wick in flat-plate loop heat pipe with long heat transfer distance". In: *Applied Thermal Engineering* 184 (Feb. 2021), p. 116283. ISSN: 13594311. DOI: 10.1016/j.applthermaleng.2020.116283.

[76] Inès Gabsi, Samah Maalej, and Mohamed Chaker Zaghdoudi. "Modeling of Loop Heat Pipe Thermal Performance". In: *Journal of Advanced Research in Fluid Mechanics and Thermal Sciences* 81.1 (Mar. 2021), pp. 41–72. ISSN: 22897879. DOI: 10.37934/arfmts.81.1.4172.

[77] Qi Jiang et al. "A Review on Additive Manufacturing of Pure Copper". In: *Coatings* 11.6 (June 2021), p. 740. ISSN: 2079-6412. DOI: 10.3390/coatings11060740.

[78] Eberhard Abele et al. "Selective laser melting for manufacturing of thin-walled porous elements". In: *Journal of Materials Processing Technology* 215 (Jan. 2015), pp. 114–122. ISSN: 09240136. DOI: 10.1016/j.jmatprotec.2014.07.017.

[79] Mehrshad Mehrpouya et al. "Multimaterial powder bed fusion techniques". In: *Rapid Prototyping Journal* 28.11 (Dec. 2022), pp. 1–19. ISSN: 1355-2546. DOI: 10.1108/RPJ-01-2022-0014.

[80] Osezua Ibhadode et al. "Topology optimization for metal additive manufacturing: current trends, challenges, and future outlook". In: *Virtual and Physical Prototyping* 18.1 (Dec. 2023). ISSN: 1745-2759. DOI: 10.1080/17452759.2023.2181192.

[81] Nataliia Fedorova et al. "Static Wettability of Differently Mechanically Treated and Amphiphobic-Coated Aluminium Surfaces". In: *Materials* 13.10 (May 2020), p. 2240. ISSN: 1996-1944. DOI: 10.3390/ma13102240.

[82] K.K. Wong and K.C. Leong. "Saturated pool boiling enhancement using porous lattice structures produced by Selective Laser Melting". In: *International Journal of Heat and Mass Transfer* 121 (June 2018), pp. 46–63. ISSN: 00179310. DOI: 10.1016/j.ijheatmasstransfer.2017.12.148.

[83] Daxiang Deng et al. "A comparative study of flow boiling performance in reentrant copper microchannels and reentrant porous microchannels with multi-scale rough surface". In: *International Journal of Multiphase Flow* 72 (June 2015), pp. 275–287. ISSN: 03019322. DOI: 10.1016/j.ijmultiphaseflow.2015.01.004.

[84] Yong Tang et al. "Effects of structural parameter on flow boiling performance of interconnected microchannel net". In: *Applied Thermal Engineering* 112 (Feb. 2017), pp. 164–173. ISSN: 13594311. DOI: 10.1016/j.applthermaleng.2016.10.050.

[85] Jin S. Kim et al. "Effect of surface roughness on pool boiling heat transfer of water on hydrophobic surfaces". In: *International Journal of Heat and Mass Transfer* 118 (Mar. 2018), pp. 802–811. ISSN: 00179310. DOI: 10.1016/j.ijheatmasstransfer.2017.10.124.

[86] Avdhoot Walunj and A. Sathyabhama. "Comparative study of pool boiling heat transfer from various microchannel geometries". In: *Applied Thermal Engineering* 128 (Jan. 2018), pp. 672–683. ISSN: 13594311. DOI: 10.1016/j.applthermaleng.2017.08.157.

[87] Amir Faghri. "Heat Pipes: Review, Opportunities and Challenges". In: *Frontiers in Heat Pipes* 5.1 (Apr. 2014). ISSN: 2155-658X. DOI: 10.5098/fhp.5.1.

A Material properties

A.1 Compatibility data

Choosing the right combination of working fluid and evaporator material is essential to avoid a chemical reaction between working fluid and LHP material. Based on literature, Table 6 gives an overview of suitable combinations of wick material and working fluid [87].

Working Fluid	**Compatible material**	**Incompatible material**
Water	Stainless Steel, Copper, Silica, Nickel, Titanium	Aluminium, Inconel
Ammonia	Aluminium, Stainless Steel, Cold Rolled Steel, Iron, Nickel	
Methanol	Stainless Steel,Iron, Copper, Brass, Silica, Nickel	Aluminium
Acetone	Aluminum,Stainless Steel, Copper, Brass, Silica	Aluminium
Freon-11	Aluminium	
Freon-21	Aluminium, Iron	
Freon-113	Aluminium	
Heptane	Aluminium	
Dowtherm	Stainless Steel, Copper, Silica	
Lithium	Tungsten, Tantalum, Molybdenum, Niobium	Stainless Steel, Nickel, Inconel, Titanium
Sodium	Stainless Steel, Nickel, Inconel, Niobium	Titanium
Cesium	Titanium, Niobium, Stainless Steel, Nickel-based super alloys	
Mercury	Stainless Steel	Molybdenum, Nickel, Tantalum, Inconel, Titanium, Niobium
Lead	Tungsten, Tantalum	Stainless Steel, Nickel, Inconel, Titanium, Niobium
Silver	Tungsten, Tantalum	Rhenium

Table 6: Generalized results of experimental compatibility tests [87]

B Steady-state modeling

B.1 Casing heat leak

The evaporator casing, as shown in figure 35, is modeled as a rectangular domain. The points c_0 and c_1 represent respectively the height of the base plate and grooves ($c_0 = H_b + H_{vg}$) and this height together with the wick thickness ($c_1 = c_0 + t_w$).

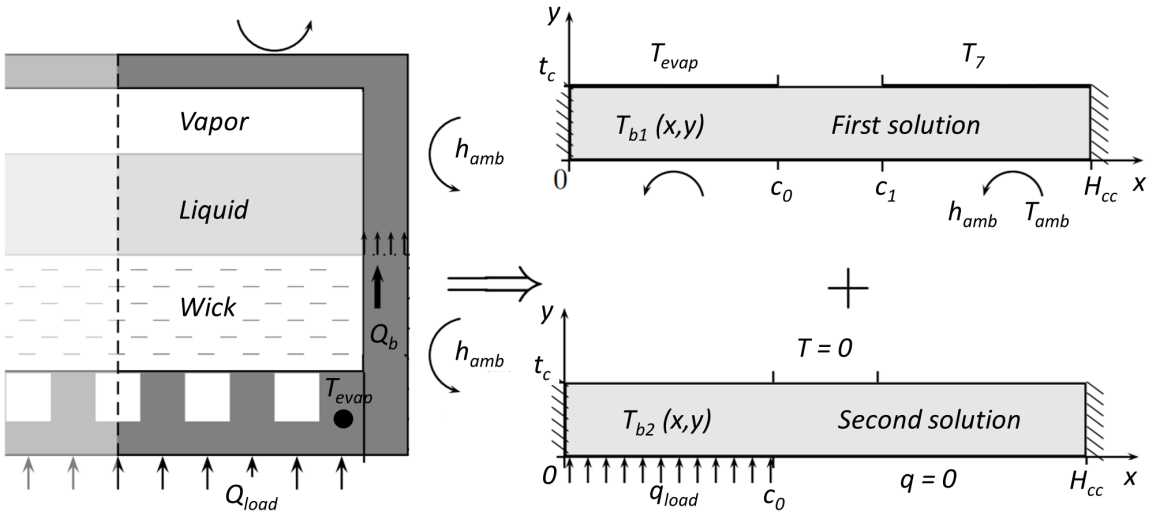

Figure 35: Modeling evaporator casing [35]

The solving procedure to describe the heat leak through the wick structure starts with the 2-dimensional stationary heat equation given in equation 55 where T_b is the temperature of the casing [35].

$$\frac{\partial^2 T_b}{\partial x^2} + \frac{\partial^2 T_b}{\partial y^2} = 0 \tag{55}$$

A non-dimensional temperature is described with equation 56 and results in equation 57

$$T_b^* = \frac{k_c(T_b - T_7)}{q_{load}\, t_c}; \tag{56}$$

$$X = \frac{x}{H_{cc}}; \qquad Y = \frac{y}{t_c}; \qquad D = \frac{t_c}{H_{cc}}; \tag{57}$$

The general profile is distinguished into 2 temperature profiles $T_{b1}(x, y)$ and $T_{b2}(x, y)$ to include all the required boundary conditions. The first profile refers to the temperatures

inside the system and the second one adds the applied heat flux to the solution. It is supposed that there is an adiabatic condition at both ends of the wall due to symmetry. Further, there is a constant convective heat transfer coefficient with the ambient (h_{amb}) at the entire external evaporator surface. The inner side of the casing has two fixed temperatures, namely the evaporator temperature ($0 \leq x \leq c_0$) and the liquid/vapor bulk temperature of the compensation chamber ($c_1 \leq x \leq H_{cc}$). To simplify the model, the compensation chamber bulk temperature will be equal to the saturated liquid temperature (T_7) inside this reservoir, however, it must be noted that in actual situations the working fluid temperature distribution varies along the inner side of the casing. The temperature profile between $c_0 \leq x \leq c_1$ is supposed to be linear. The non-dimensional temperature profile for the first solution is described as:

$$
\begin{aligned}
&\left.\frac{\partial T^*_{\mathrm{b1}}}{\partial X}\right|_{X=0} = \left.\frac{\partial T^*_{\mathrm{b1}}}{\partial X}\right|_{X=1} = 0 \quad \text{(symmetry)} \\
&\left.\frac{\partial T^*_{\mathrm{b1}}}{\partial Y}\right|_{Y=0} = Bi_{\mathrm{c}} T^*_{\mathrm{b1}} + \frac{h_{\mathrm{amb}}}{q_0}\left(T_7 - T_{\mathrm{amb}}\right) \\
&\text{with} \quad Bi_{\mathrm{c}} = \frac{t_c h_{\mathrm{amb}}}{k_{\mathrm{c}}} \quad \text{(Biot number)} \\
&T^*_{\mathrm{b1}}(X,1) = \begin{cases} \frac{k_{\mathrm{c}}(T_{\mathrm{evap}} - T_7)}{q_0\ t_c} & \text{if } 0 < X \leqslant \frac{c_0}{H_{cc}} \\ \frac{k_{\mathrm{c}}}{q_0\ t_c}\left(T_{\mathrm{evap}} - T_7\right)\frac{c_1 - H_{cc}X}{c_1 - c_0} & \text{if } \frac{c_0}{H_{cc}} \leqslant X < \frac{c_1}{H_{cc}} \\ 0 & \text{if } \frac{c_1}{H_{cc}} < X < 1 \end{cases}
\end{aligned}
\tag{58}
$$

As mentioned the second temperature profile is related to the heat flux through the system. Again both ends are supposed to be adiabatic due to symmetry. Furthermore, it is considered that there is no heat transfer at the entire surface excluding the interface between ($0 \leq x \leq c_0$). Using the boundary conditions, the non-dimensional heat equation becomes:

$$
\begin{aligned}
&\left.\frac{\partial T^*_{\mathrm{b2}}}{\partial X}\right|_{X=0} = \left.\frac{\partial T^*_{\mathrm{b2}}}{\partial X}\right|_{X=1} = 0 \\
&\left.\frac{\partial T^*_{\mathrm{b2}}}{\partial Y}\right|_{Y=0} = \begin{cases} -\frac{q_{\mathrm{load}}}{q_0} & \text{if } 0 < X \leqslant \frac{c_0}{H_{cc}} \\ 0 & \text{if } X > \frac{c_0}{H_{cc}} \end{cases} \\
&T^*_{\mathrm{b2}}(X,1) = 0
\end{aligned}
\tag{59}
$$

Using the general expression 2D Fourier series enables to combine 2 non-dimensional temperature fields:

$$\begin{aligned} T_{\mathrm{b}}^{*}(X,Y) &= C_{01}Y + C_{02} \\ &\quad + \sum_{m=1}^{\infty} \left(C_{\mathrm{m1}} e^{m\pi DY} + C_{\mathrm{m2}} e^{-m\pi DY} \right) \cos(m\pi X) \end{aligned} \tag{60}$$

The coefficients within this formula are as follows:

$$\begin{aligned} C_{01} &= \frac{Bi_{\mathrm{b}}}{Bi_{\mathrm{b}}+1} \frac{k_{\mathrm{c}}}{q_0\, t_c} \left(\left(T_{\mathrm{evap}} - T_7\right) \frac{c_0 + c_1}{2c} + \left(T_7 - T_{\mathrm{amb}}\right) \right) \\ &\quad - \frac{c_0}{H_{cc}} \frac{q_{\mathrm{load}}}{q_0} \\ C_{02} &= \frac{1}{Bi_{\mathrm{c}}+1} \frac{k_{\mathrm{c}}}{q_0\, t_c} \left(\left(T_{\mathrm{evap}} - T_7\right) \frac{c_0 + c_1}{2c} - Bi_{\mathrm{c}} \left(T_7 - T_{\mathrm{amb}}\right) \right) \\ &\quad + \frac{c_0}{H_{cc}} \frac{q_{\mathrm{load}}}{q_0} \\ C_{\mathrm{m1}} &= 2 \frac{k_{\mathrm{c}}}{q_0 t_c} \frac{T_{\mathrm{evap}} - T_7}{m^2\pi^2} \frac{H_{cc}}{c_1 - c_0} \frac{\cos\left(m\pi \frac{c_0}{H_{cc}}\right) - \cos\left(m\pi \frac{c_1}{H_{cc}}\right)}{e^{m\pi D} + \frac{m\pi D + Bi_{\mathrm{c}}}{m\pi D - m\pi D} e^{-m}} \\ &\quad - 2 \frac{q_{\mathrm{load}}}{q_0} \frac{1}{m^2\pi^2 D} \sin\left(m\pi \frac{c_0}{H_{cc}}\right) \frac{1}{1 + e^{2m\pi D}} \\ C_{\mathrm{m2}} &= 2 \frac{k_{\mathrm{c}}}{q_0 t_c} \frac{T_{\mathrm{evap}} - T_7}{m^2\pi^2} \frac{H_{cc}}{c_1 - c_0} \frac{\cos\left(m\pi \frac{c_0}{H_{cc}}\right) - \cos\left(m\pi \frac{c_1}{H_{cc}}\right)}{e^{-m\pi D} + \frac{m\pi D - Bi_{\mathrm{c}}}{m\pi D + Bi_{\mathrm{c}}} e^{m\pi D}} \\ &\quad + 2 \frac{q_{\mathrm{load}}}{q_0} \frac{1}{m^2\pi^2 D} \sin\left(m\pi \frac{c_0}{H_{cc}}\right) \frac{1}{1 + e^{-2m\pi D}} \end{aligned} \tag{61}$$

As mentioned at y = 0 there is no temperature distribution considered and so the heat leak from the casing to the ambient can be described by:

$$\begin{aligned} Q_{\text{amb}} = & \int_0^{\infty} h_{\text{amb}}\, \pi x \left(T_{\text{b}}(x,0) - T_{\text{amb}}\right) dx \\ & + \int_{c_0}^{c_1} h_{\text{amb}}\, \pi c_0 \left(T_{\text{b}}(x,0) - T_{\text{amb}}\right) dx \\ = & h_{\text{amb}} \pi c_0 \left(c_1 - \frac{c_0}{2}\right) \left(T_7 - T_{\text{amb}} + \frac{q_0 t_c}{k_{\text{c}}} C_{02}\right) \\ & + h_{\text{amb}}\, \pi \frac{q_0 t_c}{k_{\text{c}}} \sum_{m=1}^{\infty} \left(C_{\text{m1}} + C_{\text{m2}}\right) \frac{H_{cc}}{m\pi} \\ & \times \left(\frac{H_{cc}}{m\pi}\left(-1 + \cos\left(\frac{m\pi c_0}{2}\right)\right) + \frac{c_0}{m\pi} \sin\left(m\pi \frac{c_1}{H_{cc}}\right)\right) \end{aligned} \tag{62}$$

The total transferred conductive heat through the evaporator body Q_b is calculated by integrating Fourier's law at y = c_1.

$$\begin{aligned} Q_{\text{b}} = Q_{\text{amb}} + \int_0^d - \pi c_0 k_{\text{c}} \frac{\partial T_{\text{c}}}{\partial x}\bigg|_{x=c_1} dy = Q_{\text{amb}} & + t_c c_0 q_0 \sum_{m=1}^{\infty} \pi \sin\left(m\pi \frac{c_1}{H_{cc}}\right) \\ & \times \left(C_{\text{m1}}\left(e^{m\pi D} - 1\right) - C_{\text{m2}}\left(e^{-m\pi D} - 1\right)\right) \end{aligned} \tag{63}$$

The entire heat leak through the wall and the ambient heat leak both can be written in terms of coefficients independent of temperatures.

$$Q_b = B_1 T_7 + B_2 T_{evap} + B_3 \tag{64}$$

$$Q_{amb} = B_4 T_7 + B_5 T_{evap} + B_6 \tag{65}$$

These coefficients are expressed as follows:

$$
\begin{aligned}
B_1 = {} & h_{\text{amb}}\pi\frac{c_1^2}{2}\left(\frac{-\frac{c_0+c_1}{2c_1}+1}{Bi_{\text{c}}+1}\right) \\
& -\sum_{m=1}^{100}\left(2k_{\text{c}}\frac{H_{cc}}{c_1-c_0}\frac{1}{m^2\pi^2}\left(\cos\left(\frac{m\pi c_0}{H_{cc}}\right)-\cos\left(\frac{m\pi c_1}{H_{cc}}\right)\right)\right. \\
& \left[\left(c_0\pi\sin\left(\frac{m\pi c_1}{H_{cc}}\right)\left(e^{m\pi D}-1\right)+\frac{\pi h_{\text{amb}}}{k_{\text{c}}}\left(-\frac{H_{cc}^2}{m^2\pi^2}+\frac{H_{cc}^2}{m^2\pi^2}\cos\left(\frac{m\pi c_1}{H_{cc}}\right)+\frac{c_1 c}{m\pi}\sin\left(\frac{m\pi c_1}{H_{cc}}\right)\right)\right)\right. \\
& \left.\left(e^{m\pi D}+e^{-m\pi D}\frac{m\pi D+Bi_{\text{c}}}{m\pi D-Bi_{\text{c}}}\right)^{-1}\right. \\
& \left.\left.+\left(-c_0\pi\sin\left(\frac{m\pi c_1}{H_{cc}}\right)\left(e^{-m\pi D}-1\right)+\frac{\pi h_{\text{amb}}}{k_{\text{c}}}\left(-\frac{H_{cc}^2}{m^2\pi^2}+\frac{H_{cc}^2}{m^2\pi^2}\cos\left(\frac{m\pi c_1}{H_{cc}}\right)+\frac{c_1 H_{cc}}{m\pi}\sin\left(\frac{m\pi c_1}{H_{cc}}\right)\right)\right)\right.\right. \\
& \left.\left.\left(e^{-m\pi D}+e^{m\pi D}\frac{m\pi D-Bi_{\text{c}}}{m\pi D+Bi_{\text{c}}}\right)^{-1}\right]\right)
\end{aligned}
\tag{66}
$$

$$
\begin{aligned}
B_2 = {} & h_{\text{amb}}\pi\frac{c_1^2}{2}\frac{c_0+c_1}{2H_{cc}}\frac{1}{Bi_{\text{c}}+1} \\
& +\sum_{m=1}^{100}\left(2k_{c}\frac{H_{cc}}{c_1-c_0}\frac{1}{m^2\pi^2}\left(\cos\left(\frac{m\pi c_0}{H_{cc}}\right)-\cos\left(\frac{m\pi c_1}{H_{cc}}\right)\right)\right. \\
& \left[\left(c_0\pi\sin\left(\frac{m\pi c_1}{H_{cc}}\right)\left(e^{m\pi D}-1\right)+\frac{\pi h_{\text{amb}}}{k_{\text{c}}}\left(-\frac{H_{cc}^2}{m^2\pi^2}+\frac{H_{cc}^2}{m^2\pi^2}\cos\left(\frac{m\pi c_1}{H_{cc}}\right)+\frac{c_1 H_{cc}}{m\pi}\sin\left(\frac{m\pi c_1}{H_{cc}}\right)\right)\right)\right. \\
& \left.\left(\left(e^{m\pi D}+e^{-m\pi D}\frac{m\pi D+B\dot{i}_{\text{c}}}{m\pi D-B\dot{i}_{\text{c}}}\right)^{-1}\right)\right. \\
& \left.\left.+\left(c_0\pi\sin\left(\frac{m\pi c_1}{H_{cc}}\right)\left(e^{-m\pi D}-1\right)+\frac{\pi h_{\text{amb}}}{k_{\text{c}}}\left(-\frac{H_{cc}^2}{m^2\pi^2}+\frac{H_{cc}^2}{m^2\pi^2}\cos\left(\frac{m\pi c_1}{H_{cc}}\right)+\frac{c_1 H_{cc}}{m\pi}\sin\left(\frac{m\pi c_1}{H_{cc}}\right)\right)\right)\right.\right. \\
& \left.\left.\left(e^{-m\pi D}+e^{m\pi D}\frac{m\pi D-Bi_b}{m\pi D+Bi_b}\right)^{-1}\right]\right)
\end{aligned}
\tag{67}
$$

$$
\begin{aligned}
B_3 = {} & h_{\text{amb}}\,\pi\frac{c_1^2}{2}\left(\frac{q_0 t_c}{k_{\text{c}}}\frac{c_0 q_{\text{load}}}{q_0} - \frac{1}{Bi_{\text{c}}+1}T_{\text{amb}}\right) \\
& + \sum_{m=1}^{100}\left(2q_{\text{load}}H_{cc}\frac{1}{m^2\pi^2}\sin\left(\frac{m\pi c_0}{H_{cc}}\right)\right. \\
& \left[\left(-c_0\pi\sin\left(\frac{m\pi c_1}{H_{cc}}\right)\left(e^{m\pi D}-1\right) - \frac{\pi h_{\text{amb}}}{k_{\text{c}}}\left(-\frac{H_{cc}^2}{m^2\pi^2} + \frac{H_{cc}^2}{m^2\pi^2}\cos\left(\frac{m\pi c_1}{H_{cc}}\right) + \frac{c_1 H_{cc}}{m\pi}\sin\left(\frac{m\pi c_1}{H_{cc}}\right)\right)\right)\right. \\
& \left.\left(\left(1+e^{2mxD}\right)^{-1}\right)\right. \\
& \left.\left. + \left(-c_0\pi\sin\left(\frac{m\pi c_1}{H_{cc}}\right)\left(e^{-m\pi D}-1\right) + \frac{\pi h_{\text{amb}}}{k_b}\left(-\frac{H_{cc}^2}{m^2\pi^2} + \frac{H_{cc}^2}{m^2\pi^2}\cos\left(\frac{m\pi c_1}{H_{cc}}\right) + \frac{c_1 H_{cc}}{m\pi}\sin\left(\frac{m\pi c_1}{H_{cc}}\right)\right)\right)\right.\right. \\
& \left.\left.\left(1+e^{-2m\pi D}\right)^{-1}\right]\right)
\end{aligned}
\tag{68}
$$

$$
\begin{aligned}
B_4 = {} & h_{\text{amb}}\,\pi\frac{c_1^2}{2}\left(\frac{-\frac{c_0+c_1}{2H_{cc}}+1}{Bi_{\text{c}}+1}\right) \\
& - \sum_{m=1}^{\infty}\left(2k_c\frac{H_{cc}}{c_1-c_0}\frac{1}{m^2\pi^2}\left(\cos\left(\frac{m\pi c_0}{H_{cc}}\right) - \cos\left(\frac{m\pi c_1}{H_{cc}}\right)\right)\right. \\
& \times \frac{\pi h_{\text{amb}}}{k_{\text{c}}}\left(-\frac{H_{cc}^2}{m^2\pi^2} + \frac{H_{cc}^2}{m^2\pi^2}\cos\left(\frac{m\pi c_1}{H_{cc}}\right) + \frac{c_1 H_{cc}}{m\pi}\sin\left(\frac{m\pi c_1}{H_{cc}}\right)\right) \\
& \left.\times\left[\left(e^{m\pi D} + e^{-m\pi D}\frac{m\pi D + Bi_{\text{c}}}{m\pi D - Bi_{\text{c}}}\right)^{-1} + \left(e^{-m\pi D} + e^{m\pi D}\frac{m\pi D - Bi_{\text{c}}}{m\pi D + Bi_{\text{c}}}\right)^{-1}\right]\right)
\end{aligned}
\tag{69}
$$

$$
\begin{aligned}
B_5 = {} & h_{\text{amb}}\,\pi\frac{c_1^2}{2}\frac{c_0+c_1}{2H_{cc}}\frac{1}{Bi_{\text{c}}+1} \\
& + \sum_{m=1}^{\infty}\left(2k_c\frac{H_{cc}}{c_1-c_0}\frac{1}{m^2\pi^2}\left(\cos\left(\frac{m\pi c_0}{H_{cc}}\right) - \cos\left(\frac{m\pi c_1}{H_{cc}}\right)\right)\right. \\
& \times \frac{\pi h_{\text{amb}}}{k_{\text{c}}}\left(-\frac{H_{cc}^2}{m^2\pi^2} + \frac{H_{cc}^2}{m^2\pi^2}\cos\left(\frac{m\pi c_1}{H_{cc}}\right) + \frac{c_1 H_{cc}}{m\pi}\sin\left(\frac{m\pi c_1}{H_{cc}}\right)\right) \\
& \left.\times\left[\left(e^{m\pi D} + e^{-m\pi D}\frac{m\pi D + Bi_{\text{c}}}{m\pi D - Bi_{\text{c}}}\right)^{-1} + \left(e^{-m\pi D} + e^{m\pi D}\frac{m\pi D - Bi_{\text{c}}}{m\pi D + Bi_{\text{c}}}\right)^{-1}\right]\right)
\end{aligned}
\tag{70}
$$

$$B_6 = h_{\text{amb}}\,\pi\frac{c_1^2}{2}\left(\frac{t_c}{k_{\text{c}}}\frac{c_0 q_{\text{load}}}{q_0} - \frac{1}{Bi_{\text{c}}+1}T_{\text{amb}}\right)$$
$$-\sum_{m=1}^{\infty}\left(2q_{\text{load}}H_{cc}\frac{1}{m^2\pi^2}\sin\left(\frac{m\pi c_0}{H_{cc}}\right)\frac{\pi h_{\text{amb}}}{k_{\text{c}}}\left(-\frac{H_{cc}^2}{m^2\pi^2}+\frac{H_{cc}^2}{m^2\pi^2}\cos\left(\frac{m\pi c_1}{H_{cc}}\right)+\frac{c_1 H_{cc}}{m\pi}\sin\left(\frac{m\pi c_1}{H_{cc}}\right)\right)\right.$$
$$\left.\times\left[\left(1+e^{2m\pi D}\right)^{-1}-\left(1+e^{-2m\pi D}\right)^{-1}\right]\right) \tag{71}$$

B.2 Wick heat leak

Next to the heat leak through the casing, the heat leak through the wick structure is modeled using the 2D Fourier approach [35]. A part of the wick structure is selected, including the half side of the groove ($0 \leq x \leq a_0$) and the half side of the fin ($a_0 = \frac{W_f}{2}$). The latter contains the evaporator temperature corrected for thermal contact resistance between fins and wick ($T_{evap,w}$). The other interval ($a = \frac{W_f + W_{vg}}{2}$) represents one-half side of the groove and consists of the saturated vapor temperature T_1. The model also includes a micro-region between the groove and fin where intensive evaporation occurs ($a_0 \leq x \leq a_1$).

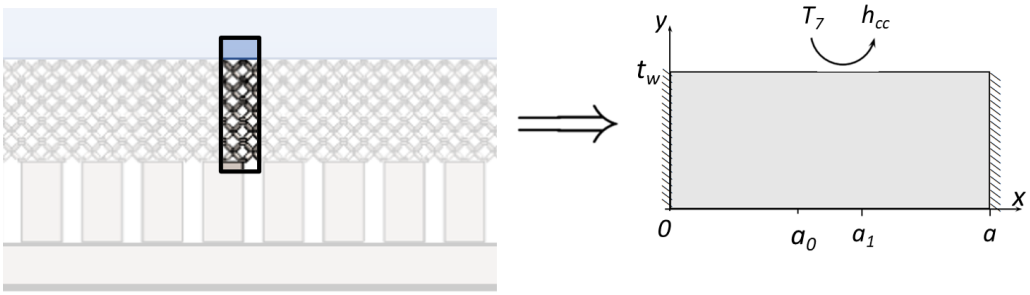

Figure 36: Modeling wick structure [35]

The solving procedure starts with the heat equation of the porous structure that is used to describe the conductive heat transfer inside the wick, given in equation 72, where values X, Y and B are described with equation 73.

$$\frac{\partial^2 T^*_{\mathrm{w1}}}{\partial X^2} + \frac{1}{B^2}\frac{\partial^2 T^*_{\mathrm{w1}}}{\partial Y^2} = 0 \tag{72}$$

$$X = \frac{x}{a}, \quad Y = \frac{y}{t_w} \quad \text{and} \quad B = \frac{t_w}{a} \tag{73}$$

It is assumed that both ends are adiabatic due to symmetry, so:

$$\left.\frac{\partial T^*_{\mathrm{w1}}}{\partial X}\right|_{X=0} = \left.\frac{\partial T^*_{\mathrm{w1}}}{\partial X}\right|_{X=1} = 0 \tag{74}$$

The general 2D Fourier expression that describes the conduction through the wick is then:

$$T_{\mathrm{w1}}(X,Y) = \sum_{m=0}^{\infty} A_m(Y)\cos(m\pi X) \tag{75}$$

By combining this general expression with the non-dimensional heat equation, a new correlation is obtained namely:

$$-(m\pi B)^2 A_m(Y) + \frac{\partial^2 A_m(Y)}{\partial Y^2} = 0 \tag{76}$$

Suppose a linear temperature profile in this micro-region area and so consider that the slope of this temperature gradient is related to the heat transfer coefficient at the liquid-vapor interface and the length of this region ($a_0 \leq x \leq a_1$) [60]. The size of this region is estimated using equation 77, where k_{we} and h_{ev} are respectively, the effective thermal conductivity of the wick structure and the heat transfer coefficient of evaporation [35].

$$a_1 - a_0 = \frac{k_{we}}{h_{ev}} \tag{77}$$

The heat transfer coefficient of evaporation h_{ev} is obtained using the Kinetic gas theory, where a_{ev}, is the evaporation coefficient.

$$h_{ev} = \frac{2a_{ev}}{2 - a_{ev}} \frac{\rho_1 {h_1}^2}{T_1} \left(\frac{2\pi \bar{R} T_1}{\bar{M}}\right)^{-0.5} \left(1 - \frac{P_1}{2\rho_1 h_1}\right) \tag{78}$$

As a result, the boundary condition at the interface Y = 0 becomes:

$$T^*_{\mathrm{w1}}(X,0) = \begin{cases} \frac{k_{\mathrm{we}}(T_{\mathrm{evap,w}} - T_7)}{q_0 t_w} & \text{if } 0 < X \leqslant \frac{a_0}{a} \\ \frac{k_{\mathrm{we}}}{q_0 t_w}\left((T_1 - T_7) + (T_{\mathrm{evap,w}} - T_1)\frac{a_1 - aX}{a_1 - a_0}\right) & \text{if } \frac{a_0}{a} < X < \frac{a_1}{a} \\ \frac{k_{\mathrm{we}}(T_1 - T_7)}{q_0 t_w} & \text{if } \frac{a_1}{a} \leqslant X < 1 \end{cases} \tag{79}$$

Furthermore, it is assumed that there is heat transfer between the wick and the liquid bulk inside the compensation chamber. As a result, the boundary condition at this interface is:

$$\left.\frac{\partial T^*_{\mathrm{w1}}}{\partial Y}\right|_{Y=1} = -Bi_{\mathrm{w}} T^*_{\mathrm{w1}} \quad \text{with} \quad Bi_{\mathrm{w}} = \frac{t_w h_{\mathrm{cc}}}{k_{\mathrm{we}}} \tag{80}$$

The non-dimensional temperature field is then:

$$\begin{aligned} T^*_{\mathrm{w1}}(X,Y) &= A_{01}Y + A_{02} \\ &\quad + \sum_{m=1}^{\infty} \left(A_{\mathrm{m1}} e^{m\pi BY} + A_{\mathrm{m2}} e^{-m\pi BY}\right) \cos(m\pi X) \end{aligned} \tag{81}$$

Including the coefficients:

$$\begin{aligned}
A_{01} &= -\frac{Bi_{\mathrm{w}}}{1+Bi_{\mathrm{w}}}\frac{k_{\mathrm{we}}}{q_0 t_w}\left(T_1 - T_7 + (T_{\mathrm{evap,w}} - T_1)\,\frac{a_0+a_1}{2a}\right)\\
A_{02} &= \frac{k_{\mathrm{we}}}{q_0 t_w}\left(T_1 - T_7 + (T_{\mathrm{evap,w}} - T_1)\,\frac{a_0+a_1}{2a}\right)\\
A_{\mathrm{m1}} &= 2\frac{k_{\mathrm{we}}}{q_0 t_w}\frac{T_{\mathrm{evap,w}} - T_1}{m^2\pi^2}\frac{a}{a_1-a_0}\frac{\cos\left(m\pi\frac{a_0}{a}\right)-\cos\left(m\pi\frac{a_1}{a}\right)}{1+\frac{m\pi B+Bi_{\mathrm{w}}}{m\pi B-Bi_{\mathrm{w}}}}e^{2m\pi B}\\
A_{\mathrm{m2}} &= 2\frac{k_{\mathrm{we}}}{q_0 t_w}\frac{T_{\mathrm{evap,w}} - T_1}{m^2\pi^2}\frac{a}{a_1-a_0}\frac{\cos\left(m\pi\frac{a_0}{a}\right)-\cos\left(m\pi\frac{a_1}{a}\right)}{1+\frac{m\pi B-Bi_{\mathrm{w}}}{m\pi B+Bi_{\mathrm{w}}}e^{-2m\pi B}}
\end{aligned} \tag{82}$$

The non-dimensional temperature field does not include the liquid flow through the porous structure. Actually, there will be a 2D flow inside the wick structure. However, to make use of the superposition principle, a homogeneous 1D volumetric source q is supposed.

$$q = -\frac{3\dot{m}c_{p,7}\,(T_2 - T_7)}{2A_w t_w} \tag{83}$$

This volumetric source is used to describe the heat transfer occurring by convection of the working fluid inside the wick structure. The heat equation inside the wick can be described with the equation , where the boundary conditions are given in equation and .

$$\frac{\partial^2 T_{w2}}{\partial y^2} = \frac{q}{k_{we}} \tag{84}$$

$$\begin{aligned}
T_{\mathrm{w2}}(y=0) - T_{\mathrm{w2}}(y=t_w) &= t_w^2\frac{\mathrm{q}}{k_{\mathrm{we}}}\\
T_{\mathrm{evap}}(y=b) &= T_7
\end{aligned} \tag{85}$$

Finally, the non-dimensional temperature field that describes the heat transfer by convection inside the wick is described with equation 86. Using the superprinciple given in equation 87, makes it possible to add the convective and conductive non-dimensional temperature profiles.

$$T^*_{w2}(Y) = \frac{q\,t_w}{2q_0}\left(Y^2 - 3Y + 2\right) \tag{86}$$

$$T^*_{\mathrm{w}}(X,Y) = T^*_{w1}(X,Y) + T^*_{w2}(Y) \tag{87}$$

Subsequently, Fouriers law is used to describe the heat transmitted through the evaporator Q_{evap} and the heat that is dissipated by evaporation Q_{ev}:

$$\begin{aligned} Q_{\mathrm{evap}} =& \frac{A_{\mathrm{w}}}{a} \int_0^{\frac{a_0+a_1}{2}} - k_{\mathrm{we}} \frac{\partial T_{\mathrm{w}}}{\partial y}\bigg|_{y=0} dx \\ =& - A_{\mathrm{w}} q_0 \left[\frac{a_0+a_1}{2a} \left(A_{01} - \frac{3qt_w}{2q_0} \right) \right. \\ & \left. + \sum_{m=1}^{\infty} B \left(A_{\mathrm{m1}} - A_{\mathrm{m2}} \right) \sin\left(m\pi \frac{a_0+a_1}{2a} \right) \right] \end{aligned} \tag{88}$$

$$\begin{aligned} Q_{\mathrm{ev}} =& \frac{A_{\mathrm{w}}}{a} \int_{\frac{a_0+a_1}{2}}^{a} k_{\mathrm{we}} \frac{\partial T_{\mathrm{w}}}{\partial y}\bigg|_{y=0} dx \\ =& A_{\mathrm{w}} q_0 \left[\left(1 - \frac{a_0+a_1}{2a} \right) \left(A_{01} - \frac{3qt_w}{2q_0} \right) \right. \\ & \left. - \sum_{m=1}^{\infty} B \left(A_{\mathrm{m1}} - A_{\mathrm{m2}} \right) \sin\left(m\pi \frac{a_0+a_1}{2a} \right) \right] \end{aligned} \tag{89}$$

Both values can be rewritten in terms of coefficients independent of temperatures namely:

$$Q_{evap} = B_7 T_7 + B_8 T_1 + B_9 T_{evap,w} \tag{90}$$

$$Q_{ev} = B_{10} T_7 + B_{11} T_1 + B_{12} T_{evap,w} \tag{91}$$

The coefficients to determine the transfer occurring in the evaporator structure are:

$$B_7 = A_{\mathrm{w}} \frac{a_0 + a_1}{2a} \left(-\frac{k_{\mathrm{we}}}{t_w} \frac{Bi_{\mathrm{w}}}{1 + Bi_{\mathrm{w}}} + \frac{3\dot{m} c_{\mathrm{p},7}}{2A_{\mathrm{w}}} \right) \tag{92}$$

$$\begin{aligned} B_8 = A_{\mathrm{w}} \Bigg[& \sum_{m=1}^{\infty} \left(2 \frac{k_{\mathrm{we}}}{a_1 - a_0} \frac{1}{m^2 \pi^2} \sin\left(m\pi \frac{a_0 + a_1}{2a} \right) \left(\cos\left(\frac{m\pi a_0}{a} \right) - \cos\left(\frac{m\pi a_1}{a} \right) \right) \right. \\ & \left(\left(1 + e^{2m\pi B} \frac{m\pi B + Bi_{\mathrm{w}}}{m\pi B - Bi_{\mathrm{w}}} \right)^{-1} - \left(1 + e^{-2m\pi B} \frac{m\pi B - Bi_{\mathrm{w}}}{m\pi B + Bi_{\mathrm{w}}} \right)^{-1} \right) \\ & \left. + \frac{a_0 + a_1}{2a} \left(\frac{k_{\mathrm{we}}}{t_w} \left(1 - \frac{a_0 + a_1}{2a} \right) \frac{Bi_{\mathrm{w}}}{1 + Bi_{\mathrm{w}}} - \frac{3\dot{m} c_{\mathrm{p},7}}{2A_{\mathrm{w}}} \right) \right] \end{aligned} \tag{93}$$

$$\begin{aligned} B_9 = -A_{\mathrm{w}} \Bigg[& \sum_{m=1}^{\infty} \left(2 \frac{k_{\mathrm{we}}}{a_1 - a_0} \frac{1}{m^2 \pi^2} \sin\left(m\pi \frac{a_0 + a_1}{2a} \right) \left(\cos\left(\frac{m\pi a_0}{a} \right) - \cos\left(\frac{m\pi a_1}{a} \right) \right) \right. \\ & \left(\left(1 + e^{2m\pi B} \frac{m\pi B + Bi_{\mathrm{w}}}{m\pi B - Bi_{\mathrm{w}}} \right)^{-1} - \left(1 + e^{-2m\pi B} \frac{m\pi B - Bi_{\mathrm{w}}}{m\pi B + Bi_{\mathrm{w}}} \right)^{-1} \right) \\ & \left. - \frac{k_{\mathrm{we}}}{t_w} \left(\frac{a_0 + a_1}{2a} \right)^2 \frac{Bi_{\mathrm{w}}}{1 + Bi_{\mathrm{w}}} \right] \end{aligned} \tag{94}$$

$$B_{10} = A_{\mathrm{w}} \left(1 - \frac{a_0 + a_1}{2a} \right) \left(\frac{k_{\mathrm{we}}}{t_w} \frac{Bi_{\mathrm{w}}}{1 + Bi_{\mathrm{w}}} - \frac{3\dot{m} c_{\mathrm{p},7}}{2A_{\mathrm{w}}} \right) \tag{95}$$

$$\begin{aligned} B_{11} = A_{\mathrm{w}} \Bigg[& \sum_{m=1}^{\infty} \left(2 \frac{k_{\mathrm{we}}}{a_1 - a_0} \frac{1}{m^2 \pi^2} \sin\left(m\pi \frac{a_0 + a_1}{2a} \right) \left(\cos\left(\frac{m\pi a_0}{a} \right) - \cos\left(\frac{m\pi a_1}{a} \right) \right) \right. \\ & \left(\left(1 + e^{2m\pi B} \frac{m\pi B + Bi_{\mathrm{w}}}{m\pi B - Bi_{\mathrm{w}}} \right)^{-1} - \left(1 + e^{-2m\pi B} \frac{m\pi B - Bi_{\mathrm{w}}}{m\pi B + Bi_{\mathrm{w}}} \right)^{-1} \right) \\ & \left. - \left(1 - \frac{a_0 + a_1}{2a} \right) \left(\frac{k_{\mathrm{we}}}{t_w} \left(1 - \frac{a_0 + a_1}{2a} \right) \frac{Bi_{\mathrm{w}}}{1 + Bi_{\mathrm{w}}} - \frac{3\dot{m} c_{\mathrm{p},7}}{2A_{\mathrm{w}}} \right) \right] \end{aligned} \tag{96}$$

$$B_{12} = -A_{\mathrm{w}} \left[\sum_{m=1}^{\infty} \left(2 \frac{k_{\mathrm{we}}}{a_1 - a_0} \frac{1}{m^2 \pi^2} \sin\left(m\pi \frac{a_0 + a_1}{2a} \right) \left(\cos\left(\frac{m\pi a_0}{a} \right) - \cos\left(\frac{m\pi a_1}{a} \right) \right) \right. \right. \\ \left. \left. + \frac{k_{\mathrm{we}}}{t_w} \frac{a_0 + a_1}{2a} \left(1 - \frac{a_0 + a_1}{2a} \right) \right] \right. \tag{97}$$

C 2D and 3D images of evaporator design

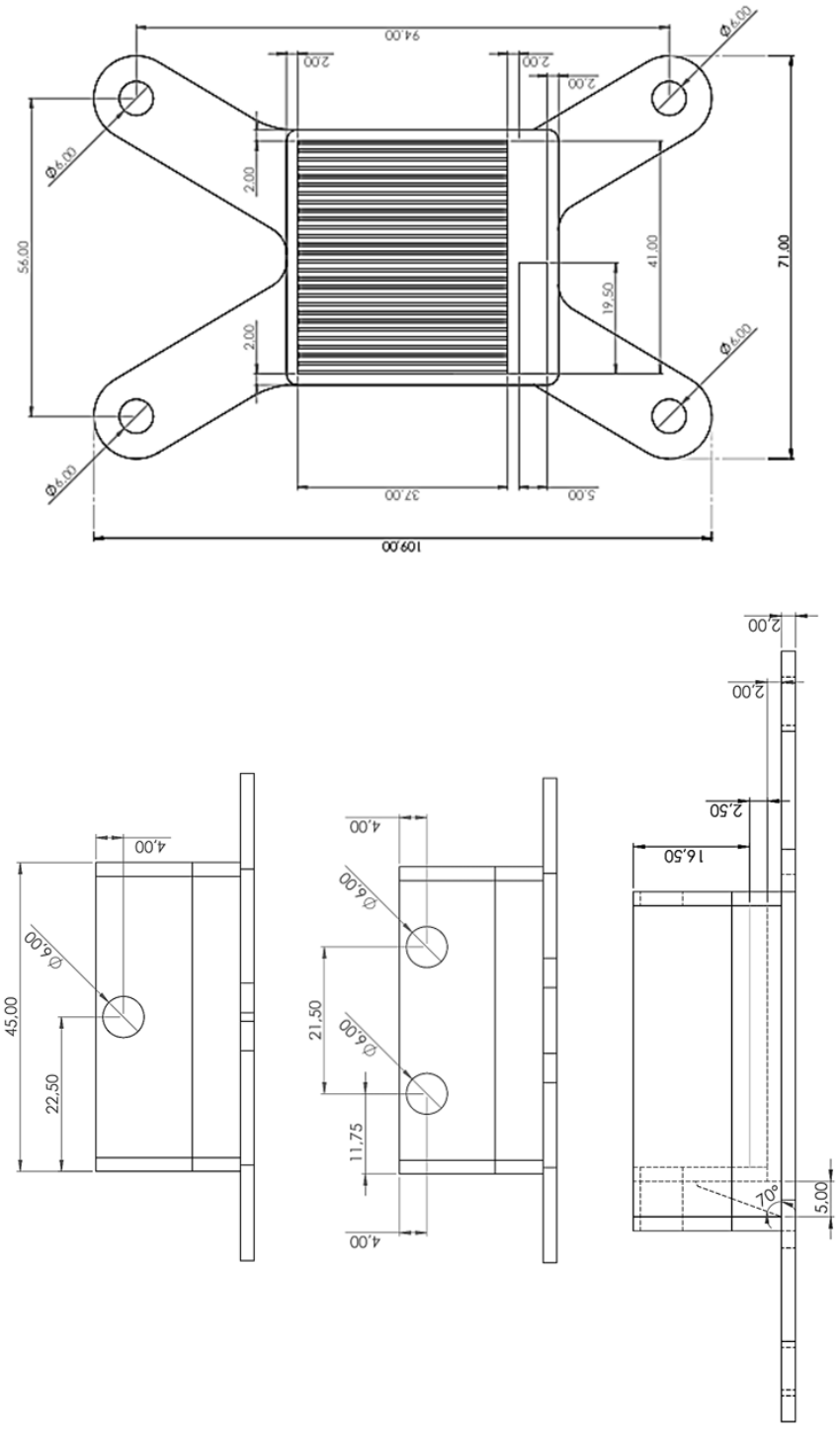

Figure 37: 2 Dimensional sketch of evaporator design

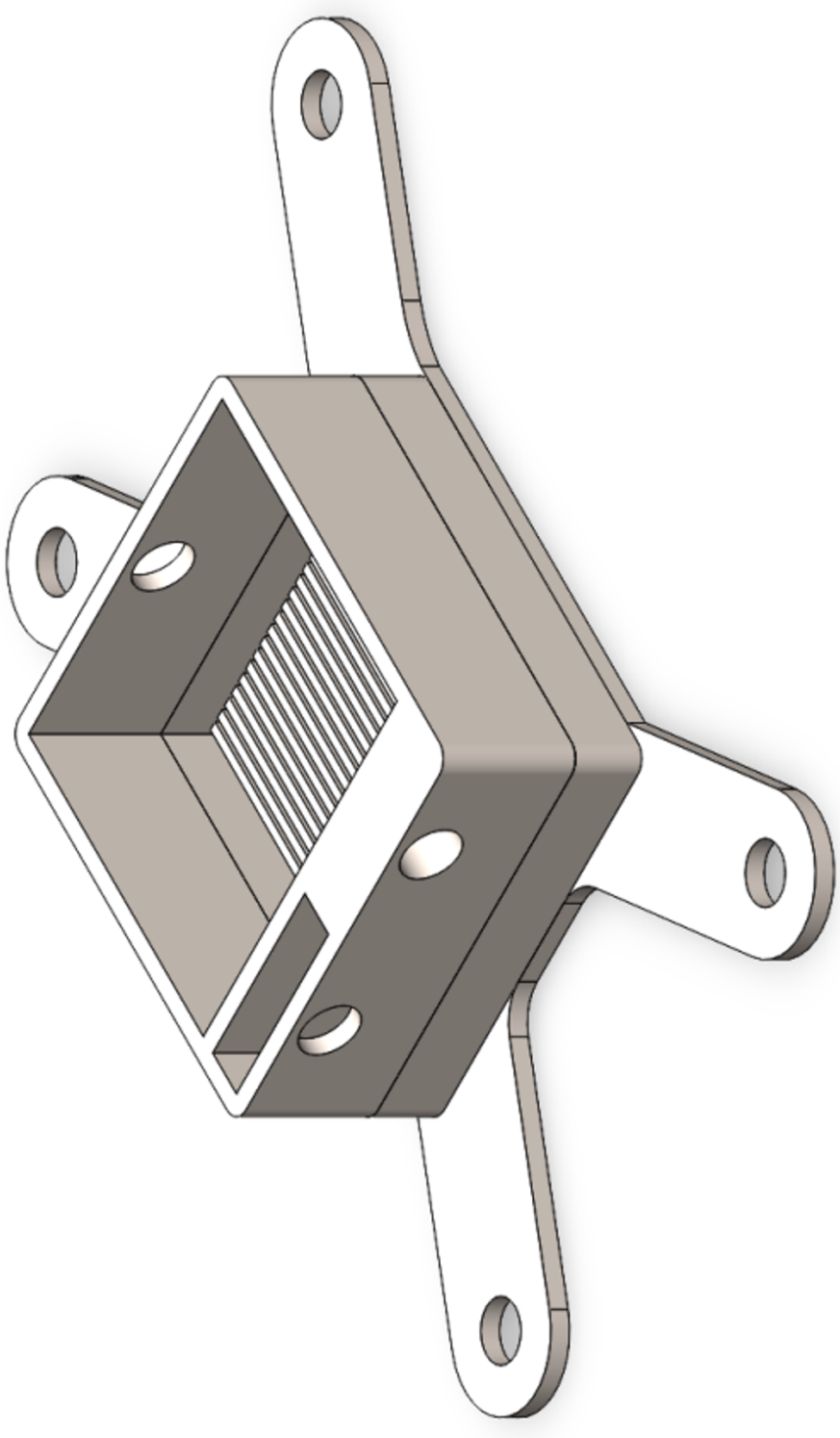

Figure 38: Evaporator design without wick structure and with advanced base plate

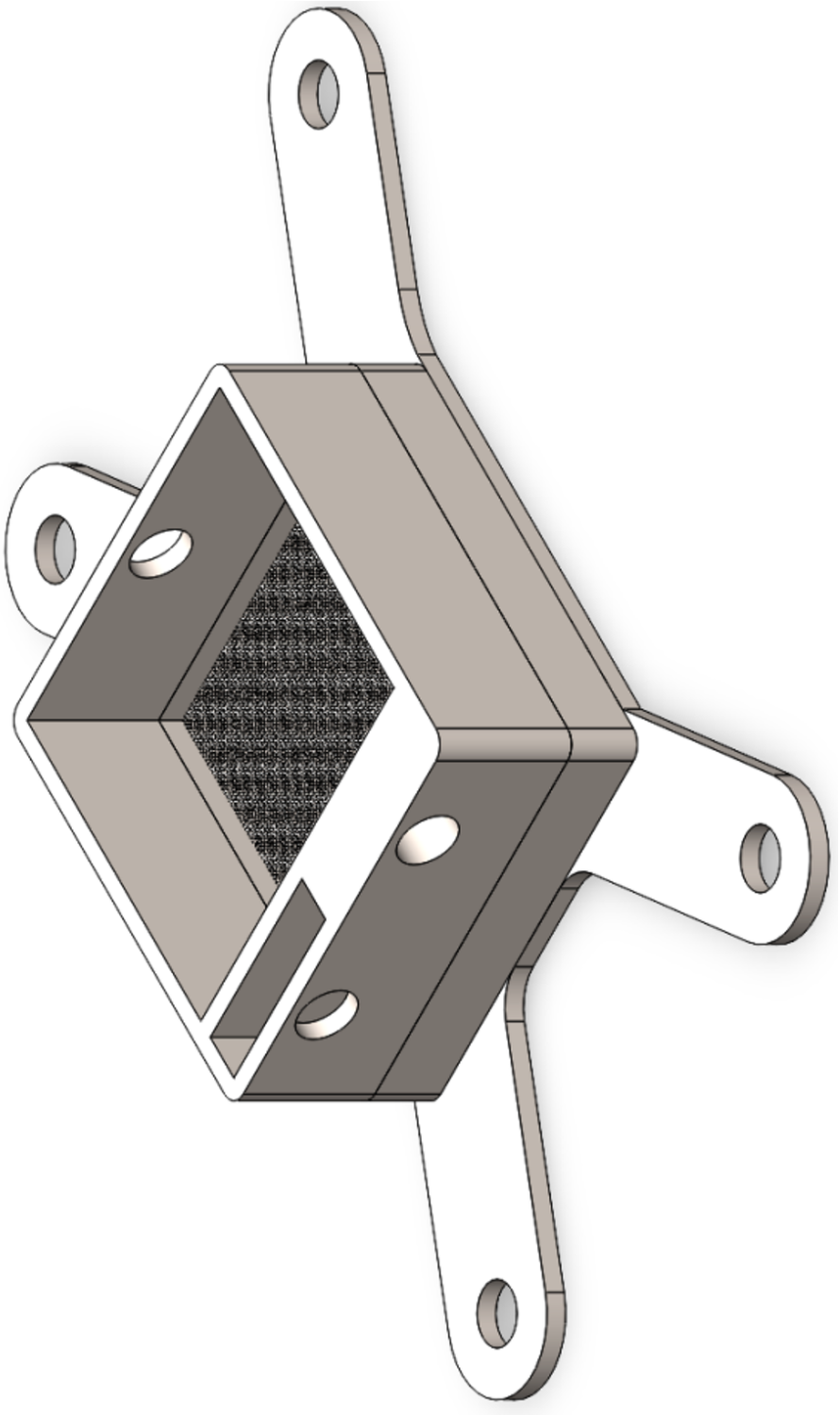

Figure 39: Evaporator design including wick structure and advanced base plate

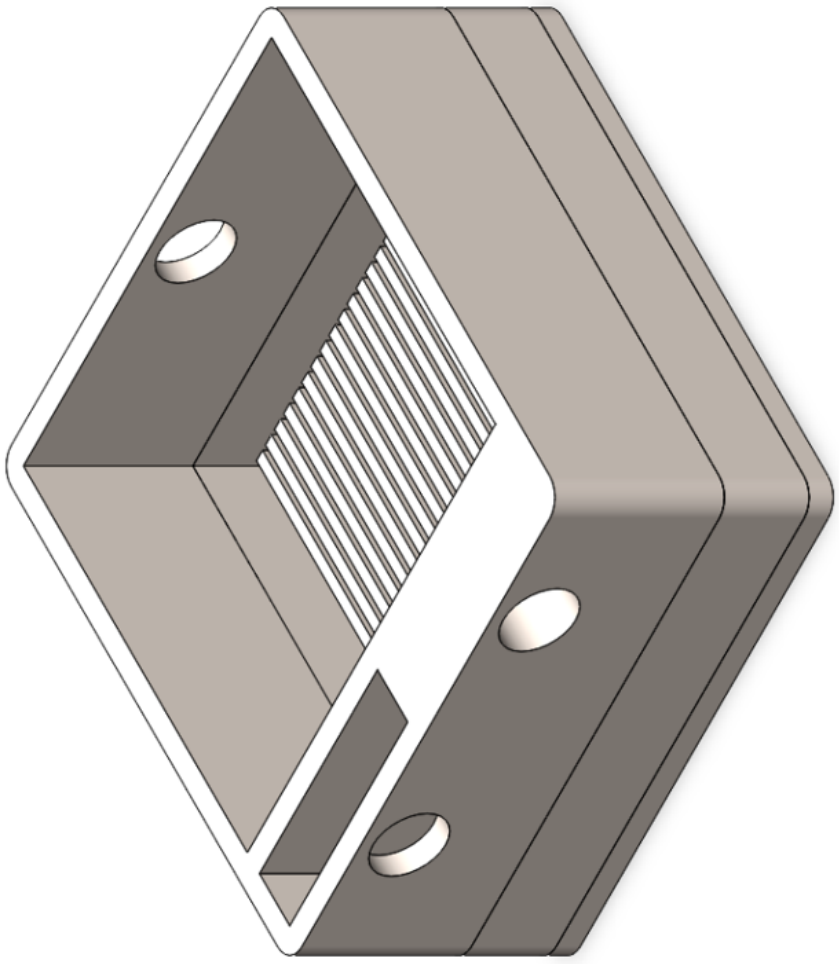

Figure 40: Evaporator design without wick structure

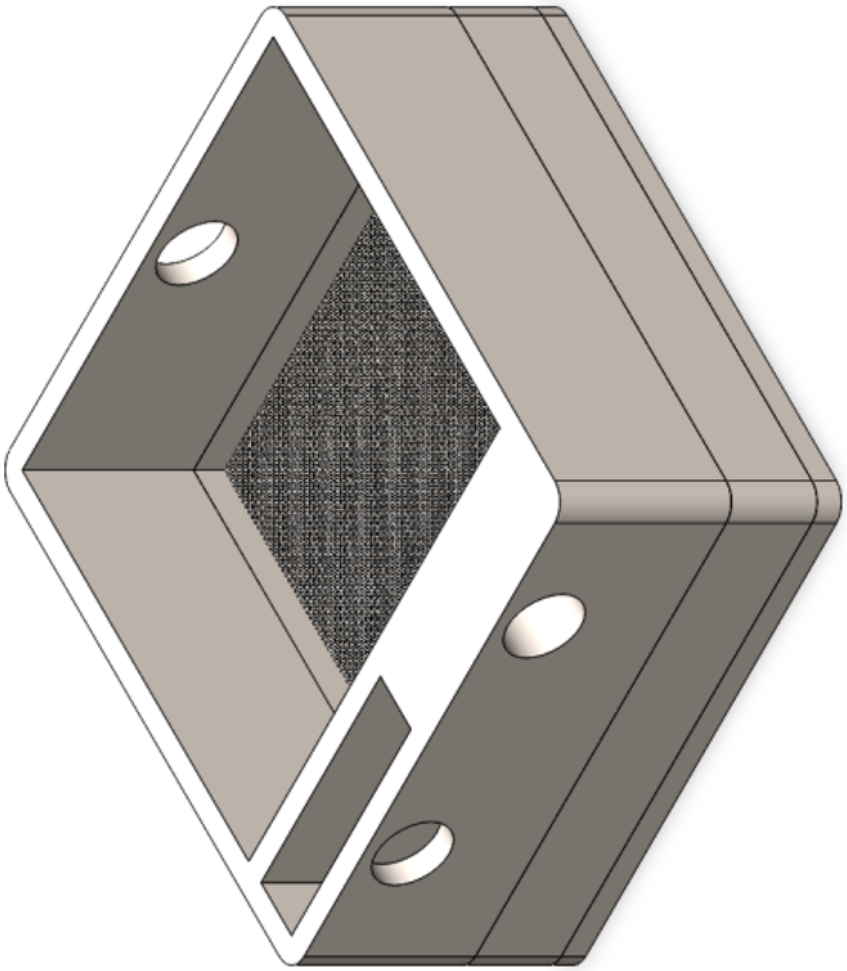

Figure 41: Evaporator design including wick structure